

MULTISCALE SIMULATION OF BORON-DOPED NANOCARBONS IN  
ELECTROCHEMICAL APPLICATIONS

by

ZHONGTAO ZHANG

C. HEATH TURNER, COMMITTEE CHAIR

YUPING BAO

JASON E. BARA

RYAN L. HARTMAN

CLAUDIA K. A. MEWES

A DISSERTATION

Submitted in partial fulfillment of the requirements  
for the degree of Doctor of Philosophy  
in the Department of Chemical and Biological Engineering  
in the Graduate School of  
The University of Alabama

TUSCALOOSA, ALABAMA

2014

Copyright Zhongtao Zhang 2014  
ALL RIGHTS RESERVED

## ABSTRACT

The stability, properties, and dispersion of novel organometallic/doped nanocarbon complexes for electrochemical application are investigated in this work with density functional theory (DFT) and molecular dynamics (MD) simulations. We suggest that electrochemical active centers like cyclopentadiene (Cp) transition metal (TM) complexes can be stabilized on boron-doped nanocarbons to create stable and high-performance support materials. We present a systematic study of the geometries, energetics, and electronic properties of CpTM (where TM=Fe, Ni, Co, Cr, Cu) complexes adsorbed on both pristine and boron-doped carbon nanotubes (CNTs) and graphene supports using DFT calculations. Significant stabilization of CpTM on boron-doped CNTs (B-CNTs) and graphenes are found, which surpasses the binding energies (BEs) of the isolated TM atoms by about 2 eV.

To evaluate the redox activity (CpFe) on B-doped nanocarbon supports, we calculate the redox potentials of CpFe/B-doped, N-doped and pristine graphene complexes with different doping patterns and concentrations with DFT calculations, combined with a conductor-like polarizable continuum model (CPCM) solvation model. The CpFe/B-doped graphene complexes show potential to be a ferrocene substitute for ferrocene-mediated electrochemical process, such as bio-sensing and dye-sensitized solar cells.

The dispersion of B-doped nanocarbons is also investigated in our work. Molecular dynamics (MD) simulations, parameterized by DFT-calculated partial charges are used to investigate the water-induced interactions, the hydration, and the debundling behavior of B-

CNTs with varying diameters and B-doping patterns within aqueous solutions. By evaluating the potential of mean force (PMF) of one, two, and three solvated B-CNTs, we demonstrate that the water-induced interactions between B-CNTs extend over prolonged distances, and the B-CNTs are shown to be more reagglomeration resistant. In addition, the hydration behavior of the B-CNTs can be understood by evaluating the water density profiles and hydrogen bonds during the solvation. These results provide guidelines for separating and dispersing B-doped nanocarbons in aqueous environments.

Overall, our simulations predict that the Cp<sup>TM</sup>/B-doped nanocarbon complexes are potential candidates for multiple electrochemical applications with significant stability, comparable redox performance to ferrocene, and enhanced dispersibility.

## DEDICATION

This dissertation is dedicated to everyone, who guided me and helped me. In particular, I am most indebted to my advisor, Dr. C. Heath Turner, my committee members, my group members and alumni.

## LIST OF ABBREVIATIONS AND SYMBOLS

DFT	Density functional theory
MD	Molecular dynamics
CNT	Carbon nanotube
TM	Transition metal
Cp	Cyclopentadienyl
B-CNT	Boron-doped carbon nanotube
EDLC	Electrochemical double layer capacitors
RAM	Random access memory
QM	Quantum mechanics
MO	Molecular orbital
LDA	Local density approximation
GGA	Generalized gradient approximation
PBE	Perdew, Burke, and Ernzerhof functional
B3LYP	Becke three-parameter exchange functional and the Lee-Yang-Parr correlation functional
PAW	projector-augmented wave
CPCM	Conductor-like polarizable continuum model
SHE	Standard hydrogen electrode
PVT	Pressure, volume and temperature
ESP	Electrostatic potentials
CHELPG	Charges from electrostatic potentials using a grid based method

BN	Boron-nitride
REPEAT	Repeating electrostatic potential extracted atomic
DDEC	Density derived electrostatic and chemical
BNCT	Boron neutron capture therapy
ORR	Oxygen reduction reaction
VASP	Vienna ab-initio simulation package
PBC	Periodic boundary conditions
DOS	Densities of states
BE	Binding energy
NBO	Natural bond orbital
ELF	Electron localization function
BD	Binding distance
CBNNT	Carbon-boron-nitride carbon nanotube
VE	Valence electrons
PDOS	Projected densities of states
GOD	Glucose oxidase
Gr	C <sub>42</sub> graphene sheet
BGr	C <sub>41</sub> B graphene sheet
BC5Gr	C <sub>35</sub> B <sub>7</sub> graphene sheet
NGr	C <sub>41</sub> N graphene sheet
UAHF	United Atom Topological Model applied on radii optimized for the HF/6-31G(d) level of theory
LOL	Localized orbital locator

HOMO	Highest occupied molecular orbital
LUMO	Lowest unoccupied molecular orbital
BNNT	Boron-nitride nanotube
BC-I	A periodic (6,6) B-CNT supercell with a BC <sub>5</sub> stoichiometry
BC-II	A periodic (6,6) B-CNT supercell with a “three-B” cluster doping pattern
BC-III	A periodic (10,10) B-CNT supercell with a BC <sub>5</sub> stoichiometry;
BC-IV	A periodic (12,12) B-CNT supercell with a BC <sub>5</sub> stoichiometry
C-I	A periodic (6,6) CNT supercell.
SPC/E	Extended simple point charge model
SETTLE	Analytical constraint algorithm for species with 3 constraints
LJ	Lennard-Jones potential
FFT	Fast Fourier transform
PME	Particle mesh Ewald method
NVT	Canonical ensemble
PMF	Potential of mean force
DPD	Dissipative particle dynamics
COM	Center of mass
$\Delta G_{(gas)}^o$	Free-energy difference of redox pairs in vacuum
$\Delta G_{(sol,cation)}^o$	Solvation free-energy of the oxidized form
$\Delta G_{(sol)}^o$	Solvation free-energy of the reduced form
$n$	Number of transferred electrons
$F$	Faraday constant

$E_{CpTM+Tube}$	Total energies of the CpTM/ pristine or B-doped CNT complexes
$E_{CpTM}$	Total energies of the CpTM ligands
$E_{Tube}$	Total energies of the CNTs
$E_{Graphene}$	Total energies of the graphene supports
$E_{CpTM+Graphene}$	Total energies of the CpTM/ pristine or B-doped graphene complexes
$\Delta\rho$	Deformation charge density
$\rho_{CpTM/CNT}$	Charge density of the CpTM/CNT complex
$\rho_{CpTM}$	Charge density of the CpTM complex
$\rho_{CNT}$	Charge density of the CNT
$BD_{TM-B}$	Transition metal-boron atom binding distance
$BD_{TM-C}$	Transition metal-carbon atom binding distance
$\mu_B$	Magnetic moment
$\Delta G_{(gas)}^o$	Free-energy difference of redox pairs in vacuum
$\Delta G_{(sol)}^o$	Free-energy difference of redox pairs in solution
$\Delta G_{(sol,complex)}^o$	Solvation free-energy of the reduced complex
$\Delta G_{(sol,complex\ cation)}^o$	Solvation free-energy of the oxidized complex
$u_{LJ}$	12-6 style LJ potential function
$r$	Distance between two B-CNT surfaces
$\varepsilon$	Energy parameter for LJ or Stockmayer potential
$\sigma$	Length parameter for LJ or Stockmayer potential
$u_{Stockmayer}$	Stockmayer potential function
$c$	Third parameter of Stockmayer potential function

$\Delta A_{PMF}$	PMF of a single water molecule
$k_B$	Boltzmann constant
$T$	Temperature
$\rho(r)$	The density of water at specific position $r$
$\rho_{Bulk}$	The density of bulk water

## ACKNOWLEDGMENTS

In the beginning, I am most indebted to my advisor, Heath Turner, for his help, guidance, and encouragement. His wisdom in research and kindly support really has made my research experience enlightening and enjoyable.

I am also grateful to my committee members: Yuping Bao, Jason E. Bara, Ryan L. Hartman, and Claudia K. A. Mewes for their valuable suggestions on my research projects and my dissertation.

I would like to thank to my lab members, alumni, and colleagues: Wei An, Haining Liu, and Ryan Hamilton for the friendship and help during my life at UA.

I also would like to thank the faculty, staff, and graduate students of the Department of Chemical and Biological Engineering at the University of Alabama, for their help and support. I would like to thank the NSF and the Alabama Supercomputer Center for their funding and computational support on my research projects.

Finally, I would like to thank my family members: my wife, Yingying, and my parents for their support and encouragement on my life and emotion. I also would like to thank my lovely son, Matt, for his sweetness and giving me happiness.

## CONTENTS

ABSTRACT .....	ii
DEDICATION .....	iv
LIST OF ABBREVIATIONS AND SYMBOLS .....	v
ACKNOWLEDGMENTS .....	x
LIST OF TABLES .....	xiv
LIST OF FIGURES .....	xv
1. INTRODUCTION .....	1
1.1 Motivation.....	1
1.2 Objectives .....	4
1.3 Overview of computational methods .....	5
1.4 Overview of our work.....	6
References.....	10
2. STRUCTURAL AND ELECTRONIC PROPERTIES OF CARBON NANOTUBES AND GRAPHENES FUNCTIONALIZED WITH CYCLOPENTADIENE–TRANSITION METAL COMPLEXES: A DFT STUDY.....	15
2.1 Introduction.....	15
2.2 Computational details .....	18
2.3 Results and discussion .....	20
2.3.1 Geometries .....	20
2.3.2 Energetics.....	23

2.3.3 Electronic structures.....	25
2.3.4 Interaction of O <sub>2</sub> with the CpFe/B-CNT (8,0) complex.....	29
2.4 Conclusions.....	30
References.....	32
Appendix A.....	48
<b>3. REDOX PROPERTIES OF GRAPHENES FUNCTIONALIZED WITH CYCLOPENTADIENE–TRANSITION METAL COMPLEXES: A POTENTIAL REDOX-ACTIVE MATERIAL .....</b>	<b>66</b>
3.1 Introduction.....	66
3.2 Computational methods and models.....	69
3.3 Results and discussions.....	71
3.3.1 Geometries and energetics .....	71
3.3.2 Redox potentials of CpFe/pristine, N-doped, and B-doped graphene complexes .....	74
3.3.3 Redox potentials of CpCo and CpNi/B-doped graphene complexes .....	76
3.3.4 Charge transfer and frontier orbital analysis of the redox process ...	77
3.4 Conclusions.....	79
References.....	81
Appendix B.....	94
<b>4. WATER-INDUCED INTERACTIONS BETWEEN BORON-DOPED CARBON NANOTUBES.....</b>	<b>97</b>
4.1 Introduction.....	97

4.2 Computational methods .....	100
4.3 Results and discussions.....	103
4.3.1 Partial charge calculation.....	103
4.3.2 CNT-CNT interactions in vacuum.....	104
4.3.2.1 MD simulations.....	104
4.3.2.2 Coarse grain model parameterization .....	105
4.3.3 CNT-CNT interactions in water.....	106
4.3.4 Water density profile and hydration properties .....	110
4.4 Conclusions.....	111
References.....	113
Appendix C.....	132
5. SUMMARY .....	144
6. FUTURE WORK.....	147
References.....	153

## LIST OF TABLES

2.1. Calculated minimum binding distance between the CpTM ligand and the substrate.....	36
2.2. Calculated magnetic moment per supercell corresponding to several of the systems.....	37
A1. Binding energies of different CpTMs adsorbed on pristine/B-doped CNTs and graphenes .....	48
B1. Benchmarks of our computational method .....	94
4.1. Simulation parameters of different B-CNT and CNT systems .....	118
4.2. Fitted parameters for B-CNT pairs for LJ and Stockmayer potential functions.....	119
C1. Calculated geometry and partial charges of BC-I model .....	132

## LIST OF FIGURES

1.1. Representative structures: (a) B-CNT(6,6), (b) ferrocene, and (c) CpTM/B-CNT complex.....	9
2.1. Optimized geometries of CpFe on CNT/B-CNT complexes.....	38
2.2. Binding energies of different CpTMs adsorbed on pristine/B-doped CNTs and graphenes. ....	39
2.3. Calculated density of states (DOS) for CpTM/B-CNT (8,0) complexes .....	40
2.4. Calculated density of states (DOS) for CpTM/B-CNT (6,6) complexes .....	41
2.5. Calculated density of states (DOS) for CpTM/CNT (8,0) complexes .....	42
2.6. Calculated density of states (DOS) for CpTM/CNT (6,6) complexes .....	43
2.7. Calculated density of states (DOS) for CpFe/B-CNT (8,0) and CpFe/CNT (8,0) complexes .....	44
2.8. Optimized structures and NBO partial charges of CpFe/BC <sub>5</sub> graphenecomplexes (H atoms are omitted for clarity).....	45
2.9. Optimized geometries of an O <sub>2</sub> molecule on a CpFe/B-CNT (8,0) complex.....	46
2.10. a) Plotted 3D-deformation charge density isosurface of CpFe/B-CNT (6,6) complex, b) Cross section of the system, c) cross section of the deformationcharge density across the iron atom and Cp ring. d) ELF cross sectionof the CpFe/B-CNT (6,0) complex .....	47
A1. Optimized structures and NBO partial charges of CpFe/B-C graphene complexes (H atoms are omitted for clarity).....	49

A2. Optimized structures and NBO partial charges of CpFe/C <sub>70</sub> graphene omplexes (H atoms are omitted for clarity). .....	50
A3. Optimized structures of CpTM/B-CNT (6,6) complexes. ....	51
A4. Optimized structures of CpTM/CNT(6,6) complexes. ....	52
A5. Optimized structures of CpTM/B-CNT(8,0) complexes. ....	53
A6. Optimized structures of CpTM/CNT(8,0) complexes. ....	54
A7. Calculated band structures of CpTM/B-CNT(6,6) complexes. ....	55
A8. Calculated band structures of CpTM/CNT(6,6) complexes. ....	56
A9. Calculated band structures of CpTM/B-CNT(8,0) complexes. ....	57
A10. Calculated band structures of CpTM/CNT(8,0) complexes. ....	58
A11. a) Plotted 3D-deformation charge density isosurface of CpFe/CNT (6,6) complex, b) cross section of the system, c) cross section of the deformation charge density across the iron atom and Cp ring and d) ELF cross section of the CpFe/B-CNT (6,0) complex.....	59
A12. a) Plotted 3D-deformation charge density isosurface of CpFe/B-CNT (8,0) complex, b) cross section of the system, c) cross section of the deformation charge density across the iron atom and Cp ring and d) ELF cross section of the CpFe/B-CNT (6,0) complex.....	60
A13. a) Plotted 3D-deformation charge density isosurface of CpFe/CNT (8,0) complex, b) cross section of the system, c) cross section of the deformation charge density across the iron atom and Cp ring and d) ELF cross section of the CpFe/B-CNT (6,0) complex.....	61
A14. a) Plotted 3D-deformation charge density isosurface of CpCo/B-CNT (6,6) complex, b) cross section of the system, c) cross section of the deformation charge density across the cobalt atom and Cp ring. ....	62
A15. a) Plotted 3D-deformation charge density isosurface of	

CpCr/B-CNT (6,6) complex, b) cross section of the system, c) cross section of the deformation charge density across the chromium atom and Cp ring.....	63
A16. a) Plotted 3D-deformation charge density isosurface of CpCu/B-CNT (6,6) complex, b) cross section of the system, c) cross section of the deformation charge density across the copper atom and Cp ring.....	64
A17. a) Plotted 3D-deformation charge density isosurface of CpNi/B-CNT (6,6) complex, b) cross section of the system, c) cross section of the deformation charge density across the nickel atom and Cp ring.....	65
3.1. Optimized structures of a) BGr support; b) Gr support; c) NGr support; d) BC5Gr support; E) CpFe/BGr in water; f) CpFe/Gr in water; g) CpFe/NGr in water; h) CpFe/BGr in water with vinyl sidechain on the Cp ring; i) CpCo/BGr in water; and j) CpNi/BGr in water.....	85
3.2. Thermodynamic cycle used for the redox potential calculation. ....	86
3.3. Binding energies of different neutral and positive charged complexes in water. ....	87
3.4. 2D LOL plot of a) the neutral CpFe/BGr and b) charged CpFe <sup>+1</sup> /BGr in water. ....	88
3.5. Redox potential of CpTM complexes with different TMs, sidechains, and solvents.....	89
3.6. 3D-deformation charge density isosurface of a) CpFe/BGr complex; b) CpFe/Gr complex; and c) CpFe/NGr complex after the redox process. ....	90
3.7. 3D orbital isosurface of CpFe/BGr complexes in water.....	91
3.8. 3D orbital isosurface of CpFe/Gr and CpFe/NGr complexes in water.....	92
3.9. NBO partial charges of: a) charged CpFe <sup>+1</sup> /BGr; b) charged CpFe <sup>+1</sup> /Gr; and c) charged CpFe <sup>+1</sup> /NGr in water. ....	93

B1. 2D LOL plot of the neutral CpFe/Gr in water. ....	95
B2. 2D LOL plot of the neutral CpFe/NGr in water.....	96
4.1. a) Side view and b) top view of the B-CNT(6,6) supercell with the BC <sub>5</sub> doping pattern (BC-I). c) DFT-calculated DDEC partial charge results. d) Side view and e) top view of the B-CNT(6,6) supercell with B <sub>3</sub> doping pattern (BC-II). f) Side view and g) top view of B-CNT(10,10) supercell with the BC <sub>5</sub> doping pattern (BC-III). h) Side view and i) top view of B-CNT(12,12) supercell with the BC <sub>5</sub> doping pattern (BC-IV). ....	120
4.2. Simulation boxes containing (a) one B-CNT, (b) two B-CNTs and (c) three B-CNTs in a bundle, showing the dimensions of the simulation box and the arrangements of B-CNT (6,6) with the BC <sub>5</sub> doping pattern (BC-I).....	121
4.3. Partial charge distributions of the B atoms along the c-axis of the BC-I model obtain by DDEC (solid circles) and CHELPG (hollow circles). ....	122
4.4. The calculated PMFs of nanotube pairs in vacuum from MD simulations. ....	123
4.5. PMF of B-CNT(6,6) with a BC <sub>5</sub> doping pattern (BC-I) and fitted potentials, showing the PMF data (black solid circles), Stockmayer fit (red hollow circles), and LJ fit (black hollow circles). ....	124
4.6. PMFs of B-CNT(6,6) (BC-I) and pristine CNT(6,6) (C-I) in water (solid lines) and vacuum (dashed lines) calculated from MD simulation.....	125
4.7. Total and decomposed PMFs of B-CNT(6,6) with the BC <sub>5</sub> doping pattern (BC-I), showing the total PMF (black solid line), the Coulomb contribution of PMF (red dashed line) and the LJ contribution of PMF (black dashed line). ....	126
4.8. The trends of the PMFs' first minima, first maxima, and second minima energy vs. the tube diameter of BC-I, BC-III, and BC-IV models (with BC <sub>5</sub> doping patterns).....	127

4.9. Illustration of hysteresis corresponding to the expansion and compression PMFs of three C-I and BC-I nanotube bundles. ....	128
4.10. 2D and 3D density profiles of solvated BC-I pairs.....	129
4.11. 2D and 3D density profile of solvated C-I pairs.....	130
4.12. Radial PMF of single water molecule around pristine CNT and B-CNT.....	131
C1. a) geometry and b) CHELPG partial charges of the cluster model of (6, 6) BC <sub>5</sub> B-CNT.....	134
C2. 2D density profile of three CNT bundles expansion and compression at 1.38 nm. (a) B-CNT expansion. (b) B-CNT compression. (c) CNT expansion. (d) CNT compression.....	135
C3. LJ and Stockmayer potential fitting of MD calculated PMFs of BC-III model (B-CNT(10,10) with BC <sub>5</sub> doping pattern).....	136
C4. LJ and Stockmayer potential fitting of MD calculated PMFs of BC-IV model (B-CNT(12,12) with BC <sub>5</sub> doping pattern). ....	137
C5. LJ and Stockmayer potential fitting of MD calculated PMFs of BC-II model (B-CNT(6,6) with B <sub>3</sub> doping pattern).....	138
C6. Total and decomposed PMFs of B-CNT(6,6) with B <sub>3</sub> doping pattern (BC-II), showing the total PMF(purple), the Coulomb contribution of PMF(red) and the LJ contribution of PMF (dashed blue).....	139
C7. Total and decomposed PMFs of B-CNT(10,10) with BC <sub>5</sub> doping pattern (BC-III), showing the total PMF(purple), the Coulomb contribution of PMF(red) and the LJ contribution of PMF (dashed blue).....	140
C8. Total and decomposed PMFs of B-CNT(12,12) with BC <sub>5</sub> doping pattern (BC-IV), showing the total PMF(purple), the Coulomb contribution of PMF(red) and the LJ contribution of PMF(blue).....	141
C9. PMFs of solvated BC-I pair with DDEC and CHELPG calculated	

partial charges. ....	142
C10. Average number of hydrogen-bond per water molecule around pristine CNT and B-CNT.....	143
6.1. a) Proposed N-containing five-member rings, b) BEs of different N-containing five-member rings/Fe/B-CNT(8,0) complexes, c) Optimized geometry of pyrazoleFe/B-CNT(8,0) complex. ....	150
6.2. Optimized geometry of a porphyrinFe/B-CNT complex.....	151
6.3. PM6 scan of a porphyrinFe/B-CNT complex.....	152

## CHAPTER 1

### INTRODUCTION

#### 1.1 Motivation

Modern electrochemical applications in energy generation, storage and sensing call for new high performance electrochemical materials. The objectives of designing novel nanomaterials, which combine the support/electrode materials as well as redox/catalytic active centers, include strong stability, appropriate redox potential, high conductivity, and dispersibility. Among the support material candidates, boron-doped nanocarbons (including fullerenes, carbon nanotubes (CNT), and graphenes) demonstrate exceptional properties, as the substitutional doping provides the following benefits. First, many transition metals (TMs) as well as other catalytic active centers can be stabilized on B-doped nanocarbons. Meanwhile, the catalytic properties can also be tuned, due to the metal-support interaction. Our group has conducted a series of calculations on the stabilization of transition metals and organometallic complexes on the doped nanocarbons.<sup>1-9</sup> For instance, the binding energy of single TM atoms and cyclopentadienyl(Cp)/TM/B-doped nanocarbons is more than double the binding energy on pristine nanocarbon supports.<sup>3, 7</sup> Experiments using Pt/B-doped carbon supports also exhibit better corrosion and CO resistance than pristine carbon.<sup>6</sup> Moreover, the *p*-type doping of B atoms increases the conductivity of nanocarbons drastically.<sup>3</sup> The calculated band structures of B-doped CNTs (B-CNTs) reveal that B-doping can turn semi-conductive nanotubes into conductors, as well as increased the conductivity of metallic nanotubes.<sup>3</sup> In addition, the doping process renders more defects with B-doped nanocarbons, and these sites may act as active

catalytic centers and provide more intimate contact with the enzymes in electrochemical sensing.<sup>6, 10-13</sup> For instance, using B-CNT as the electrode material with glucose oxidase as the glucose sensor, Deng et al. found improved sensitivity and stability, versus pristine CNT.<sup>10</sup> Last but not least, B-CNTs are found to be dispersed more easily than pristine CNTs, with or without surfactants, in aqueous solution.<sup>14</sup> Therefore, various electrochemical systems with B-doped nanocarbon materials have been reported, including fuel cells,<sup>15</sup> batteries,<sup>16</sup> solar cells,<sup>17</sup> electrochemical sensors,<sup>10</sup> and electrochemical double-layer capacitors (EDLC),<sup>18</sup> etc. In particular, our group has conducted extensive investigations of B-doped nanocarbons as a CO tolerant catalyst, as a gas sensor, and within nanoelectronics.<sup>2-6, 19</sup>

Ferrocene is a sandwich-like molecule with two Cp rings on both sides and an iron atom in the center. Since its discovery,<sup>20</sup> ferrocene and other metallocenes have drawn great interests in catalysis, solar energy generation, hydrogen storage, cancer therapy, random access memory (RAM), and nano-magnetism.<sup>21-23</sup> In particular, ferrocene-based compounds are important electron donor-acceptors, which means that they can be oxidized or reduced back and forth easily in an electrochemical system. For example, ferrocene can provide and accept electrons from various enzymes in electrochemical sensing applications, such as glucose, glycolate, amino-acid and other bio-molecules.<sup>10, 24, 25</sup> In addition, the low redox barrier of ferrocene makes it an ideal component in nonvolatile resistive RAM, which stores a data bit by altering the resistance of a redox cell.<sup>8, 9, 26</sup> However, due to the nature of ferrocene and other metallocenes, immobilizing those redox active species on the surface of an electrode is a challenge.<sup>27</sup>

Therefore, by combining the properties of B-doped nanocarbons and ferrocene-based redox-active materials, the hypothesis of this work is that ferrocene-like organometallic active centers

can be stabilized on B-doped nanocarbons (Figure 1.1). In fact, recent theoretical and experimental studies found the existence and potential applications of similar complexes, which show fundamental properties analogues to our current systems.<sup>28-35</sup> For example, using density functional theory (DFT) methods, Plachinda et al.<sup>28</sup> reported that the attachment of metal-arene complexes onto graphene turned the band gap of graphene from a semimetal into a semiconductor. Moreover, Zhao et al.<sup>29</sup> characterized benzene/TM/B/N-doped graphene complexes by DFT methods, and found that these complexes show good stability, tunable electronic and magnetic structures, and enhanced O<sub>2</sub> adsorption properties. Other organometallic/nanocarbon complexes have also been synthesized by experimentalists, such as CpTM/fullerene,<sup>31</sup> CpTM/annulene, CpTM/sumanene,<sup>32, 33</sup> benzene/Cr/CNT and graphene<sup>34</sup> complexes. These past successes indicate that it would be experimentally feasible to synthesize CpTMs on carbon supports. Moreover, due to the redox-active nature of ferrocene-based compounds, as well as the high stability and good conductivity of B-doped nanocarbons, it is envisioned that CpTM/B-doped nanocarbon could be used as a novel redox-active material, which integrates the redox-active CpTM center onto the B-doped nanocarbon.

In addition to the stabilization and physical/chemical properties, the homogenous dispersion of nanocarbons (with varying sizes and chiralities) is considered to be a major challenge. Nanocarbons need to be well dispersed before effectively separating, purifying and incorporating these materials into their final applications. However, due to the strong van der Waals interactions between nanocarbons and their hydrophobic solvation behavior, most nanocarbons are known to aggregate after synthesis.<sup>36</sup> To better disperse nanocarbons in solution, many additives have been used, including surfactants,<sup>37-39</sup> dyes,<sup>40</sup> polymers,<sup>41</sup> and biomolecules.<sup>42</sup> In addition, computational studies of nanocarbon dispersions have been

reported using molecular dynamics (MD) simulations.<sup>43-45</sup> However, most of those studies are focused on the dispersion of pristine nanocarbons, where the reports of doping effects on the dispersion properties are scarce. Blackburn et al. reported an experimental investigation of pristine and boron-doped CNTs (B-CNTs) dispersed in aqueous solution with/without surfactants.<sup>14</sup> Raman spectroscopy was used to identify that the B-CNTs are more easily dispersed than the pristine CNTs. This finding implies that substitutional doping may be an effective route for dispersing or separating CNTs. However, the mechanism of the doped nanocarbon dispersion is currently not clear, and to the best of our knowledge, no following studies have been reported. Therefore, an MD simulation study can clarify the water-induced interactions and solvation behaviors of B-doped nanocarbons, which may lead to improved materials and techniques for achieving stable nanocarbon dispersion.

## 1.2 Objectives

The goal of the present work is to computationally design novel nanomaterials based on organometallic compounds and doped nanocarbons for electrochemical applications. These nanostructures are intended to possess the following properties:

(a) High stability, as the organometallic active centers can be stabilized on the pristine or doped nanocarbons, which directly linked to the sintering, corrosion, and poisoning resistance. Also, B-doped nanocarbons can stabilize active centers which are not stable on pristine supports. An important criterion of the stability is the binding energy obtained from the DFT calculations.

(b) Suitable electrochemical properties, several electrochemical characteristics are important for these complexes, such as suitable redox potentials, conductivities, band structures, and catalytic activities.

(c) Stable dispersions, as the dispersibility is a major challenge for all nanocarbon materials, better solubility and reagglomeration resistant is desired for the candidate complexes.

### 1.3 Overview of computational methods

In this work, a multiscale simulation approach is used to characterize and evaluate the stability, properties, and dispersion of our prototype materials. These simulations include both first-principles DFT and classical MD simulations.

The quantum mechanics (QM) simulations can model a relatively small scale system (the upper limit is about a thousand of atoms and 100ps) by solving the Schrödinger equation (Kohn-Sham equation in DFT calculations) to obtain the electronic structure and fundamental properties. Many properties of ground states and excited states can be calculated, such as the electronic energy, band structure, molecular orbitals (MO), optimized geometry, vibrational frequencies, and transition states of a reaction. With respect to the traditional ab initio methods like Hartree-Fock,<sup>46</sup> DFT is more computationally efficient, as the scaling is approximately  $N^3$  ( $N$  is equivalent to the total number of the electrons) in cases where the linear scaling algorithms are available.<sup>47-49</sup> However, one big challenge of DFT is that the results are not systematically improvable with the functional. In other words, as the complexity of the functional grows (from the local density approximation (LDA),<sup>50</sup> to the generalized gradient approximation (GGA),<sup>51</sup> or to the hybrid-GGA like B3LYP<sup>52</sup>), the accuracy is not always improved. Thus, choosing a reliable level of theory is a key aspect of the DFT calculations. In this work, we use the generalized gradient approximation (GGA) functional of Perdew, Burke, and Ernzerhof (PBE),<sup>51</sup> combined with the projector-augmented wave (PAW)<sup>53</sup> method to calculate the properties of the periodic models. For the cluster models, the B3LYP hybrid-GGA functional is used.<sup>52</sup> Both

functionals have been well-tested in organometallic-nanocarbons system analogous to ours.<sup>28, 29</sup> In addition, the redox properties can also be evaluated by the DFT calculations. Using a solvation model such as the conductor-like polarizable continuum model (CPCM),<sup>54</sup> the free-energy changes of solvated and vacuum redox pairs can be evaluated with DFT calculations.

In order to simulate larger system and to obtain thermodynamic and transport properties, MD simulation can model systems of up to millions of atoms and several ms of time. By calculating the interaction of atoms using empirical potential energy functions and by propagating the system using Newtonian equations of motion, the MD simulations are capable of capturing many thermodynamics properties, like heat capacity, solvation properties, PVT behavior, surface tension, solubility, as well as transport properties, such as the diffusion coefficients and the thermal conductivity of complex system. These advantages make MD an ideal choice to study the dispersion behavior of nanocarbons in solution.<sup>43-45, 55-57</sup> However, the reliability of MD heavily depends upon the forcefield parameters used in the simulations. While the Lennard-Jones parameters for B-doped nanocarbons have been developed by Kang et al.,<sup>58</sup> the strongly polarized B-C bonds need to be parameterized with electrostatic interactions. Thus, we have developed a forcefield containing partial charges on atom sites from first-principle DFT calculations in order to describe the coulomb interactions of B-doped nanocarbons. Various population analysis methods are used to attribute the electron density to individual atomic sites. These methods often rely on molecular orbitals,<sup>59</sup> the topology of the electronic density,<sup>60</sup> and fitting to the electrostatic potentials (ESP).<sup>61</sup> In our work, both CHELPG and DDEC methods are used to parameterize the partial charges within the B-CNT materials.

## 1.4 Overview of our work

In this work, we start by testing the stability of the CpTM/B-doped nanocarbons as a first step, in search of more stable electrochemical materials with redox activities. DFT calculations are used to evaluate the structural and electronic properties of CpTM (TM=Fe, Co, Cr, Cu, Ni) adsorbed on pristine or doped nanocarbons (CNTs and graphenes). These first row TMs are chosen based on the stability of their metallocene counterparts, as well as their potential electrochemical and catalytic applications.<sup>27, 34, 62</sup> Remarkable stabilization of the CpTM complexes on the B-CNTs is found, even surpassing the BEs of single TM atom adsorption,<sup>3</sup> which are often considered as an upper limit of the adsorption energy. The band structure, charge transfer, and O<sub>2</sub> adsorption properties are also included in our work.

The next step is to evaluate the CpFe/B-doped nanocarbon as an integrated redox active electrode material. Because of the broad application of ferrocene-based compounds as redox mediators in electrochemical systems, our design goal is that these novel complexes should have redox potentials close to a ferrocene molecule, while still maintaining the high stability and conductivity of the B-doped support. As the stability and conductivity are confirmed in the second part of our work, we then focus on screening the redox potential of the CpTM adsorbed on pristine, B-doped, and N-doped nanocarbons with different doping patterns, solvents, and doping concentration. Using population analyses and deformation charge density analyses, the mechanism of charge transfer is also clarified.

In addition, the solvation behavior of the B-CNTs with varying diameters, doping patterns, and doping concentrations are investigated using MD simulations. The B-CNTs are modeled using partial charge sites parameterized from DFT calculations. The potential of mean force (PMF) of compressing and expanding two and three B-CNT bundles is calculated in order to reveal the dispersibility and the reagglomeration resistance of these materials. Moreover, we

analyze the water-CNT interactions by extracting the PMF of individual water molecules and by quantifying the average number of hydrogen bonds near the water-nanotube interface. In addition, models of B-CNT interactions are parameterized for future coarse-grain simulations, which can be used to model much larger systems.

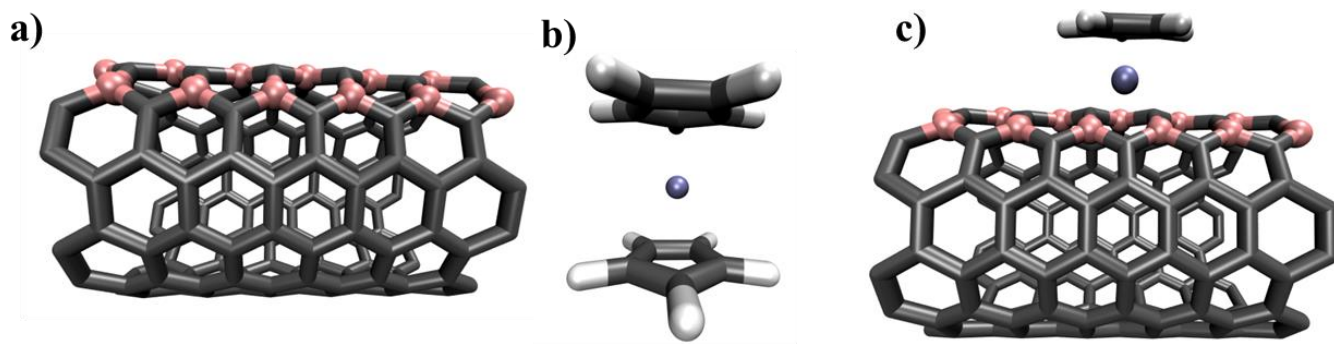


**Figure 1.1.** Representative structures: (a) B-CNT(6,6), (b) ferrocene, and (c) CpTM/B-CNT complex

## References

- (1) Acharya, C. K.; Turner, C. H. Stabilization of Platinum Clusters by Substitutional Boron Dopants in Carbon Supports. *Journal of Physical Chemistry B* **2006**, *110*, 17706-17710.
- (2) Acharya, C. K.; Sullivan, D. I.; Turner, C. H. Characterizing the Interaction of Pt and PtRu Clusters with Boron-Doped, Nitrogen-Doped, and Activated Carbon: Density Functional Theory Calculations And Parameterization. *Journal of Physical Chemistry C* **2008**, *112*, 13607-13622
- (3) An, W.; Turner, C. H. Structural, Electronic, and Magnetic Features of Platinum Alloy Strings Templated on a Boron-Doped Carbon Nanotube. *Physical Review B* **2010**, *81*, 8
- (4) An, W.; Turner, C. H. Transition-Metal Strings Templated on Boron-Doped Carbon Nanotubes: A DFT Investigation. *Journal of Physical Chemistry C* **2009**, *113*, 15346-15354.
- (5) An, W.; Turner, C. H. Chemisorption of Transition-Metal Atoms on Boron- and Nitrogen-Doped Carbon Nanotubes: Energetics and Geometric and Electronic Structures. *Journal of Physical Chemistry C* **2009**, *113*, 7069-7078.
- (6) Acharya, C. K.; Li, W.; Liu, Z. F.; Kwon, G.; Turner, C. H.; Lane, A. M.; Nikles, D.; Klein, T.; Weaver, M. Effect of Boron Doping in the Carbon Support on Platinum Nanoparticles and Carbon Corrosion. *Journal of Power Sources* **2009**, *192*, 324-329.
- (7) Zhang, Z. T.; Turner, C. H. Structural and Electronic Properties of Carbon Nanotubes and Graphenes Functionalized with Cyclopentadienyl-Transition Metal Complexes: A DFT Study. *Journal of Physical Chemistry C* **2013**, *117*, 8758-8766.
- (8) Choi, T. L.; Lee, K. H.; Joo, W. J.; Lee, S.; Lee, T. W.; Chae, M. Y. Synthesis and Nonvolatile Memory Behavior of Redox-Active Conjugated Polymer-Containing Ferrocene. *Journal of the American Chemical Society* **2007**, *129*, 9842.
- (9) Jin, C.; Lee, J.; Lee, E.; Hwang, E.; Lee, H. Nonvolatile Resistive Memory Of Ferrocene Covalently Bonded to Reduced Graphene Oxide. *Chemical Communications* **2012**, *48*, 4235-4237.
- (10) Deng, C. Y.; Chen, J. H.; Chen, X. L.; Mao, C. H.; Nie, L. H.; Yao, S. Z. Direct Electrochemistry of Glucose Oxidase and Biosensing for Glucose Based on Boron-Doped Carbon Nanotubes Modified Electrode. *Biosensors & Bioelectronics* **2008**, *23*, 1272-1277.
- (11) Borowiak-Palen, E.; Rummeli, M.; Gemming, T.; Knupfer, M.; Kalenczuk, R. J.; Pichler, T. Formation of Novel Nanostructures Using Carbon Nanotubes as a Frame. *Synthetic Metals* **2005**, *153*, 345-348.
- (12) Golberg, D.; Bando, Y.; Han, W.; Kurashima, K.; Sato, T. Single-walled B-doped Carbon, B/N-Doped Carbon and BN Nanotubes Synthesized from Single-Walled Carbon Nanotubes through a Substitution Reaction. *Chemical Physics Letters* **1999**, *308*, 337-342.
- (13) Radovic, L. R.; Karra, M.; Skokova, K.; Thrower, P. A. The Role of Substitutional Boron in Carbon Oxidation. *Carbon* **1998**, *36*, 1841-1854.
- (14) Blackburn, J. L.; Engtrakul, C.; McDonald, T. J.; Dillon, A. C.; Heben, M. J. Effects of Surfactant and Boron Doping on the BWF Feature in the Raman Spectrum of Single-Wall Carbon Nanotube Aqueous Dispersions. *Journal of Physical Chemistry B* **2006**, *110*, 25551-25558.
- (15) Wang, J. J.; Chen, Y. G.; Zhang, Y.; Ionescu, M. I.; Li, R. Y.; Sun, X. L.; Ye, S. U.; Knights, S. 3D Boron Doped Carbon Nanorods/Carbon-Microfiber Hybrid Composites: Synthesis and Applications in a Highly Stable Proton Exchange Membrane Fuel Cell. *Journal of Materials Chemistry* **2011**, *21*, 18195-18198.

- (16) Wu, Z. S.; Ren, W. C.; Xu, L.; Li, F.; Cheng, H. M. Doped Graphene Sheets As Anode Materials with Superhigh Rate and Large Capacity for Lithium Ion Batteries. *ACS Nano* **2011**, *5*, 5463-5471.
- (17) Zhu, H. W.; Wei, J. Q.; Wang, K. L.; Wu, D. H. Applications of Carbon Materials in Photovoltaic Solar Cells. *Solar Energy Materials and Solar Cells* **2009**, *93*, 1461-1470.
- (18) Wang, D. W.; Li, F.; Chen, Z. G.; Lu, G. Q.; Cheng, H. M. Synthesis and Electrochemical Property of Boron-Doped Mesoporous Carbon in Supercapacitor. *Chemistry of Materials* **2008**, *20*, 7195-7200.
- (19) An, W.; Wu, X. J.; Yang, J. L.; Zeng, X. C. Adsorption and Surface Reactivity on Single-Walled Boron Nitride Nanotubes Containing Stone-Wales Defects. *Journal of Physical Chemistry C* **2007**, *111*, 14105-14112.
- (20) Kealy, T. J.; Pauson, P. L. A New Type of Organo-Iron Compound. *Nature* **1951**, *168*, 1039-1040.
- (21) Long, N. J. *Metallocenes : an introduction to sandwich complexes*. Blackwell Science: Oxford, OX ; Malden, MA, USA, 1998.
- (22) Wu, X. J.; Zeng, X. C. Double Metallocene Nanowires. *Journal of the American Chemical Society* **2009**, *131*, 14246
- (23) Zhang, X. Y.; Wang, J. L.; Gao, Y.; Zeng, X. C. Ab Initio Study of Structural and Magnetic Properties of TMn(ferrocene)(n+1) (TM = Sc, Ti, V, Mn) Sandwich Clusters and Nanowires (n = infinity). *ACS Nano* **2009**, *3*, 537-545.
- (24) Cass, A. E. G.; Davis, G.; Francis, G. D.; Hill, H. A. O.; Aston, W. J.; Higgins, I. J.; Plotkin, E. V.; Scott, L. D. L.; Turner, A. P. F. Ferrocene-mediated Enzyme Electrode for Amperometric Determination of Glucose. *Analytical Chemistry* **1984**, *56*, 667-671.
- (25) Dicks, J. M.; Aston, W. J.; Davis, G.; Turner, A. P. F. Mediated Amperometric Biosensors for D-galactose, Glycolate and L-amino-acids Based on a Ferrocene-modified Carbon Paste Electrode. *Analytica Chimica Acta* **1986**, *182*, 103-112.
- (26) Roth, K. M.; Yasserli, A. A.; Liu, Z. M.; Dabke, R. B.; Malinovskii, V.; Schweikart, K. H.; Yu, L. H.; Tiznado, H.; Zaera, F.; Lindsey, J. S.; Kuhr, W. G.; Bocian, D. F. Measurements of Electron-Transfer Rates of Charge-Storage Molecular Monolayers On Si(100). Toward Hybrid Molecular/Semiconductor Information Storage Devices. *Journal of the American Chemical Society* **2003**, *125*, 505-517.
- (27) Cossi, M.; Iozzi, M. F.; Marrani, A. G.; Lavecchia, T.; Galloni, P.; Zanoni, R.; Decker, F. Measurement and DFT Calculation of Fe(Cp)(2) Redox Potential in Molecular Monolayers Covalently Bound to H-Si(100). *Journal of Physical Chemistry B* **2006**, *110*, 22961-22965.
- (28) Plachinda, P.; Evans, D. R.; Solanki, R. Electronic Properties of Metal-AreneFunctionalized Graphene. *Journal of Chemical Physics* **2011**, *135*, 044103.
- (29) Zhao, J. X.; Yu, Y. Y.; Bai, Y.; Lu, B.; Wang, B. X. Chemical Functionalization of BN Graphene with the Metal-Arene Group: A Theoretical Study. *Journal of Materials Chemistry* **2012**, *22*, 9343-9350.
- (30) Avdoshenko, S. M.; Ioffe, I. N.; Cuniberti, G.; Dunsch, L.; Popov, A. A. Organometallic Complexes of Graphene: Toward Atomic Spintronics Using a Graphene Web. *Acs Nano* **2011**, *5*, 9939-9949.

- (31) Dai, J.; Zhao, Y.; Wu, X. J.; Zeng, X. C.; Yang, J. L. Organometallic Hexahapto-Functionalized Graphene: Band Gap Engineering with Minute Distortion to the Planar Structure. *Journal of Physical Chemistry C* **2013**, *117*, 22156-22161.
- (32) Nakamura, E.; Koshino, M.; Saito, T.; Niimi, Y.; Suenaga, K.; Matsuo, Y. Electron Microscopic Imaging of a Single Group 8 Metal Atom Catalyzing C-C Bond Reorganization of Fullerenes. *Journal of the American Chemical Society* **2011**, *133*, 14151-14153.
- (33) Amaya, T.; Sakane, H.; Hirao, T. A Concave-bound CpFe Complex of Sumanene as a Metal in a Pi Bowl. *Angewandte Chemie-International Edition* **2007**, *46*, 8376-8379.
- (34) Petrukhina, M. A. Coordination of Buckybowls: The First Concave-bound Metal Complex. *Angewandte Chemie-International Edition* **2008**, *47*, 1550-1552.
- (35) Sarkar, S.; Niyogi, S.; Bekyarova, E.; Haddon, R. C. Organometallic Chemistry of Extended Periodic Pi-Electron Systems: Hexahapto-Chromium Complexes of Graphene and Single-Walled Carbon Nanotubes. *Chemical Science* **2011**, *2*, 1326-1333.
- (36) Henrard, L.; Hernandez, E.; Bernier, P.; Rubio, A. van der Waals interaction in Nanotube Bundles: Consequences on Vibrational Modes. *Physical Review B* **1999**, *60*, 8521-8524.
- (37) Islam, M. F.; Rojas, E.; Bergey, D. M.; Johnson, A. T.; Yodh, A. G. High Weight Fraction Surfactant Solubilization of Single-Wall Carbon Nanotubes In Water. *Nano Letters* **2003**, *3*, 269-273.
- (38) Moore, V. C.; Strano, M. S.; Haroz, E. H.; Hauge, R. H.; Smalley, R. E.; Schmidt, J.; Talmon, Y. Individually Suspended Single-Walled Carbon Nanotubes in Various Surfactants. *Nano Letters* **2003**, *3*, 1379-1382.
- (39) Arnold, M. S.; Green, A. A.; Hulvat, J. F.; Stupp, S. I.; Hersam, M. C. Sorting Carbon Nanotubes by Electronic Structure Using Density Differentiation. *Nature Nanotechnology* **2006**, *1*, 60-65.
- (40) Hu, C. G.; Chen, Z. L.; Shen, A. G.; Shen, X. C.; Li, H.; Hu, S. S. Water-soluble Single-Walled Carbon Nanotubes via Noncovalent Functionalization by a Rigid, Planar and Conjugated Diazo Dye. *Carbon* **2006**, *44*, 428-434.
- (41) O'Connell, M. J.; Boul, P.; Ericson, L. M.; Huffman, C.; Wang, Y. H.; Haroz, E.; Kuper, C.; Tour, J.; Ausman, K. D.; Smalley, R. E. Reversible Water-Solubilization of Single-Walled Carbon Nanotubes by Polymer Wrapping. *Chemical Physics Letters* **2001**, *342*, 265-271.
- (42) Nakashima, N.; Okuzono, S.; Murakami, H.; Nakai, T.; Yoshikawa, K. DNA Dissolves Single-walled Carbon Nanotubes in Water. *Chemistry Letters* **2003**, *32*, 456-457.
- (43) Tummala, N. R.; Striolo, A. SDS Surfactants on Carbon Nanotubes: Aggregate Morphology. *Acs Nano* **2009**, *3*, 595-602.

- (44) Tummala, N. R.; Morrow, B. H.; Resasco, D. E.; Striolo, A. Stabilization of Aqueous Carbon Nanotube Dispersions Using Surfactants: Insights from Molecular Dynamics Simulations. *ACS Nano* **2010**, *4*, 7193-7204.
- (45) Walther, J. H.; Jaffe, R. L.; Kotsalis, E. M.; Werder, T.; Halicioglu, T.; Koumoutsakos, P. Hydrophobic Hydration of C-60 and Carbon Nanotubes in Water. *Carbon* **2004**, *42*, 1185-1194.
- (46) Hartree, D. R. The Wave Mechanics of an Atom with a Non-Coulomb Central Field. Part I. Theory and Methods. *Mathematical Proceedings of the Cambridge Philosophical Society* **1928**, *24*, 89-110.
- (47) Skylaris, C. K.; Haynes, P. D.; Mostofi, A. A.; Payne, M. C. Introducing ONETEP: Linear-scaling Density Functional Simulations on Parallel Computers. *Journal of Chemical Physics* **2005**, *122*, 084119.
- (48) Hohenberg, P.; Kohn, W. Inhomogeneous Electron Gas. *Physical Review B* **1964**, *136*, B864-B871.
- (49) Kohn, W.; Sham, L. J. Self-Consistent Equations Including Exchange and Correlation Effects. *Physical Review* **1965**, *140*, A1133-A1138.
- (50) Vosko, S. H.; Wilk, L.; Nusair, M. Accurate Spin-Dependent Electron Liquid Correlation Energies for Local Spin-Density Calculations - A Critical Analysis. *Canadian Journal of Physics* **1980**, *58*, 1200-1211.
- (51) Perdew, J. P.; Burke, K.; Ernzerhof, M. Generalized Gradient Approximation Made Simple. *Physical Review Letters* **1996**, *77*, 3865-3868.
- (52) Becke, A. D. Density-Functional Thermochemistry.3. The Role of Exact Exchange. *Journal of Chemical Physics* **1993**, *98*, 5648-5652.
- (53) Blochl, P. E.; Jepsen, O.; Andersen, O. K. Improved Tetrahedron Method for Brillouin-Zone Integrations. *Physical Review B* **1994**, *49*, 16223-16233.
- (54) Barone, V.; Cossi, M. Quantum Calculation of Molecular Energies and Energy Gradients in Solution by a Conductor Solvent Model. *Journal of Physical Chemistry A* **1998**, *102*, 1995-2001.
- (55) Li, L. W.; Bedrov, D.; Smith, G. D. Water-induced Interactions between Carbon Nanoparticles. *Journal of Physical Chemistry B* **2006**, *110*, 10509-10513.
- (56) Lin, S. C.; Blankschtein, D. Role of the Bile Salt Surfactant Sodium Cholate in Enhancing the Aqueous Dispersion Stability of Single-Walled Carbon Nanotubes: A Molecular Dynamics Simulation Study. *Journal of Physical Chemistry B* **2010**, *114*, 15616-15625.

- (57) Uddin, N. M.; Capaldi, F. M.; Farouk, B. Molecular Dynamics Simulations of the Interactions And Dispersion of Carbon Nanotubes in Polyethylene Oxide/Water Systems. *Polymer* **2011**, *52*, 288-296.
- (58) Kang, J. W.; Hwang, H. J. Comparison of C-60 Encapsulations into Carbon and Boron Nitride Nanotubes. *Journal of Physics-Condensed Matter* **2004**, *16*, 3901-3908.
- (59) Reed, A. E.; Curtiss, L. A.; Weinhold, F. Intermolecular Interactions from a Natural Bond Orbital, Donor-Acceptor Viewpoint. *Chemical Reviews* **1988**, *88*, 899-926.
- (60) Bader, R. F. W. A Quantum-Theory of Molecular-Structure and Its Applications. *Chemical Reviews* **1991**, *91*, 893-928.
- (61) Breneman, C. M.; Wiberg, K. B. Determining Atom-Centered Monopoles from Molecular Electrostatic Potentials - The Need for High Sampling Density in Formamide Conformational-Analysis. *Journal of Computational Chemistry* **1990**, *11*, 361-373.
- (62) Otero, R.; Calleja, F.; Garcia-Suarez, V. M.; Hinarejos, J. J.; de la Figuera, J.; Ferrer, J.; de Parga, A. L. V.; Miranda, R. Tailoring Surface Electronic States via Strain to Control Adsorption: O/Cu/Ru(0001). *Surface Science* **2004**, *550*, 65-72.

## CHAPTER 2

### STRUCTURAL AND ELECTRONIC PROPERTIES OF CARBON NANOTUBES AND GRAPHENES FUNCTIONALIZED WITH CYCLOPENTADIENE–TRANSITION METAL COMPLEXES: A DFT STUDY\*

#### 2.1. Introduction

Since its discovery in 1951,<sup>1</sup> ferrocene ( $\text{Cp}_2\text{Fe}$ , where Cp = cyclopentadienyl) has attracted considerable interest in organometallic chemistry. Nowadays, metallocene  $\text{Cp}_2\text{TM}$ -based compounds (where TM = transition metal) have been widely used in catalysis, solar energy generation, hydrogen storage, cancer therapy, and nano-magnetism.<sup>2-4</sup> This is due, in part, to the novel electronic, structural, magnetic, and transport properties of metallocenes.<sup>3-8</sup> As a result, great interest has been focused on experimental studies of the complexes between metallocenes and other molecules or structures, such as single-walled carbon nanotubes (SWCNTs).<sup>9-13</sup>

In addition to experimental techniques, computational methods are powerful tools for understanding the properties of these important molecules. Recently, several computational studies of benzene/metal/graphene complexes have been reported.<sup>6-8</sup> These compounds are structurally very similar to CpTM complexes, so their fundamental properties are expected to provide reasonable analogues to our current systems. For example, in 2011, by using density functional theory (DFT) methods, Plachinda et al.<sup>6</sup> predicted that the attachment of metal-arene complexes onto graphene leads to an increase in the band gap of graphene, and hence, turns it

---

\* Reprinted with permission from Journal of Physical Chemistry C, 2013, Volume 117, Page 8758-8766. Copyright 2013 American Chemical Society.

from a semimetal into a semiconductor. Furthermore, Zhao et al.<sup>7</sup> used DFT methods to characterize benzene+metal+BN graphene complexes. It was found that these complexes show good stabilities, tunable electronic and magnetic structures, and enhanced O<sub>2</sub> adsorption characteristics. Although these studies provide insights into the properties of related organic-metal complexes, the electronic and geometric structures of CpTM adsorbed on CNTs and graphene substrates are still unknown.

A potential advantage of our CpTM/carbon complexes is their enhanced stability, which is particularly important for their application as catalysts. For example, most of the metallocene-based catalysts, such as ferrocenyl phosphines (which have been widely used as chiral catalysts in organic syntheses and pharmaceutical industries) are homogeneous catalysts.<sup>2</sup> For many industrial operations, immobilizing homogeneous catalysts can more easily accommodate the demands of continuous operation and minimize the need for down-stream separation processes. Previously, methods have been reported<sup>14</sup> for immobilizing metallocene-based or similar catalysts using chemical functionalization, such as pyridyl-functionalized fullerenes,<sup>15</sup> CNTs reacted with diazonium salts,<sup>14</sup> and the bonding of ligands with silica. These immobilization protocols include at least two steps: (a) functionalization of the support side chains, followed by; (b) attachment of ferrocene-based catalysts to the side chains. However, it may be more cost-efficient and/or environmentally-friendly to do a one-step modification to directly attach CpTMs onto a carbon support, versus performing a series of chemical functionalization steps.

In addition to potential applications in catalysis, the immobilized Cp groups can also be functionalized with different side chains, rendering useful material platforms for sensing and biomedical applications. For example, boron-doped CNTs (B-CNTs) can be modified by attaching CpTM complexes functionalized with drug molecules (antigens to target cancer cells).

These complexes can be used as targeted agents for boron neutron capture therapy (BNCT) of cancer,<sup>16,17</sup> which benefits from both the high selectivity of the antigens and the ability of the CNTs to penetrate cell membranes.<sup>18</sup> However, to the best of our knowledge, no systematic study has been dedicated to understand and quantify the interactions between CpTM ligands and large  $\pi$ -conjugated systems, such as the CNTs and graphenes reported here.

Recently, the experimental synthesis of similar organic-metal complexes has been performed, such as CpTM/fullerene,<sup>19</sup> CpTM/annulene, and CpTM/sumanene,<sup>20,21</sup> and benzene/Cr/SWCNT and graphene<sup>22</sup> complexes, which suggests the possibility of directly immobilizing CpTMs on carbon supports. One potential challenge of the direct immobilization route is instability (due to the weak binding between the metallocene and pristine carbon), which may become problematic at high temperatures.<sup>19</sup> However, our previous work<sup>23-26</sup> has shown that doped nanocarbon supports (like boron-doped fullerenes, CNTs, and graphenes) may possess elevated binding energies with transition metals, leading to improved chemical stability. Therefore, it may be possible to use substitutionally-doped nanocarbon supports to immobilize ferrocene-based molecules, leading to increased stability, and possibly, useful catalytic and/or sensor properties.

In this paper, we report a theoretical study on the structural and electronic properties of CpTM (TM=Fe, Co, Cr, Cu, Ni) and pristine or boron-doped single-walled CNTs and graphenes. These first row TMs are selected because of the wide applications of their Cp<sub>2</sub>TM or benzene-metal complex counterparts in catalysis, as well as in the areas of nanoelectronics and nanomagnetism. Specifically, iron is one of our focus metals, as it is a commonly used (as the stable metal center of ferrocene), and so it serves as a baseline for the other CpTM complexes in our study. In addition to iron, cobalt and nickel are chosen because of their large atomic

magnetic momenta. Due to the tuning of the band structure of BN graphene<sup>7</sup> and the experimental synthesis of benzene/Cr/SWCNT complexes,<sup>22</sup> CpCr/CNT complexes are also presented in our work. Finally, to further explore the potential applications of CpTM/CNT complexes as a catalyst and/or gas sensor, copper is included in our study as a potential catalyst for the oxygen reduction reaction (ORR).<sup>27</sup>

## 2.2. Computational details

In this paper, all calculations on pristine and boron-doped CNTs were performed with first-principles DFT methods using the Vienna ab-initio simulation package (VASP).<sup>28,29</sup> Specifically, the generalized gradient approximation (GGA) functional of Perdew, Burke, and Ernzerhof (PBE),<sup>30</sup> combined with the projector-augmented wave (PAW)<sup>31</sup> method, were used in the calculations. Two types of pristine and boron-doped CNT models were used, based on our previous work,<sup>26,32</sup> corresponding to (6,6) and (8,0) structures. The boron-doped models correspond to our previous “Type-I” doping arrangement, such that the boron atoms are primarily doped along one side of the CNT (at a concentration of 9.375%). In our previous work other doping patterns were also explored, but regardless of the specific dopant arrangement, the same general effects were observed. Six unit cells of pristine and boron-doped CNTs are included in a hexagonal lattice ( $a=b=22$  Å, and  $a=b=18$  Å for CNT (6,6) and CNT (8,0), respectively), with 1-D periodic boundary conditions (PBC) along the tube axis (c axis). The unit cell sizes were sufficient for eliminating interactions between periodic images.

The initial configurations of the CpTM ligand and CNT complexes were modeled by placing single CpTM ligands on different adsorption sites (with initial configurations starting from hollow sites and from the most stable sites of single TM atom adsorption) on the outer

surfaces of four types of CNTs: pristine CNT (6,6), pristine CNT (8,0), B-CNT (6,6), and B-CNT (8,0). The energy cutoffs of the plane wave basis sets were chosen to be 400 eV in all the calculations. For the relaxation of pristine and boron-doped CNTs, as well as for the CpTM/CNT and CpTM/B-CNT complexes, the Brillouin zone integration was performed by using  $1 \times 1 \times 5$   $k$ -points within the Monkhorst-Pack scheme<sup>33</sup> and first-order Methfessel-Paxton smearing of 0.2 eV.<sup>34</sup> All of the configurations were fully relaxed without constraints using the conjugate-gradient method, with the convergence threshold set to  $10^{-4}$  eV for the total energy and  $10^{-2}$  eV/Å in force on each atom. The densities of states (DOS) and band structures of these relaxed structures were calculated using finer  $1 \times 1 \times 10$   $k$ -points to shed light on the electronic structures of our complexes. The binding energies (BE) between the CpTM ligands and the CNTs were defined as:

$$BE = E_{CpTM} + E_{Tube} - E_{CpTM+Tube} \quad (1)$$

where  $E_{CpTM+Tube}$ ,  $E_{CpTM}$ , and  $E_{Tube}$  are the total energies of the complexes, the CpTM ligands, and the CNTs, respectively. Therefore, a positive binding energy indicates an attractive interaction between the CpTM ligand and the CNT.

To further expand our discussion to the CpTM graphene complexes and reveal details of the interaction between CpTMs and doped nanocarbons, the interaction between CpTM complexes and pristine/B-doped graphenes were investigated with DFT calculations using the Gaussian 09 package.<sup>35</sup> Three models of pristine and B-doped graphenes were used in our work:  $BC_5$  ( $C_{58}B_{12}$ ), and single B atom substituted  $C_{69}B$  graphene (referred to as B-C), and pristine graphene ( $C_{70}$ ), as in our previous work.<sup>23</sup> The adsorption geometry and energy were calculated at the B3LYP/6-31G level of theory.<sup>36</sup> The binding energies are calculated in the same manner as in the CpTM/CNT complexes:

$$BE = E_{CpTM} + E_{Graphene} - E_{CpTM+Graphene} \quad (2)$$

In addition, natural bond orbital (NBO) population analyses, deformation charge density plots, and electron localization function (ELF) plots were used to approximate the charge distribution in our systems, in order to provide additional insight into the interaction details.<sup>37-39</sup> The deformation charge density is defined as:

$$\Delta\rho = \rho_{CpTM/CNT} - \rho_{CpTM} - \rho_{CNT} \quad (3)$$

where  $\rho_{CpTM/CNT}$ ,  $\rho_{CpTM}$ , and  $\rho_{CNT}$  are the charge densities of the CpTM/CNT complex, CpTM complex, and CNT, respectively. The ELF indicates the probability density of finding an electron (with the same spin) near a reference electron at a given position. For perfectly localized electrons, the ELF is equal to unity. The ELF enables quantitative interpretations and direct visualizations of the electron locations in a molecular system, which provides further information about the interactions and bonding.

Calculating the non-bonding interactions between  $sp^2$  conjugated molecules like organic molecule-graphene complexes or graphene bilayers is challenging. Previous DFT calculations using the local density approximation (LDA) tend to overestimate the binding,<sup>40,41</sup> but due to a cancellation of errors in the non-bonded interaction energy, the results are fairly consistent with higher-level calculations. In our work, the TM-carbon interactions are the main contributor to the BE. Therefore, for consistency with previous calculations involving TM adsorption on carbon, a GGA (PBE) and a hybrid-GGA (B3LYP) functional are chosen for all the system in this paper.

## 2.3. Results and discussion

### 2.3.1 Geometries

The optimized geometries of CpFe adsorbed on CNT and B-CNT complexes are shown in Figure 2.1 with TM=Co, Cr, Cu, Ni shown in Figure A3-A6 (Supporting Information). The adsorption geometries are in general agreement with previous computational results of TM/CNT complexes<sup>26,42</sup> and of benzene/metal/graphene complexes.<sup>6-8</sup>

For CpTM/B-CNT complexes, the TM atoms adsorb on or near the hollow sites that contain both C and B atoms, forming multiple TM-C and TM-B bonds. The TM-B and TM-C binding distances between the TM atoms and the B or C are in the same range or slightly shorter than isolated TMs adsorbed on B-CNT (e.g., 1.78 and 1.98 Å for the shortest Fe-C and Fe-B distances on CpFe/B-CNT (8,0), respectively, as compared with 1.89 Å for Fe-C and 2.09 Å for Fe-B for single Fe adsorption), using the same level of theory.<sup>26</sup> Moreover, the binding distances of the TM atoms on the B-CNTs are shorter than the benzene/metal on BN or pristine graphene complexes. For example, the TM-C distance of benzene/Fe/pristine graphene and the TM-B distance of benzene/Fe/BN graphene are 2.36 and 2.43 Å, respectively.<sup>6,7</sup> The shorter TM-B or C distances indicate a stronger binding of the CpFe complex with B-CNT, versus the single Fe atom. The TM-B and TM-C binding distances ( $BD_{\text{TM-B}}$  and  $BD_{\text{TM-C}}$ ) are shown in Table 2.1. In addition, the average distances between the TM atoms and the C atoms of the Cp ring generally follow the order of the metallocene counterparts. From Cr to Cu, the TM-Cp distances increase with the number of  $3d$  electrons from 2.06 Å to 2.26 Å for all of the complexes, and these values agree with the experimental results and high-level calculations of isolated metallocene molecules.<sup>43,44</sup> Also, the trends of the TM-C distance of the CpTM/CNT complexes agree with previous work of single TM adatoms on CNTs.<sup>26,42</sup> Interestingly, the TM-C bonds of CpTM/B-CNTs are shorter than those corresponding to the CpTM/CNTs, suggesting that boron-doping

may indeed enhance the TM-substrate interactions, which also was observed in single TM adsorption.<sup>7</sup>

The most stable adsorption sites of the CpTM ligands on CNTs are quite different from single TM adatoms, which may energetically favor top, bridge or hollow sites (depending on the TM).<sup>26,42</sup> On the contrary, the following characteristics are observed for the CpTM adsorption:

- Most CpTM complexes occupy the hollow sites of the six-member ring center. This includes: TM=Fe and Cr on all four kinds of pristine and doped CNTs, TM=Ni, Co on B-CNT (6,6) and TM=Co CNT (6,6)
- Some complexes adsorb near the center on the sidewall. This includes TM=Ni on CNT (6,6), and TM=Co on B-CNT (8,0), CNT (6,6), and CNT (8,0).
- Some exceptions to the previous predictions are found: TM=Cu on B-CNT (8,0) and B-CNT (6,6) are adsorbed near the boron atoms. TM=Cu on CNT (6,6) also favors the top sites. Adsorption near the C-C bridge site or near the C atoms are favored for TM=Cu on CNT (8,0) and TM=Ni on CNT (8,0), respectively.

The trends of the adsorption sites are generally consistent with the geometries of benzene<sub>2</sub>/TM complexes, in which the Cr and Fe favor the center of two benzene rings, the benzene rings are shifted in the Ni complexes, and the Cu complexes are unstable.<sup>45</sup>

For all three CpFe/graphene complexes, the CpFe complexes stay in the hollow center, with a slightly longer distance (approximately 2.3 Å for the TM-B or TM-C distance), indicating weaker interactions than within the CpFe/CNT complexes. This is confirmed by the BE values shown in Figure 2.2 (details of each BE are shown in Table A1 of the Supplementary Information). The geometry (along with the NBO partial charges) of the CpFe/BC<sub>5</sub> graphene is

shown in Figure 2.8, and the CpFe/B-C and pristine graphene are shown in Figures A1 and A2 of the Supporting Information.

### 2.3.2 Energetics

According to previous work, for most TM atoms in magnetic ground states, spin-restricted DFT calculations tend to overestimate the BEs between the TM and pristine CNT.<sup>26,42</sup> Therefore, spin-polarized DFT calculations are preferable for modeling CpTM/CNT complexes. Large binding energies are predicted for CpTM on the pristine CNTs and on the B-CNTs (Figure 2.2). The values are higher than benzene/metal on BN or pristine graphene complexes,<sup>6,7</sup> even surpassing the BEs of the single metal adsorbates.<sup>26,42</sup> For instance, the BEs of FeCp on B-CNT (8,0), B-CNT (6,6), CNT (8,0), and CNT (6,6) are increased by 2.05 eV, 2.32 eV, 1.56 eV, and 1.09 eV, respectively, as compared to the BEs of single Fe atoms on the same substrates.<sup>26,42</sup>

Amongst the systems that we studied, CpCr/B-CNT (8,0) has the strongest BE, followed by Cp(Fe,Co,Ni) complexes on B-CNT (8,0), followed by the BE of CpCu/B-CNT (8,0). This same trend (among adsorbates) was also found in B-CNT (6,6) complexes. However, the BEs on pristine CNT (8,0) show a different trend, as the BEs of CpFe complexes are the strongest, and the BEs of Fe, Co, and Ni were stronger than that of Cr. The BE trends of Fe, Co, Ni, and Cu are consistent with the stabilities of their metallocene counterparts.<sup>44</sup> Also, we note that the magnitude of the BE enhancement on B-CNT (8,0) is higher than those on B-CNT (6,6), similar to previous calculations on the adsorption of single TM atoms.<sup>26</sup> This phenomenon can be explained by the fact that the local geometry strain on the CNT side wall imparts enhanced reactivity for B-CNT (8,0), since its structure possesses greater curvature.<sup>46</sup> The correlations between local curvature and reactivity has been previously identified with pristine CNTs,<sup>47</sup> B-

CNTs,<sup>26</sup> and CBNNTs.<sup>46</sup> Chen, *et al.* showed that the cause of this effect is the increase of the pyramidalization angles induced by the curvature, leading to deviations from  $sp^2$  to  $sp^3$  hybridization.<sup>47</sup> In our work, we predict stronger charge transfer with respect to increased curvature, as seen by comparing the deformation charge density plot of CpFe/B-CNT(8,0) (Figure A12) with that of CpFe/B-CNT(6,6) (Figure 2.10). In addition, the strong BEs, such as 6.22 eV for CpFe on B-CNT (8,0), indicates a very strong stabilization on boron-doped CNTs (stronger than the C-C bonds within the CNT itself).<sup>42</sup> Such strong interactions may lead to new routes for generating stable, covalently-functionalized CNTs. For the  $BC_5$ , B-C, and  $C_{70}$  graphene clusters, strong BEs of 3.00 eV, 2.02 eV, and 1.01 eV are also observed, which are 2.29 eV, 1.36 eV, and 0.30 eV higher than single Fe adatom adsorption on graphene,<sup>48</sup> respectively.

The geometry and relative stabilities of metallocenes and benzene<sub>2</sub>/metal complexes can be rationalized with the well-known 18 electron rule.<sup>44,45</sup> For example, ferrocene has 18 valence electrons (VEs), and it is therefore a very stable complex. Cobaltocene and nickelocene have 19 and 20 VEs, respectively, so they are less stable than ferrocene, but they can still be synthesized because of the stabilizing electrostatic interactions of the Cp and TM. Since copper has a  $d^{10}$  electron configuration, the cuprocene complex is unstable and cannot be experimentally synthesized. However, within complexes of CpTM on CNTs or graphenes, the large  $\pi$ -conjugated substrates can redistribute the excess electrons. The redistributions of electrons within the pristine and B-doped CNTs complexes can be directly observed in the deformation charge density plots (Figures 2.10 and A11–A17). Most of the CpTMs favor adsorption at the hollow sites, and this may also be attributed to the formation of additional TM- $d$  and B/C- $p$  interactions, similar to the 18 VE ferrocene.

There are weak  $\pi$ -stacking interactions between the Cp ring and the CNT or graphene that can also contribute to the BEs (and overall stability). However, due to the nature of GGA functionals, which tend to underestimate the interactions between a Cp ring and a CNT or graphene sheet,<sup>40</sup> our complexes may be slightly more stable than the calculated BEs predict. The  $\pi$ -stacking interactions between benzene and graphene (separated by a 4 Å binding distance, comparable to the distances in our systems) have been predicted to contribute about 0.1 eV to the total binding energy.<sup>41</sup>

Our spin-polarized DFT calculations reveal the quenching effects on the magnetic momenta ( $\mu$ ) of the TMs (see Table 2.2), due to the strong interactions and multiple chemical bonds between the TMs and the CNTs. The magnetic momenta per supercell are quenched to zero or less than 1  $\mu$ B for most CpTM/CNT complexes, except for Cr, which shows a magnetic momentum of around 1.1 to 1.55  $\mu$ B for different complexes. Compared with the magnetic momenta of pristine TMs on CNTs,<sup>26</sup> the addition of the Cp ring further quenches the magnetic moments of the CpTM/CNT complexes, even on the pristine CNTs, which have weaker interactions with the CpTM adsorbates.

### 2.3.3 *Electronic structures*

The spin-polarized DOS and projected DOS (PDOS) of CpTM/CNTs complexes were calculated to shed light on the interactions between the CpTMs and the CNTs, as well as evaluate the potential applications of these materials (in nanoelectronics, spintronic devices, and sensors). In addition, deformation charge density and ELF plots of CpFe on B-CNT and CNT are shown in Figures 2.10 and A11 – A17. Our previous work on TM/B-CNT adsorption

predicted a variety of resonance behavior in the energy levels of TM-*d* and C/B-*p* from the DOS plots, as well as tunable metallicities.<sup>26</sup>

The DOS and PDOS of all 20 species are drawn in the -5 to 3 eV range, in order to show the electronic structures near the Fermi level. However, for a large supercell with PBCs, it is challenging to discuss all of the band structure features for such a great numbers of bands in one diagram, except for the direct and indirect band gaps (calculated band structures are shown in Figures A7-A10). Thus, we mainly focus on the DOS and PDOS in our discussions. In addition, the PDOS of CpFe/B-CNT and the NBO partial charges of CpFe/BC5 graphene are plotted, in order to shed light on the comparative interactions between Cp rings and single-walled CNTs.<sup>37</sup>

Generally speaking, as shown in Figure 2.3, the CpTM/B-CNT (8,0) complexes retain the metallic properties of B-CNT (8,0), but with slightly decreased metallicities. The exception is for CpCo/B-CNT (8,0) complexes, which have a Co-*d* peak across the Fermi level on the PDOS, increasing its metallicity. From the PDOS plots, strong interactions among the C-*p*, B-*p*, and TM-*d* are observed, and the positions of these interactions vary depending upon the specific TM. Therefore, similar to the single TM adsorption cases,<sup>26</sup> the C-*p*, B-*p*, and TM-*d* interactions are responsible for the enhanced chemisorption of CpTM complexes. Interestingly, the positions of maximum overlap between the B-*p* and C-*p* states with the TM-*d* states are changed by the presence of the Cp ring. For instance, the copper atom has a filled 3*d* orbital, and thus the binding between the Cu atom and the CNTs are weaker than other third row transition metals with open *d* shells. Moreover, the violation of the 18-electron rule prevents the stability of the cuprocene complex. However, for CpCu/B-CNT (8,0), the maximum overlap occurs at -3 eV to -4 eV, compared to a peak at -2.1 eV in the case of the single Cu adatom on B-CNT (8,0).<sup>26</sup> Also, as compared to the Cu adatom on B-CNT (8,0), a wider TM-*d* peak is observed with the

CpCu/B-CNT (8,0) complex, indicating that the presence of the Cp ring renders a more delocalized TM-*d* state, which may be a primary factor leading to the enhanced adsorption (compared to the single atom adsorption or metallocene).

For CpTM/B-CNT (6,6) complexes, the PDOS plots (Figure 2.4) reveal similar adsorption characteristics for the CpTM/B-CNT (6,6) complexes. Albeit, the quenching of the magnetic momenta is slightly weaker than in the CpTM/B-CNT (8,0) complexes. The effects of the different TMs show different tuning effects on the electronic structure of the complexes. For instance, with TM = Fe, Cr, and Ni, large peaks across the Fermi level indicate increased metallicities of the complexes, whereas with TM = Co and Cu, this phenomenon is not observed. In addition, according to our deformation charge density calculations, the difference in BEs can be correlated to the charge transfer (shown in Figures A14-A17). Species with the strongest BEs like Cr or Fe show increased charge transfer between the TM atom, CNT, and Cp ring, while more weakly bound species (i.e., Cu) show less charge transfer.

Interestingly, the presence of CpTM complexes turns the semi-conductive CNT (8,0) more metallic (Figure 2.5). In particular, CpCo/CNT (8,0) exhibits a conductive band structure. The tuning effect is caused by the presence of the *d*-band peak of the TMs across the Fermi level. For other CpTM/CNT (8,0) complexes, band gap narrowing is observed. These tunable band structures, combined with the stable chemisorption, may indicate potential applications of CpTM/CNT complexes in nanoelectronics. However, for weaker interactions between CpTM ligands and pristine CNTs, the magnetic momenta of TMs are less likely to be quenched. The metallicity of CNT (6,6) (Figure 2.6) is also enhanced by the chemisorption of CpTMs, except for TM = Cu, which has a small band gap, (where the Cu-*d* peak is not located near the Fermi level).

To further study the role of Cp and TM interactions, the PDOS of Fe-*d*, C-*p*, or B-*p* state of the B-CNTs, and the C-*p* states of the Cp ring are shown in Figure 2.7 (a). In the figure, evidence of interactions between the Cp ring and the CNTs is observed, as multiple resonance peaks between the C-*p* states of the Cp ring and the B/C-*p* states of the CNT are found (in the range of -3 to -10 eV). The binding between the Cp rings and Fe atoms are obviously the Fe-*d* and C-*p* interactions, as shown in the range of -3 to 0 eV. Moreover, the detailed PDOS of CpFe/CNT (8,0) (Figure 2.7 (b)) projects a more localized C-*p* peak of the Cp ring carbon atoms at about -3 eV, compared to the CpFe/B-CNT (8,0) case. Thus, two possible contributions may explain the enhanced chemisorptions, according to the PDOS analyses. First, the interactions between the Fe-*d* and C-*p* of the Cp ring, as well as the boron-doping delocalize the TM-*d* orbital (more *d* peaks and wider *d* peaks, as compared with the previously-reported<sup>26</sup> single TM atom cases), making it easier to interact with the C-*p* and B-*p* of the CNT. The charge transfer between the Cp ring, TM atom, and CNT are visualized in our deformation charge density plots, indicating the involvement of the Cp ring in the adsorption. Moreover, the delocalized TM-*d* orbitals can be seen in the ELF plots, where the less localized electrons (lower ELF values) around the Fe atom form multiple bonds with the Cp ring and CNT. In addition, the direct Cp-CNT interactions also contribute to the enhanced binding. Tournus et al.<sup>41</sup> reported a systematic study on the interactions between organic compounds and single-walled CNTs, where weak physisorption and minor modifications of the band structures were found. Both the delocalization of TM-*d* orbitals and weak interactions can contribute to the charge transfer on the Cp ring, as shown in the deformation charge density and ELF plots. However, quantitative evaluation of the weak interactions between the Cp ring and carbon supports should be performed with high-level quantum mechanical calculations.

Our NBO analyses provide further insights into the interactions in our systems (NBO partial charges of CpFe/BC<sub>5</sub>, CpFe/B-C, and CpFe/C<sub>70</sub> graphene complexes are shown in Figure 2.8, Figure A1, and Figure A2, respectively). For pristine C<sub>70</sub>, B-C and BC<sub>5</sub> graphene complexes, the partial charge of the Fe atom increases slightly by the addition of the B atoms, from 0.80 e<sup>-</sup> to 0.98 e<sup>-</sup>. However, the partial charges of the C atoms near the adsorption site on the graphene decrease drastically with the boron-doping, and this charge imbalance may provide a large contribution to the enhanced BE. Similar effects were reported by Groves et al.,<sup>49</sup> in which the electron-deficient boron atoms cause the conjugated orbitals of the carbon to become more localized (since the B atom prevents the formation of a delocalized double bond), and therefore, enhance the interaction between the TMs and graphene. Moreover, our deformation charge density plots show more charge transfer between CpFe and B-CNT than for the pristine CNT, which further supports our NBO analysis. This effect can also be observed in our PDOS plots, as wider, more delocalized C-*p* and B-*p* peaks are found in the B-doped CNTs. Also, our ELF plots indicate direct bonding between B/C and the TM atoms.

#### *2.3.4 Interaction of O<sub>2</sub> with the CpFe/B-CNT (8,0) complex*

Previously, the interactions between an O<sub>2</sub> adsorbate molecule with both a benzene/V/BN graphene complex and with a boron-doped nanotube were studied computationally, showing potential applications as an ORR catalyst and for other reactions involving oxygen.<sup>7,50</sup> Yang et al. reported that the charge transfer between the carbon and boron atoms lead to a chemisorption of O<sub>2</sub> on B-CNT (5,5) with a binding energy of -0.11 eV.<sup>50</sup> Also, for the benzene/V/BN graphene complex, the presence of the benzene/V ligand enhanced the reactivity of the BN graphene, with respect to O<sub>2</sub>.<sup>7</sup>

Consequently, due to the similarity between our CpTM/B-CNT complexes and previous systems, we conducted a preliminary investigation of the interaction of an O<sub>2</sub> molecule with the CpFe/B-CNT (8,0) system. Relaxation of the O<sub>2</sub> molecule adsorbed on the CpFe/B-CNT (8,0) complex (at the same level of theory as our other spin-polarized plane-wave DFT calculations) gives a molecular chemisorption of O<sub>2</sub> on the nanotube, as well as a dissociative chemisorption (Figure 2.9). The BEs of the O<sub>2</sub> and CpFe/B-CNT (8,0) complex of the chemisorption and the dissociative chemisorption cases are 0.28 eV and 3.67 eV, respectively. For the chemisorption case, the O<sub>2</sub> molecule is parallel to the CNT, with an O-C distance of 1.43 Å. The O-O bond distance is elongated to 2.55 Å, compared with 1.21 Å of free O<sub>2</sub>.<sup>7</sup> The O-O bond distortion and the shorter O-C distance indicates that the CpFe/B-CNT (8,0) complex may be a better catalyst, as compared to a pristine boron-doped CNT.<sup>50</sup> For the dissociative chemisorption case, the relaxation predicts a dissociative chemisorption geometry, with the O-O distance lengthened to 3.67 Å, the O-C distances are 1.40 Å and 1.43 Å, and the O-B distances are 1.40 Å and 1.48 Å, respectively.

## 2.4 Conclusions

In summary, we have conducted a systematic characterization on the geometry, energetic, and electronic properties of CpTM (TM=Fe, Ni, Co, Cr, Cu) ligands adsorbed on pristine and boron-doped single-walled CNT complexes and graphenes by using first-principles DFT calculations. The enhanced BEs of these complexes, as even compared with single atom adsorption on the same supports, demonstrates the strong stabilization effect caused by the presence of the Cp ring. The exceptional stability of CpTM/B-CNT complexes indicates a potential route for immobilizing metallocene-based catalysts. Our electronic structure

calculations demonstrate that the enhanced stabilization of the CpTM/B-CNTs (with respect to their metallocene counterparts) can be attributed to the delocalization of the TM-*d* electrons by the Cp ring, which enhances the interaction between the 2*p*-states of B and C and the *d*-states of the TM. Furthermore, there are additional (yet weaker)  $\pi$ -stacking interactions between the Cp ring and the carbon supports that may be captured with higher-level calculations.

In terms of properties, we predict tunable metallicities of the CpTM/CNT and CpTM/B-CNT complexes, which may enable these architectures to be useful for future nanoelectronics. In addition, our study on the interaction of an O<sub>2</sub> molecule with a CpFe/B-CNT (8,0) complex provides an initial indication of their potential catalytic applications. To further explore the properties and the applications of CpTM/carbon materials, future work should be dedicated to further characterize the electronic structures and catalytic reaction pathways of these systems. Also, the experimental synthesis of our CpTM/carbon structures would be particularly beneficial for characterizing their properties.

## **Acknowledgments**

Funding for this work was provided by an NSF CAREER Award (no. 0747690). Supercomputer resources were provided by the Alabama Supercomputer Center.

**Supporting Information Available:** Table of binding energies of different CpTMs adsorbed on pristine/B-doped CNTs and graphenes. Figures of the geometry and NBO partial charges of CpFe/B-C and pristine graphene; optimized structures of CpTM (TM=Co, Ni, Cr, Cu) / pristine and B-doped CNT complexes; calculated band structures of CpTM (TM=Co, Ni, Cr, Cu) / pristine and B-doped CNT complexes. This material is available in appendix A.

## References

- (1) Kealy, T. J.; Pauson, P. L. A New Type of Organo-Iron Compound. *Nature* **1951**, *168*, 1039.
- (2) Long, N. J. *Metallocenes : an introduction to sandwich complexes*; Blackwell Science: Oxford, OX ; Malden, MA, USA, 1998.
- (3) Wu, X. J.; Zeng, X. C. Double Metallocene Nanowires. *J. Am. Chem. Soc.* **2009**, *131*, 14246.
- (4) Zhang, X. Y.; Wang, J. L.; Gao, Y.; Zeng, X. C. Ab Initio Study of Structural and Magnetic Properties of  $TMn(\text{ferrocene})(n+1)$  ( $TM = \text{Sc, Ti, V, Mn}$ ) Sandwich Clusters and Nanowires ( $n = \text{infinity}$ ). *ACS Nano* **2009**, *3*, 537.
- (5) Zhang, X. Y.; Ng, M. F.; Wang, Y. B.; Wang, J. L.; Yang, S. W. Theoretical Studies on Structural, Magnetic, and Spintronic Characteristics of Sandwiched  $\text{EunCOT}_{n+1}$  ( $n=1-4$ ) Clusters. *ACS Nano* **2009**, *3*, 2515.
- (6) Plachinda, P.; Evans, D. R.; Solanki, R. Electronic Properties of Metal-Arene Functionalized Graphene. *J. Chem. Phys.* **2011**, *135*, 9.
- (7) Zhao, J. X.; Yu, Y. Y.; Bai, Y.; Lu, B.; Wang, B. X. Chemical Functionalization of BN Graphene with the Metal-Arene Group: A Theoretical Study. *J. Mater. Chem.* **2012**, *22*, 9343.
- (8) Avdoshenko, S. M.; Ioffe, I. N.; Cuniberti, G.; Dunsch, L.; Popov, A. A. Organometallic Complexes of Graphene: Toward Atomic Spintronics Using a Graphene Web. *ACS Nano* **2011**, *5*, 9939.
- (9) Kocsis, D.; Kaptas, D.; Botos, A.; Pekker, A.; Kamaras, K. Ferrocene Encapsulation in Carbon Nanotubes: Various Methods of Filling And Investigation. *Phys. Status Solidi B* **2011**, *248*, 2512.
- (10) Li, Y. C.; Chen, X. B.; Zhou, G.; Duan, W. H.; Kim, Y.; Kim, M.; Ihm, J. Trends in Charge Transfer and Spin Alignment of Metallocene on Graphene. *Phys. Rev. B* **2011**, *83*, 5.
- (11) Plank, W.; Pfeiffer, R.; Schaman, C.; Kuzmany, H.; Calvaresi, M.; Zerbetto, F.; Meyer, J. Electronic Structure of Carbon Nanotubes with Ultrahigh Curvature. *ACS Nano* **2010**, *4*, 4515.
- (12) Sceats, E. L.; Green, J. C. Noncovalent Interactions between Organometallic Metallocene Complexes and Single-Walled Carbon Nanotubes. *J. Chem. Phys.* **2006**, *125*, 12.
- (13) Sceats, E. L.; Green, J. C. Charge Transfer Composites of Bis(Cyclopentadienyl) and Bis(Benzene) Transition Metal Complexes Encapsulated in Single-Walled Carbon Nanotubes. *Phys. Rev. B* **2007**, *75*, 10.
- (14) Song, C. E.; Lee, S. G. Supported Chiral Catalysts on Inorganic Materials. *Chem. Rev.* **2002**, *102*, 3495.

- (15) Alvaro, M.; Atienzar, P.; la Cruz, P.; Delgado, J. L.; Troiani, V.; Garcia, H.; Langa, F.; Palkar, A.; Echegoyen, L. Synthesis, Photochemistry, and Electrochemistry of Single-Wall Carbon Nanotubes With Pendent Pyridyl Groups and of Their Metal Complexes with Zinc Porphyrin. Comparison with Pyridyl-Bearing Fullerenes. *J. Am. Chem. Soc.* **2006**, *128*, 6626.
- (16) Tiwari, R.; Mahasenan, K.; Pavlovicz, R.; Li, C. L.; Tjarks, W. Carborane Clusters in Computational Drug Design: A Comparative Docking Evaluation Using AutoDock, FlexX, Glide, and Surflex. *J. Chem. Inf. Model.* **2009**, *49*, 1581.
- (17) Johnsamuel, J.; Byun, Y.; Jones, T. P.; Endo, Y.; Tjarks, W. A New Strategy for Molecular Modeling and Receptor-Based Design of Carborane Containing Compounds. *J. Organomet. Chem.* **2003**, *680*, 223.
- (18) Chen, X.; Kis, A.; Zettl, A.; Bertozzi, C. R. A Cell Nanoinjector Based on Carbon Nanotubes. *Proc. Natl. Acad. Sci. U. S. A.* **2007**, *104*, 8218.
- (19) Nakamura, E.; Koshino, M.; Saito, T.; Niimi, Y.; Suenaga, K.; Matsuo, Y. Electron Microscopic Imaging of a Single Group 8 Metal Atom Catalyzing C-C Bond Reorganization of Fullerenes. *J. Am. Chem. Soc.* **2011**, *133*, 14151.
- (20) Amaya, T.; Sakane, H.; Hirao, T. A Concave-Bound Cpfe Complex of Sumanene as a Metal in a Pi Bowl. *Angew. Chem., Int. Ed.* **2007**, *46*, 8376.
- (21) Petrukhina, M. A. Coordination of Buckybowls: The First Concave-Bound Metal Complex. *Angew. Chem., Int. Ed.* **2008**, *47*, 1550.
- (22) Sarkar, S.; Niyogi, S.; Bekyarova, E.; Haddon, R. C. Organometallic Chemistry of Extended Periodic Pi-Electron Systems: Hexahapto-Chromium Complexes of Graphene and Single-Walled Carbon Nanotubes. *Chem. Sci.* **2011**, *2*, 1326.
- (23) Acharya, C. K.; Turner, C. H. Stabilization of Platinum Clusters by Substitutional Boron Dopants in Carbon Supports. *J. Phys. Chem. B* **2006**, *110*, 17706.
- (24) Acharya, C. K.; Sullivan, D. I.; Turner, C. H. Characterizing the Interaction of Pt and PtRu Clusters with Boron-Doped, Nitrogen-Doped, and Activated Carbon: Density Functional Theory Calculations and Parameterization. *J. Phys. Chem. C* **2008**, *112*, 13607.
- (25) Acharya, C. K.; Li, W.; Liu, Z. F.; Kwon, G.; Turner, C. H.; Lane, A. M.; Nikles, D.; Klein, T.; Weaver, M. Effect of Boron Doping in the Carbon Support on Platinum Nanoparticles and Carbon Corrosion. *J. Power Sources* **2009**, *192*, 324.
- (26) An, W.; Turner, C. H. Chemisorption of Transition-Metal Atoms on Boron- and Nitrogen-Doped Carbon Nanotubes: Energetics and Geometric and Electronic Structures. *J. Phys. Chem. C* **2009**, *113*, 7069.
- (27) Otero, R.; Calleja, F.; Garcia-Suarez, V. M.; Hinarejos, J. J.; de la Figuera, J.; Ferrer, J.; de Parga, A. L. V.; Miranda, R. Tailoring Surface Electronic States via Strain to Control Adsorption: O/Cu/Ru(0001). *Surf. Sci.* **2004**, *550*, 65.

- (28) Hobbs, D.; Kresse, G.; Hafner, J. Fully Unconstrained Noncollinear Magnetism within the Projector Augmented-Wave Method. *Phys. Rev. B* **2000**, *62*, 11556.
- (29) Kresse, G.; Furthmüller, Efficiency of Ab-Initio Total Energy Calculations for Metals and Semiconductors Using A Plane-Wave Basis Set. *J. Comput. Mater. Sci.* **1996**, *6*, 15.
- (30) Perdew, J. P.; Burke, K.; Ernzerhof, M. Generalized Gradient Approximation Made Simple. *Phys. Rev. Lett.* **1996**, *77*, 3865.
- (31) Blochl, P. E.; Jepsen, O.; Andersen, O. K. Improved Tetrahedron Method for Brillouin-Zone Integrations. *Phys. Rev. B* **1994**, *49*, 16223.
- (32) An, W.; Turner, C. H. Structural, Electronic, and Magnetic Features of Platinum Alloy Strings Templated on a Boron-Doped Carbon Nanotube. *Phys. Rev. B* **2010**, *81*, 8.
- (33) Monkhorst, H. J.; Pack, J. D. Special Points for Brillouin-Zone Integrations. *Phys. Rev. B* **1976**, *13*, 5188.
- (34) Methfessel, M.; Paxton, A. T. High-Precision Sampling for Brillouin-Zone Integration in Metals. *Phys. Rev. B* **1989**, *40*, 3616.
- (35) Frisch, M. J.; Trucks, G. W.; Schlegel, H. B.; Scuseria, G. E.; Robb, M. A.; Cheeseman, J. R.; Scalmani, G.; Barone, V.; Mennucci, B.; Petersson, G. A.; Nakatsuji, H.; Caricato, M.; Li, X.; Hratchian, H. P.; Izmaylov, A. F.; Bloino, J.; Zheng, G.; Sonnenberg, J. L.; Hada, M.; Ehara, M.; Toyota, K.; Fukuda, R.; Hasegawa, J.; Ishida, M.; Nakajima, T.; Honda, Y.; Kitao, O.; Nakai, H.; Vreven, T.; Montgomery, J. A.; Peralta, J. E.; Ogliaro, F.; Bearpark, M.; Heyd, J. J.; Brothers, E.; Kudin, K. N.; Staroverov, V. N.; Kobayashi, R.; Normand, J.; Raghavachari, K.; Rendell, A.; Burant, J. C.; Iyengar, S. S.; Tomasi, J.; Cossi, M.; Rega, N.; Millam, J. M.; Klene, M.; Knox, J. E.; Cross, J. B.; Bakken, V.; Adamo, C.; Jaramillo, J.; Gomperts, R.; Stratmann, R. E.; Yazyev, O.; Austin, A. J.; Cammi, R.; Pomelli, C.; Ochterski, J. W.; Martin, R. L.; Morokuma, K.; Zakrzewski, V. G.; Voth, G. A.; Salvador, P.; Dannenberg, J. J.; Dapprich, S.; Daniels, A. D.; Farkas; Foresman, J. B.; Ortiz, J. V.; Cioslowski, J.; Fox, D. J. Gaussian 09, Revision B.01 Wallingford CT, 2009.
- (36) Becke, A. D. Density-Functional Thermochemistry.3. The Role of Exact Exchange. *J. Chem. Phys.* **1993**, *98*, 5648.
- (37) Reed, A. E.; Curtiss, L. A.; Weinhold, F. Intermolecular Interactions from a Natural Bond Orbital, Donor-Acceptor Viewpoint. *Chem. Rev.* **1988**, *88*, 899.
- (38) Becke, A. D.; Edgecombe, K. E. A Simple Measure of Electron Localization in Atomic and Molecular-Systems. *J. Chem. Phys.* **1990**, *92*, 5397.
- (39) Silvi, B.; Savin, A. Classification of Chemical-Bonds Based on Topological Analysis of Electron Localization Functions. *Nature* **1994**, *371*, 683.
- (40) Hasegawa, M.; Nishidate, K. Semiempirical Approach to the Energetics of Interlayer Binding in Graphite. *Phys. Rev. B* **2004**, *70*, 7.

- (41) Tournus, F.; Latil, S.; Heggie, M. I.; Charlier, J. C. Pi-Stacking Interaction between Carbon Nanotubes and Organic Molecules. *Phys. Rev. B* **2005**, *72*, 5.
- (42) Durgun, E.; Dag, S.; Ciraci, S.; Gulseren, O. Energetics and Electronic Structures of Individual Atoms Adsorbed on Carbon Nanotubes. *J. Phys. Chem. B* **2004**, *108*, 575.
- (43) Coriani, S.; Haaland, A.; Helgaker, T.; Jorgensen, P. The Equilibrium Structure of Ferrocene. *ChemPhysChem* **2006**, *7*, 245.
- (44) Swart, M. Metal-ligand Bonding in Metallocenes: Differentiation between Spin State, Electrostatic and Covalent Bonding. *Inorg. Chim. Acta* **2007**, *360*, 179.
- (45) Youn, I. S.; Kim, D. Y.; Singh, N. J.; Park, S. W.; Youn, J.; Kim, K. S. Intercalation of Transition Metals into Stacked Benzene Rings: A Model Study of the Intercalation of Transition Metals into Bilayered Graphene. *J. Chem. Theory Comput.* **2012**, *8*, 99.
- (46) An, W.; Wu, X. J.; Yang, J. L.; Zeng, X. C. Adsorption and Surface Reactivity on Single-Walled Boron Nitride Nanotubes Containing Stone-Wales Defects. *J. Phys. Chem. C* **2007**, *111*, 14105.
- (47) Chen, Z. F.; Thiel, W.; Hirsch, A. Reactivity of the Convex and Concave Surfaces of Single-Walled Carbon Nanotubes (Swcnts) towards Addition Reactions: Dependence on the Carbon-Atom Pyramidalization. *ChemPhysChem* **2003**, *4*, 93.
- (48) Hu, L. B.; Hu, X. R.; Wu, X. B.; Du, C. L.; Dai, Y. C.; Deng, J. B. Density Functional Calculation of Transition Metal Adatom Adsorption on Graphene. *Physica B* **2010**, *405*, 3337.
- (49) Groves, M. N.; Malardier-Jugroot, C.; Jugroot, M. Improving Platinum Catalyst Durability with a Doped Graphene Support. *J. Phys. Chem. C* **2012**, *116*, 10548.
- (50) Yang, L. J.; Jiang, S. J.; Zhao, Y.; Zhu, L.; Chen, S.; Wang, X. Z.; Wu, Q.; Ma, J.; Ma, Y. W.; Hu, Z. Boron-Doped Carbon Nanotubes as Metal-Free Electrocatalysts for the Oxygen Reduction Reaction. *Angew. Chem., Int. Ed.* **2011**, *50*, 7132.

**Table 2.1.** Calculated minimum binding distance between the CpTM ligand and the substrate.\*

Structure	Binding Distance (Å)									
	Fe-B	Fe-C	Co-B	Co-C	Ni-B	Ni-C	Cr-B	Cr-C	Cu-B	Cu-C
CpTM/B-CNT(8,0)	1.98	1.78	2.05	1.89	2.10	2.00	2.12	1.94	2.14	2.03
CpTM/B-CNT(6,6)	2.19	1.94	2.24	1.98	2.27	1.99	2.16	1.92	2.21	2.02
CpTM/CNT(8,0)		2.03		1.98		1.97		2.11		2.02
CpTM/CNT(6,6)		2.12		2.17		1.93		2.15		2.04
CpTM/BC <sub>5</sub>	2.27	2.16								
CpTM/B-C	2.25	2.15								
CpTM/C <sub>70</sub>		2.18								

\* For reference, the Fe-C distance of ferrocene molecule (Cp<sub>2</sub>Fe) is 2.05 Å.<sup>41</sup>

**Table 2.2.** Calculated magnetic moment per supercell corresponding to several of the systems.\*

<i>Structure</i>	Magnetic Moment ( $\mu_B$ ) per Supercell				
	Fe	Co	Ni	Cr	Cu
CpTM/B-CNT(8,0)	0.07	0.00	0.00	1.25	0.00
CpTM/B-CNT(6,6)	0.93	0.20	0.87	1.10	0.62
CpTM/CNT(8,0)	0.97	0.00	1.08	1.27	0.00
CpTM/CNT(6,6)	0.00	1.53	0.74	1.55	0.00

\*For reference:  $\mu_B(\text{B-CNT}(8,0)) = 0.80$ ;  $\mu_B(\text{B-CNT}(6,6)) = 0.63$ ;  $\mu_B(\text{CNT}(8,0)) = 0.00$ ; and  $\mu_B(\text{CNT}(6,6)) = 0.00$ .

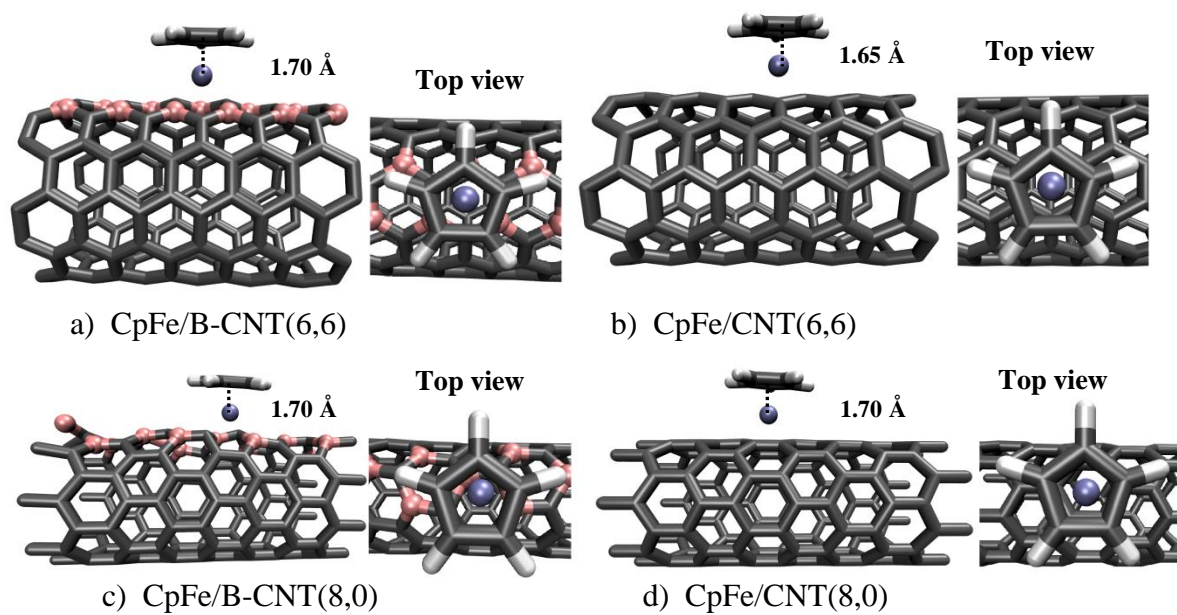


**Figure 2.1.** Optimized geometries of CpFe on CNT/B-CNT complexes. Selected distances are shown in units of angstroms, corresponding to the Fe to Cp ring center distance.

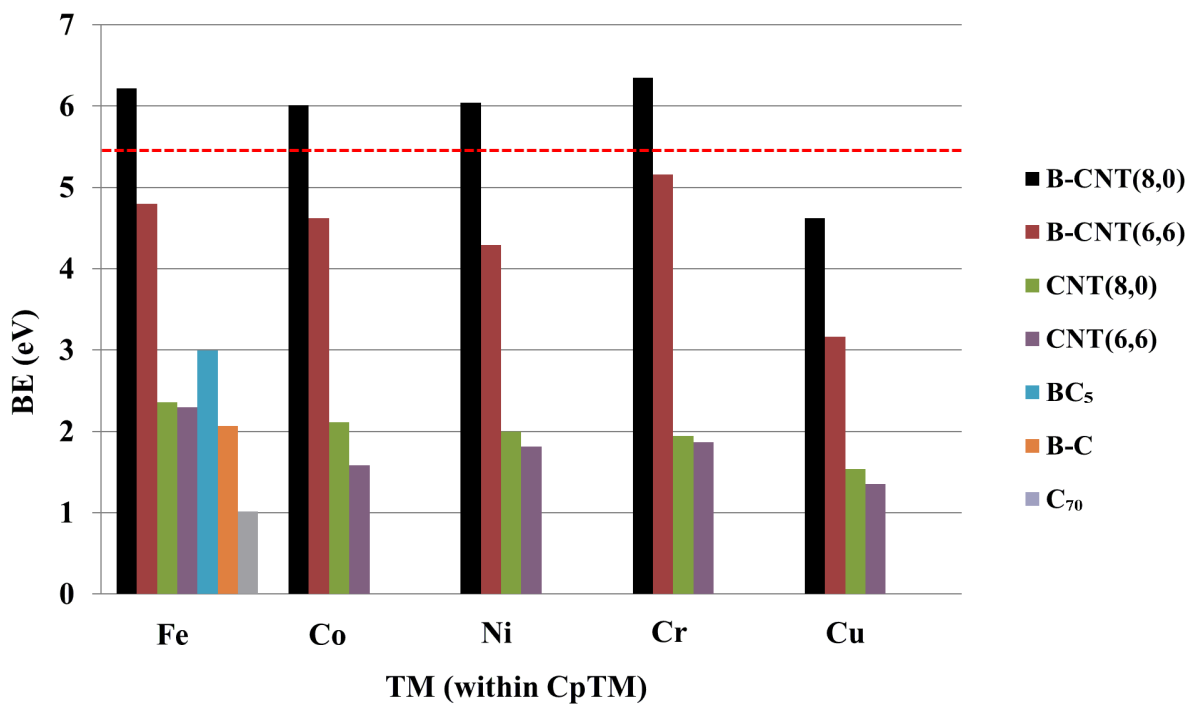


**Figure 2.2.** Binding energies of different CpTMs adsorbed on pristine/B-doped CNTs and graphenes. The red dashed line corresponds to the BE of Cp-TM within a ferrocene molecule.

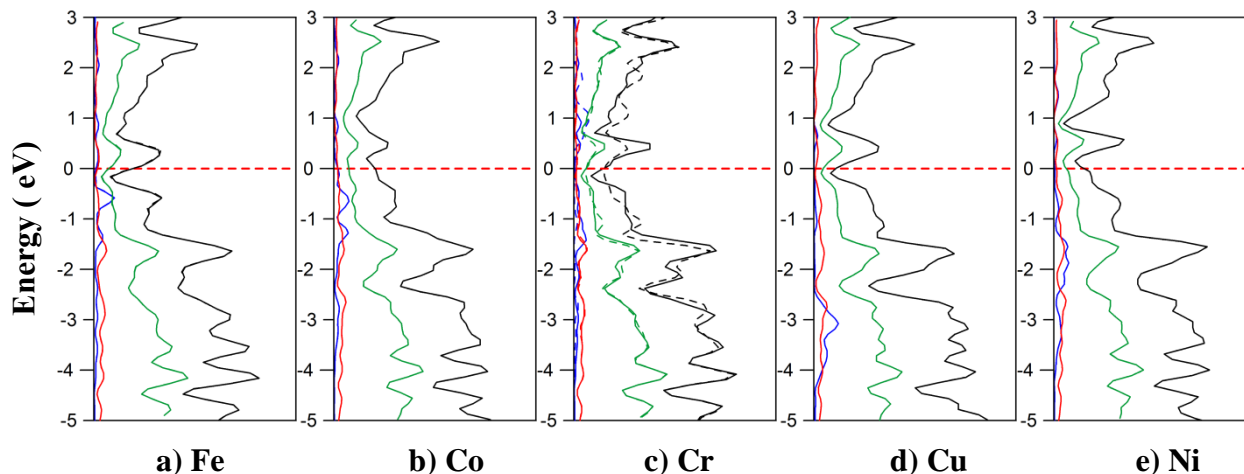


**Figure 2.3.** Calculated density of states (DOS) for CpTM/B-CNT (8,0) complexes. For the projected-DOS (PDOS), blue, green, and red curves represent projected TM-*d*, C-*p*, and B-*p* states, respectively. The Fermi level (dashed red line) is shifted to zero eV. For the total DOS, the spin-up and spin-down states are shown by solid and dashed black lines, respectively.

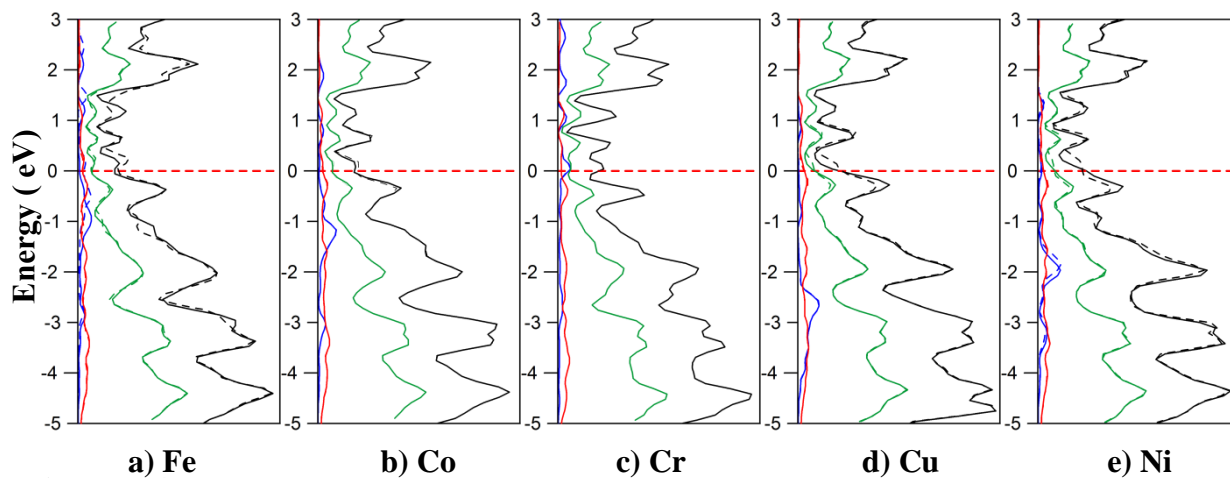


**Figure 2.4.** Calculated density of states (DOS) for CpTM/B-CNT (6,6) complexes. The line labels are consistent with those used in Figure 3.

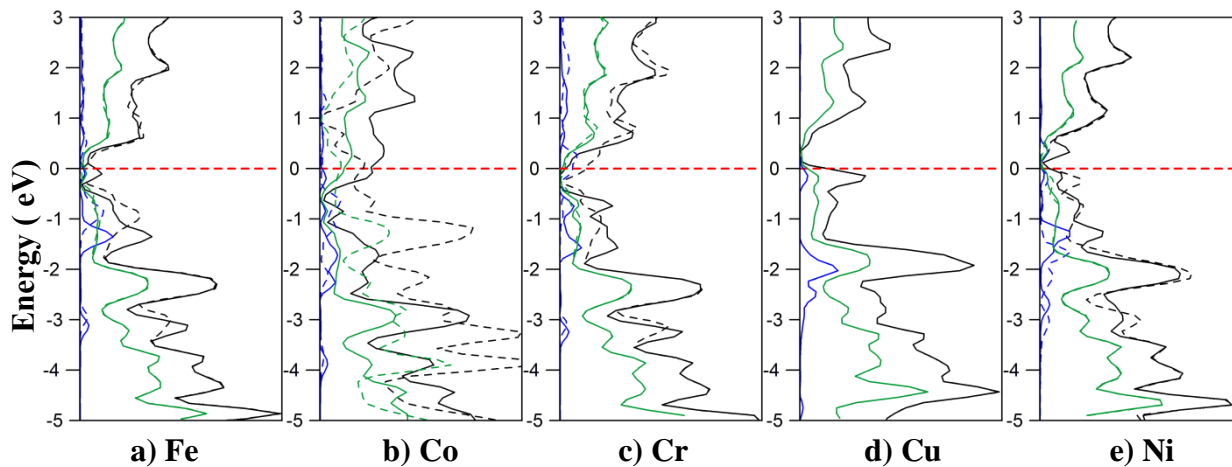


**Figure 2.5.** Calculated density of states (DOS) for CpTM/CNT (8,0) complexes. The line labels are consistent with those used in Figure 3.

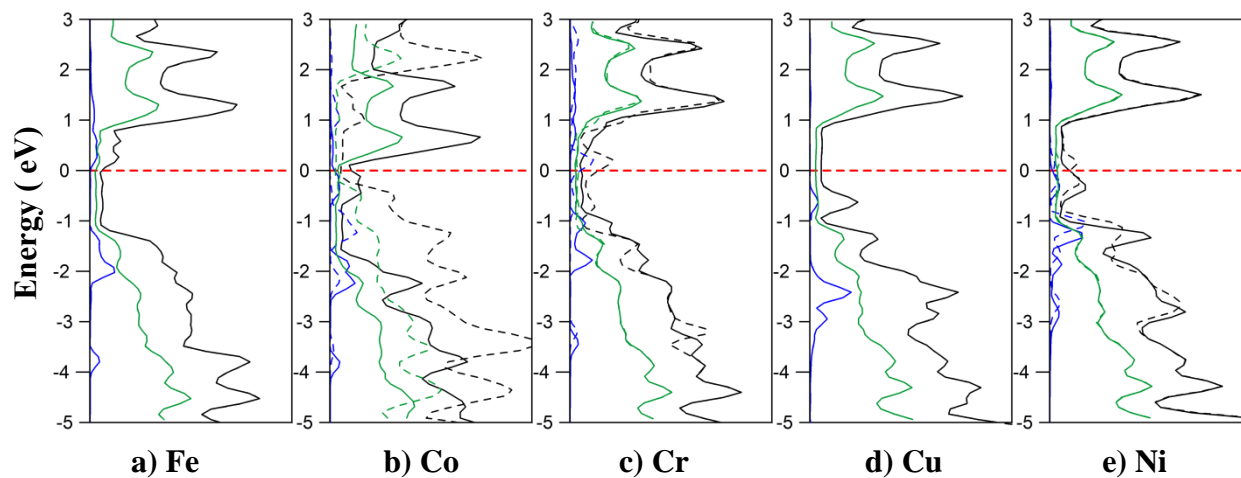


**Figure 2.6.** Calculated density of states (DOS) for CpTM/CNT (6,6) complexes. The line labels are consistent with those used in Figure 3.

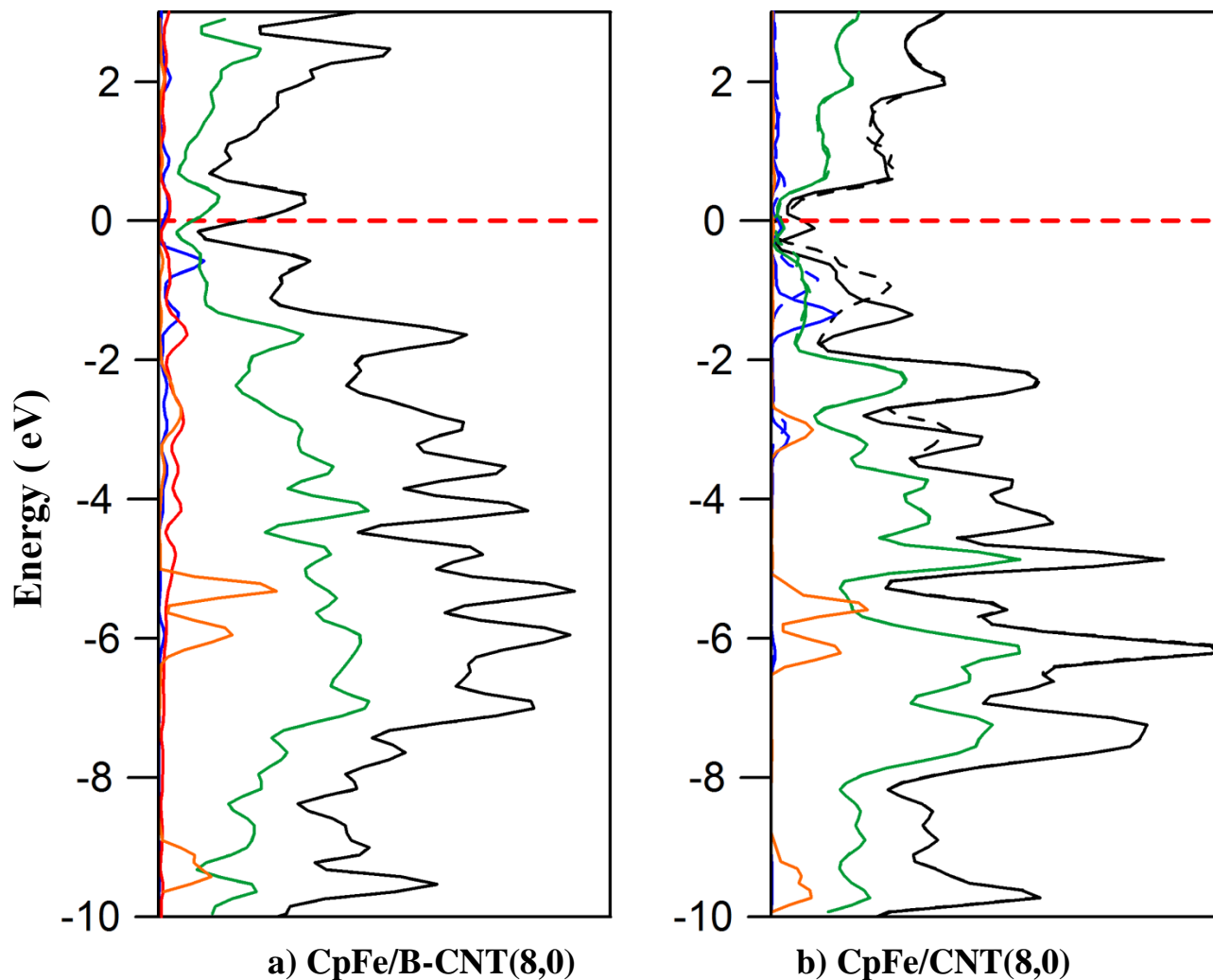


**Figure 2.7.** Calculated density of states (DOS) for CpFe/B-CNT (8,0) and CpFe/CNT (8,0) complexes. The line labels are consistent with those used in Figure 3, with the orange lines representing C-*p* states on the Cp ring.

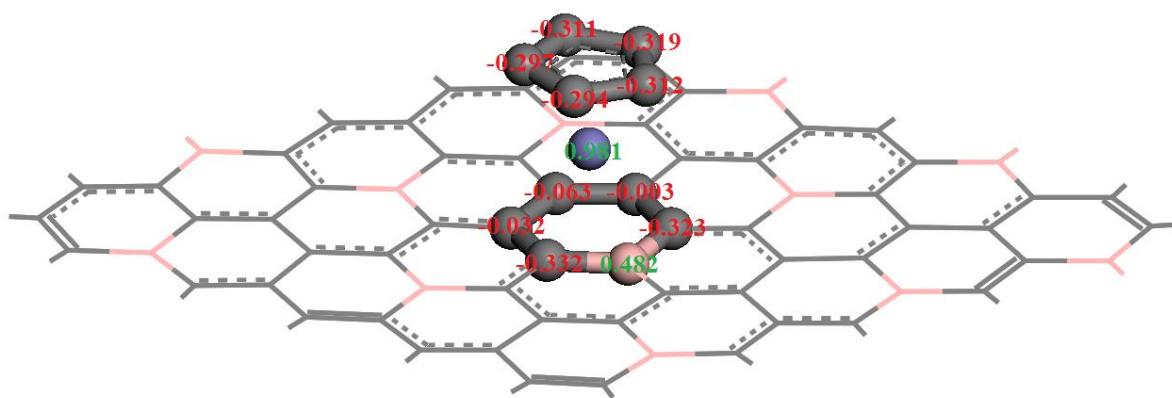


**Figure 2.8.** Optimized structures and NBO partial charges of CpFe/BC<sub>5</sub> graphene complexes (H atoms are omitted for clarity). The Fe to Cp ring center distance is 1.73 Å.

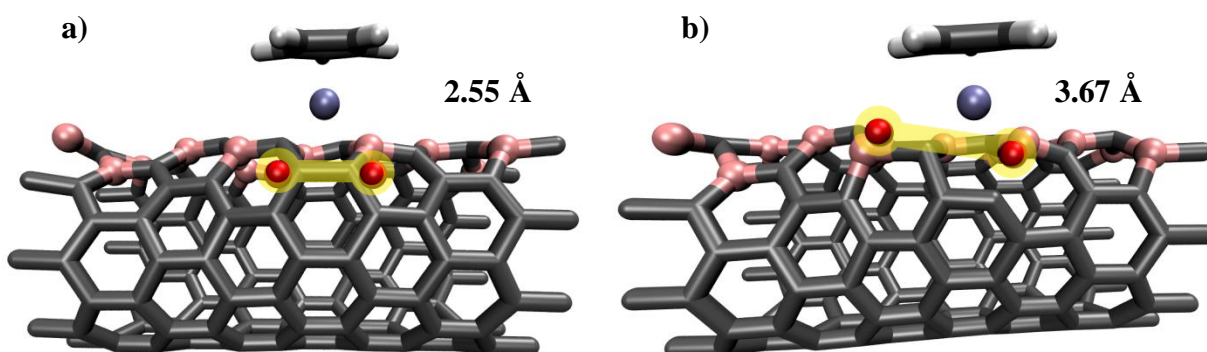


**Figure 2.9.** Optimized geometries of an O<sub>2</sub> molecule on a CpFe/B-CNT (8,0) complex: a) molecular chemisorption; and b) dissociative chemisorption. The O-O distances are shown in the figure, highlighted in yellow (for clarity).

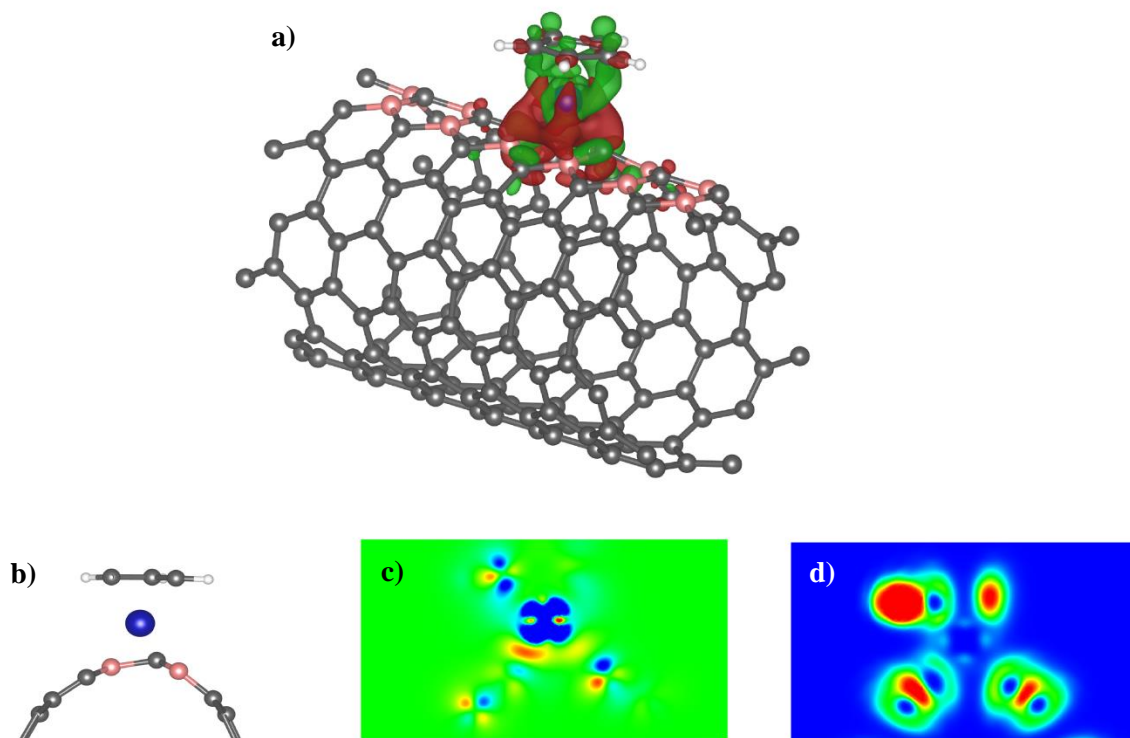


**Figure 2.10.** a) 3D-deformation charge density isosurface of CpFe/B-CNT (6,6) complex, where red and green denote positive and negative values, respectively. The isovalue is chosen to be  $0.03 e^-$ , b) cross-section of the system, c) cross-section of the deformation charge density across the iron atom and Cp ring. The red and blue colors represent values from  $-0.01e^-$  to  $0.01e^-$ , respectively, d) ELF cross-section of the CpFe/B-CNT (6,0) complex. The value of ELF ranges from 0 to 0.8, colored blue to red, respectively.

Appendix A. Supporting Information for Chapter 2.

**Table A1.** Binding energies of different CpTMs adsorbed on pristine/B-doped CNTs and graphenes.

<i>Structure</i>	TM and Binding Energy (eV)				
	Fe	Co	Ni	Cr	Cu
CpTM/B-CNT(8,0)	6.22	6.01	6.04	6.35	4.62
CpTM/B-CNT(6,6)	4.80	4.62	4.29	5.16	3.16
CpTM/CNT(8,0)	2.36	2.11	2.00	1.94	1.54
CpTM/CNT(6,6)	2.30	1.58	1.81	1.87	1.35
CpTM/BC <sub>5</sub>	3.00				
CpTM/B-C	2.07				
CpTM/C <sub>70</sub>	1.01				

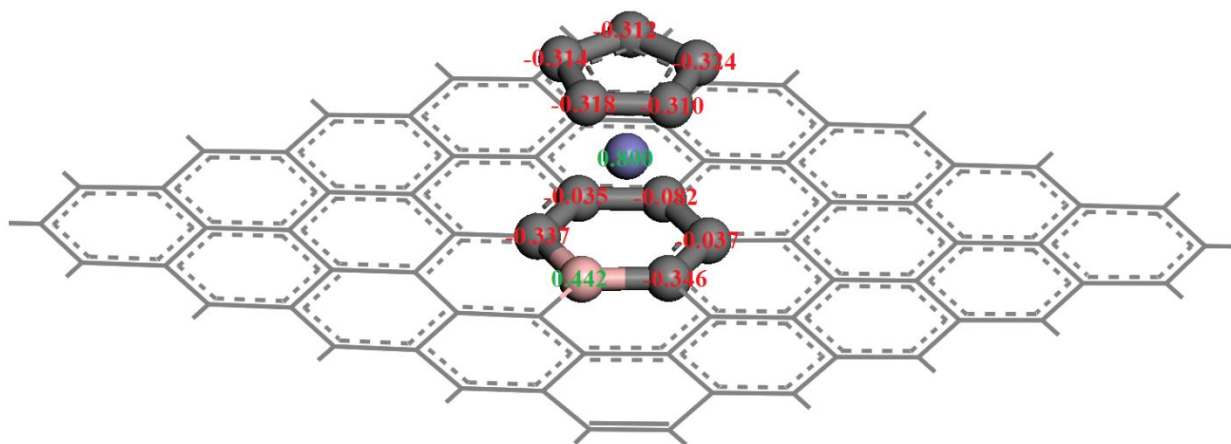


**Figure A1.** Optimized structures and NBO partial charges of CpFe/B-C graphene complexes (H atoms are omitted for clarity). The Fe to Cp ring center distance is 1.69 Å.

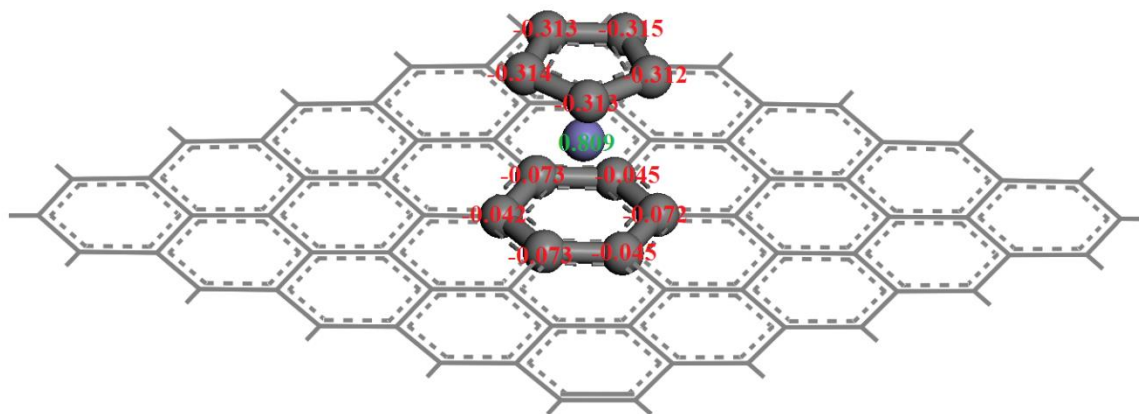


**Figure A2.** Optimized structures and NBO partial charges of CpFe/C<sub>70</sub> graphene complexes (H atoms are omitted for clarity). The Fe to Cp ring center distance is 1.66 Å.

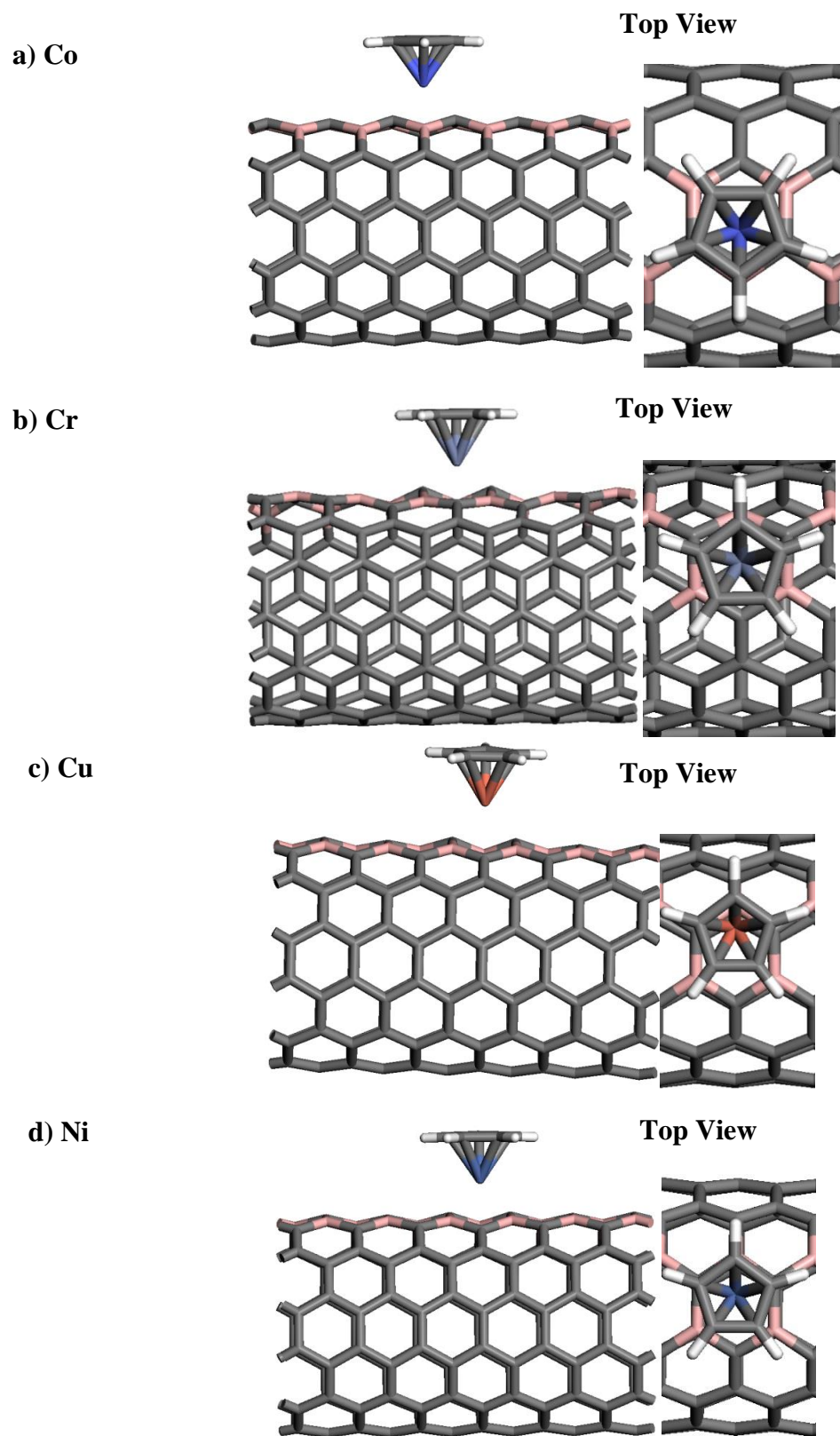


**Figure A3.** Optimized structures of CpTM/B-CNT (6,6) complexes.

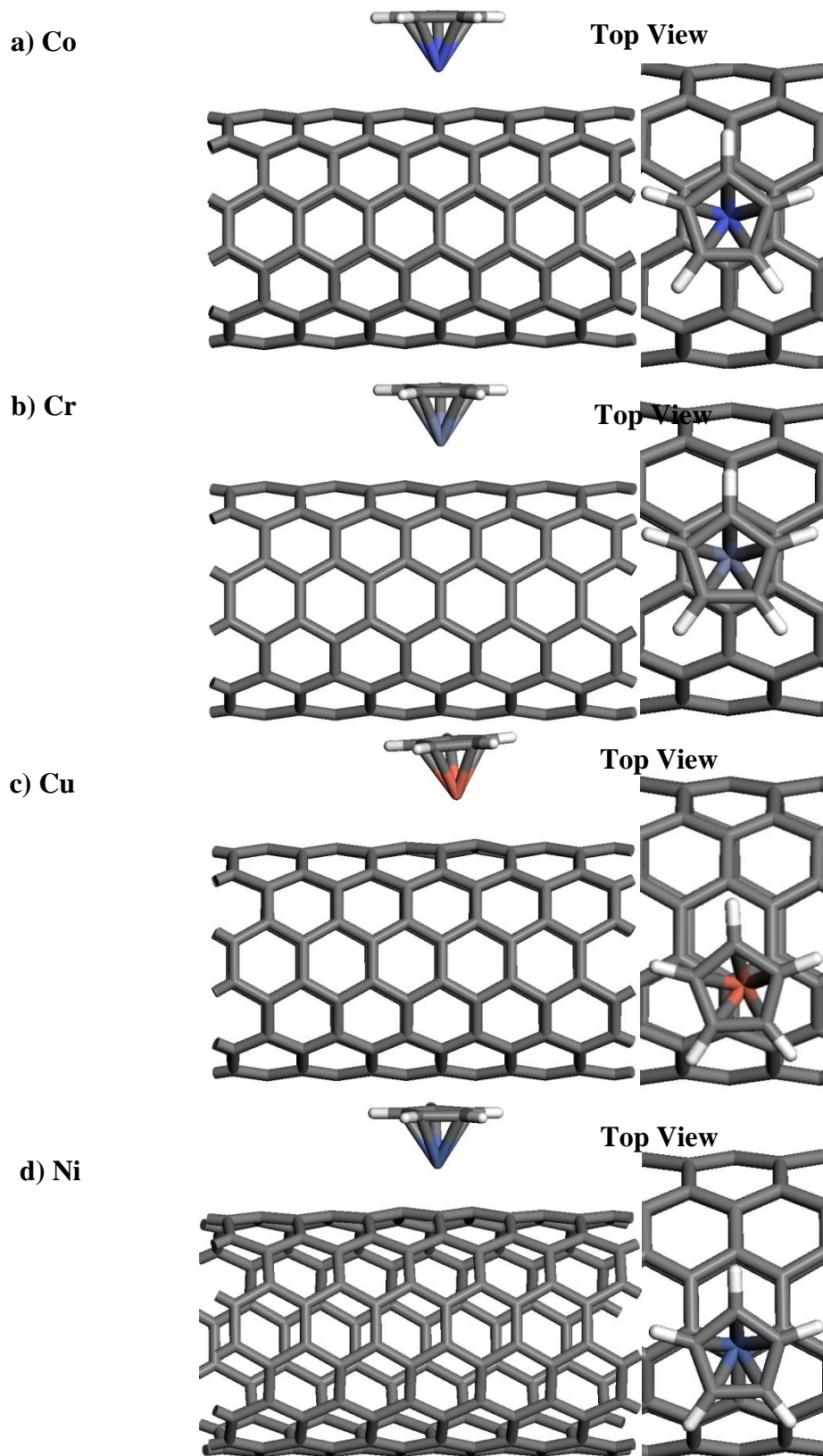


**Figure A4.** Optimized structures of CpTM/CNT (6,6) complexes.

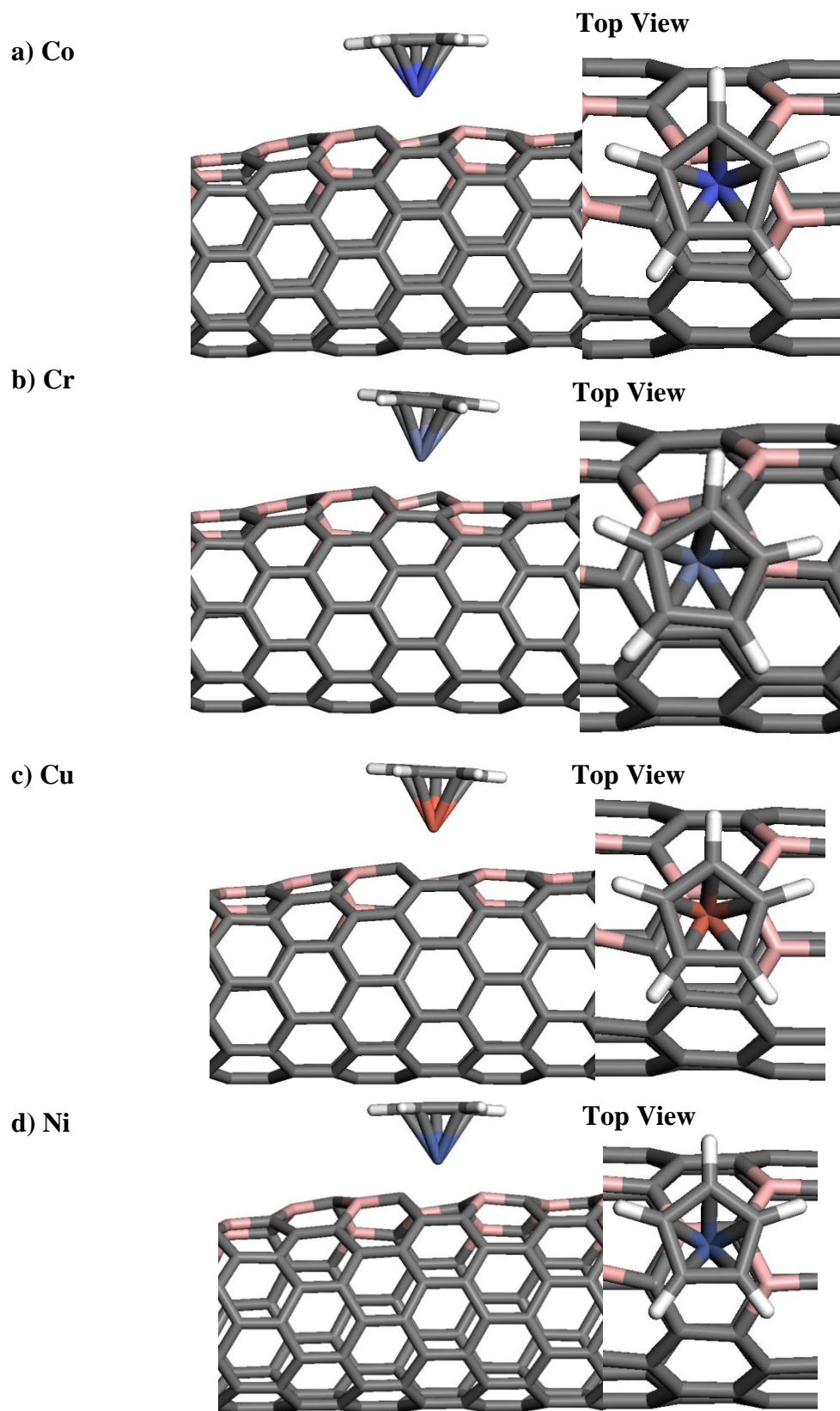


**Figure A5.** Optimized structures of CpTM/B-CNT (8,0) complexes.

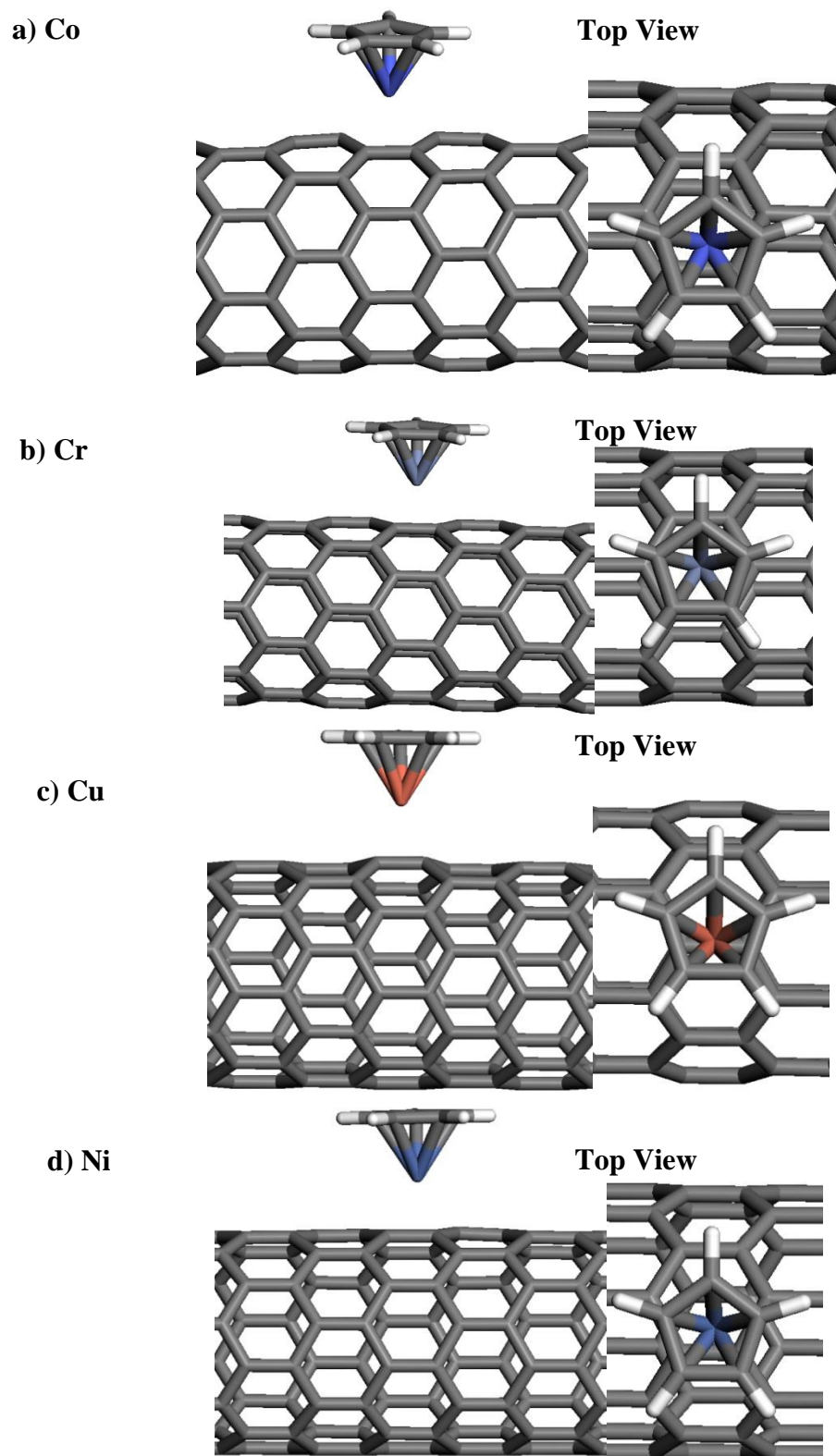


**Figure A6.** Optimized structures of CpTM/CNT (8,0) complexes.

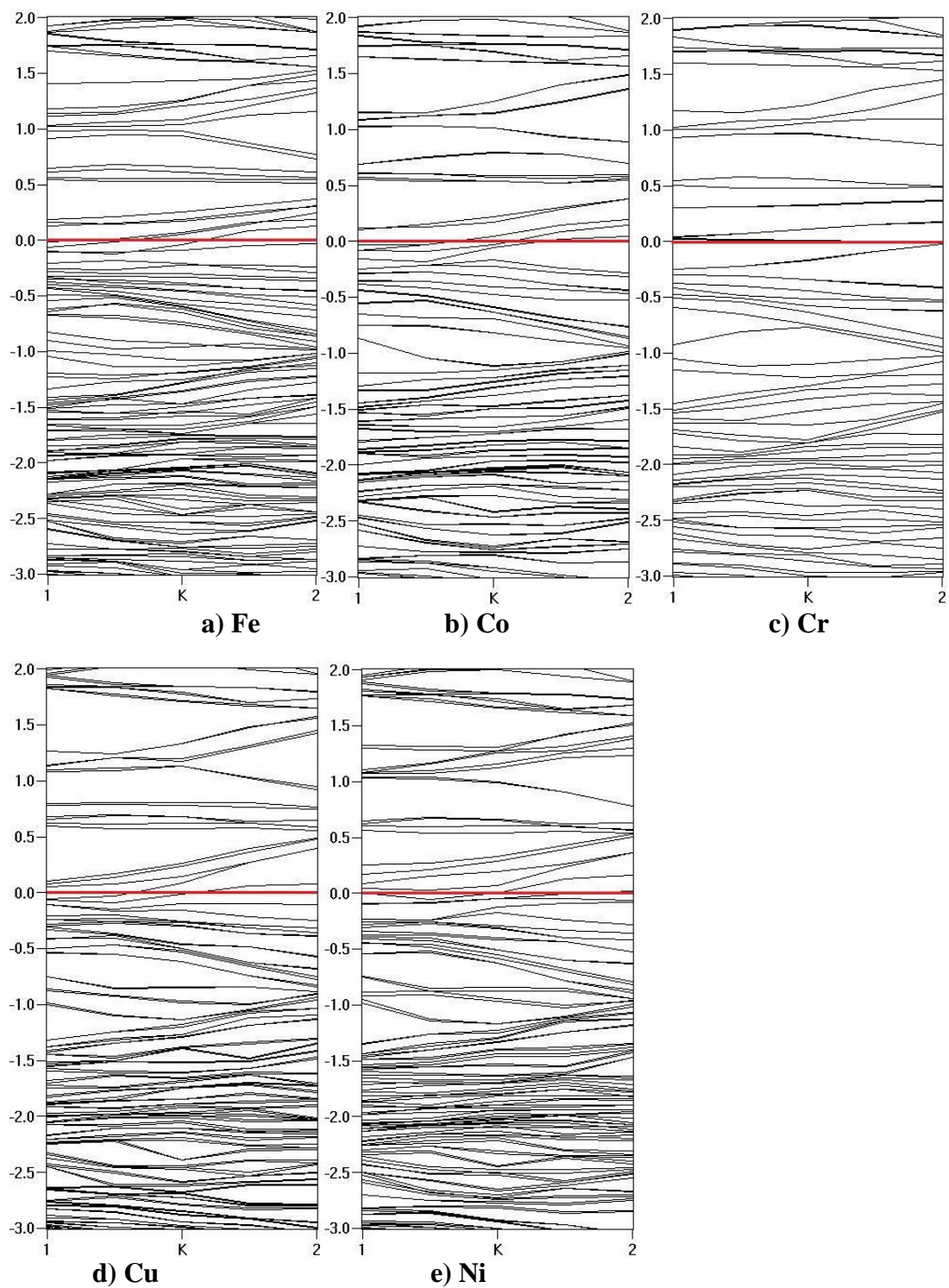


**Figure A7.** Calculated band structures of CpTM/B-CNT (6,6) complexes. The Fermi level (red line) is shifted to 0 eV.

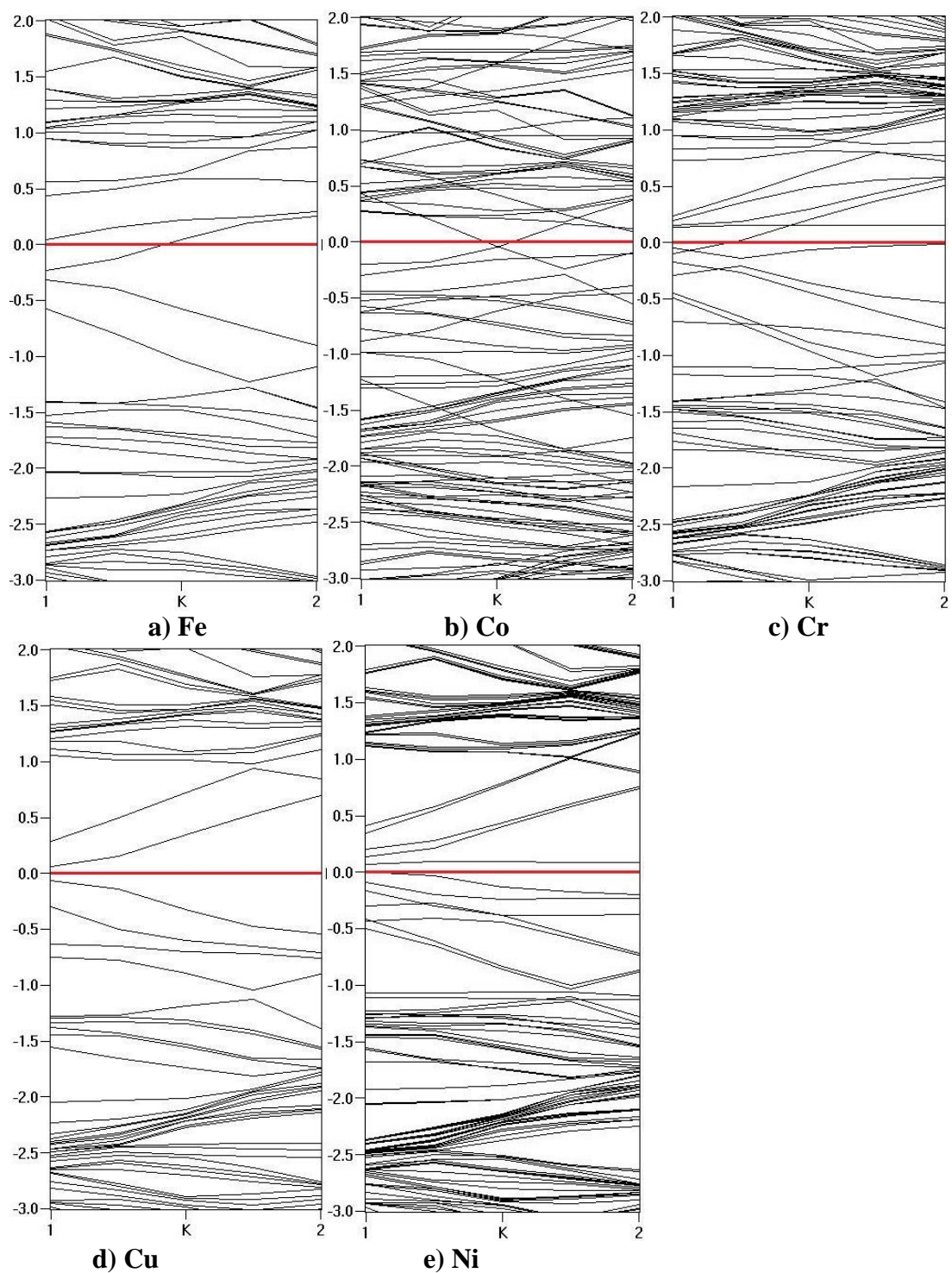


**Figure A8.** Calculated band structures of CpTM/CNT (6,6) complexes. The Fermi level (red line) is shifted to 0 eV.

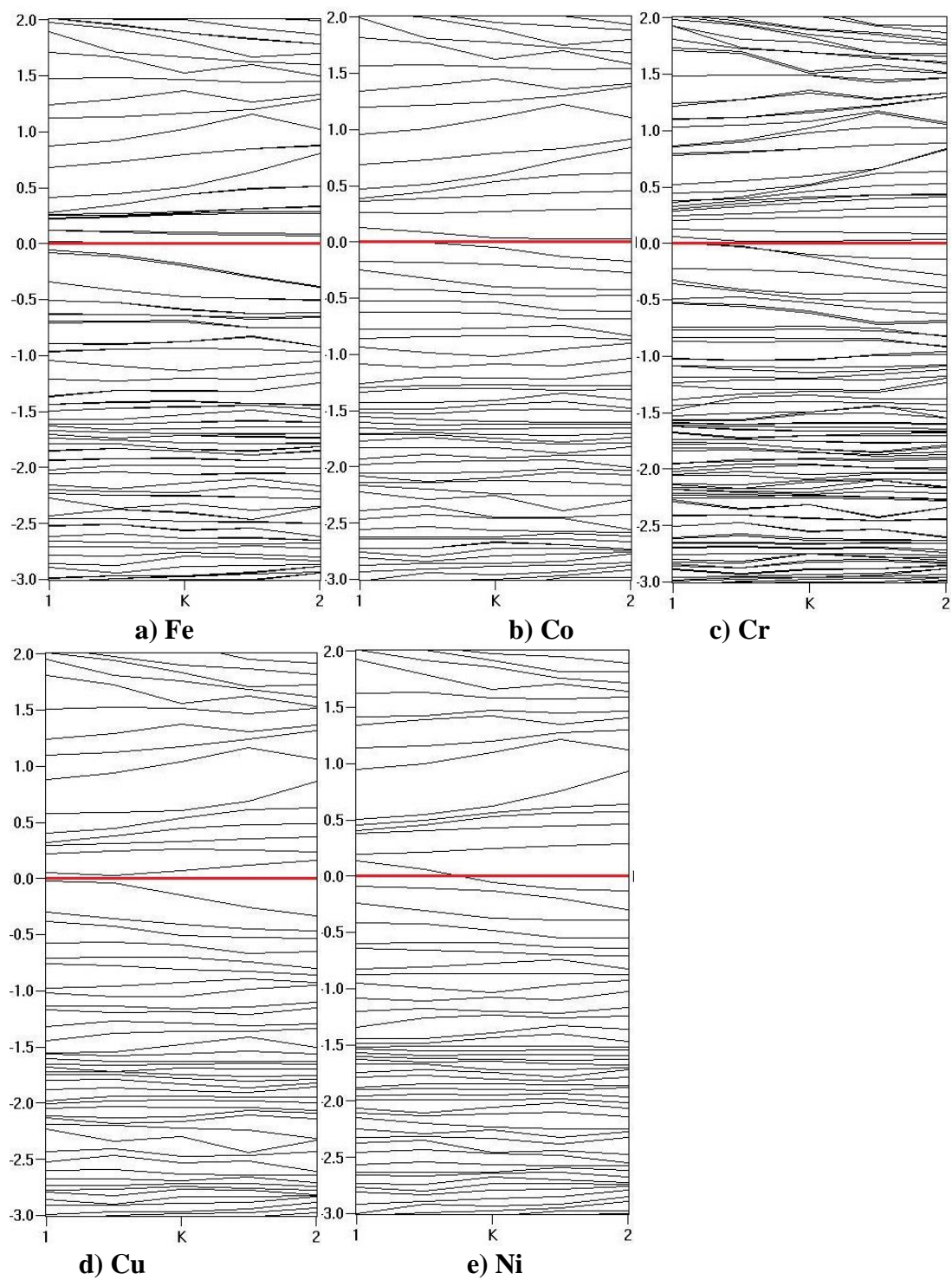


**Figure A9.** Calculated band structures of CpTM/B-CNT (8,0) complexes. The Fermi level (red line) is shifted to 0 eV.

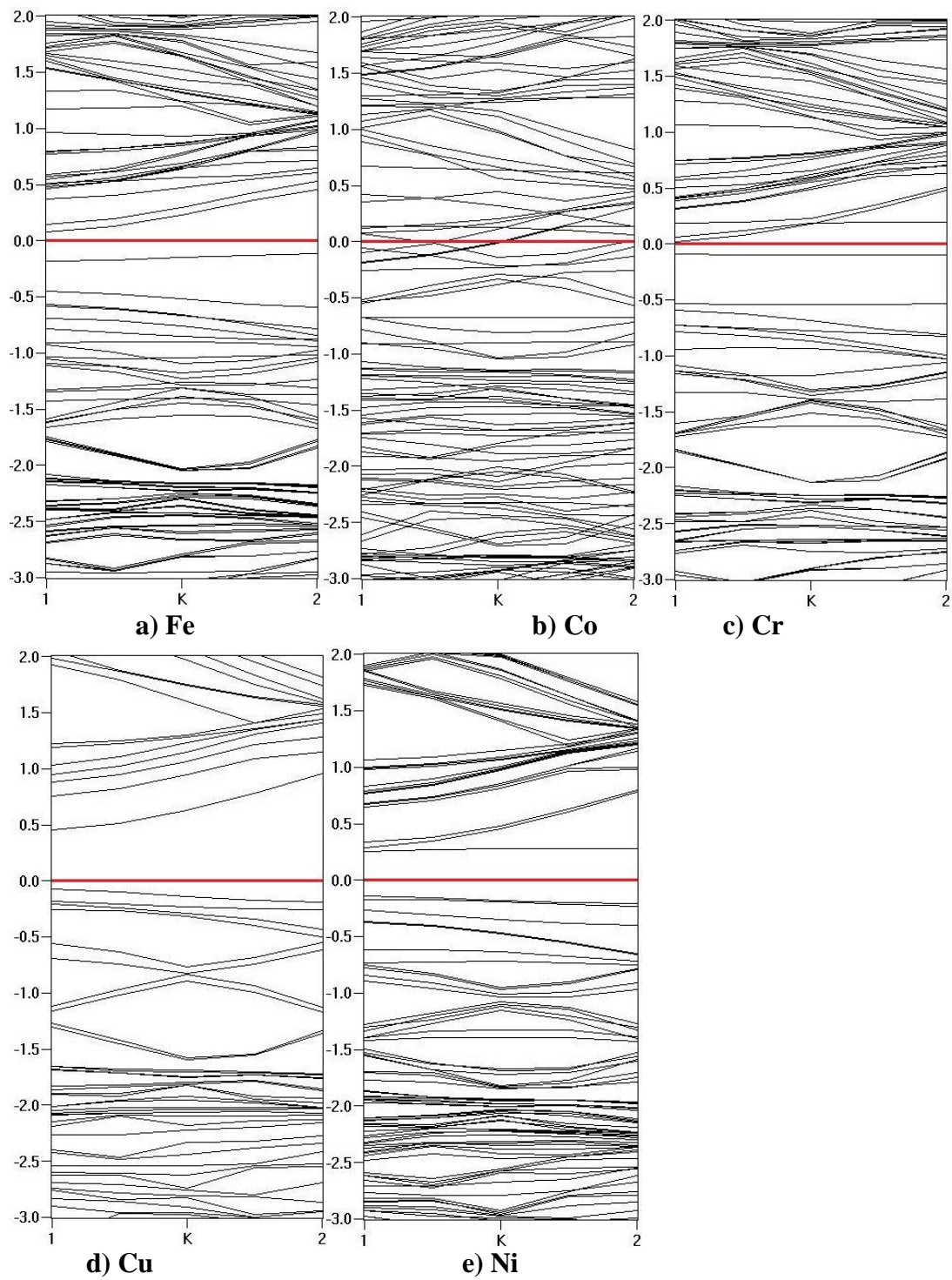
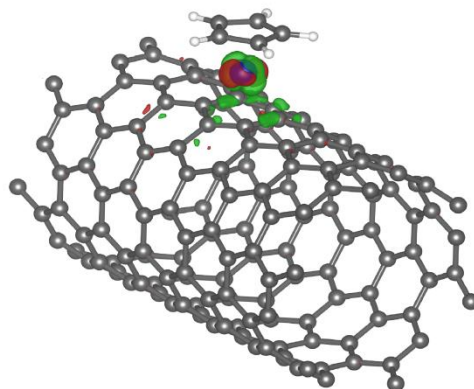
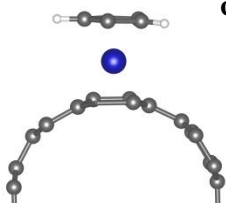


**Figure A10.** Calculated band structures of CpTM/CNT (8,0) complexes. The Fermi level (red line) is shifted to 0 eV.

a)



b)



c)

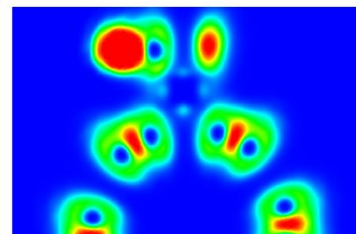
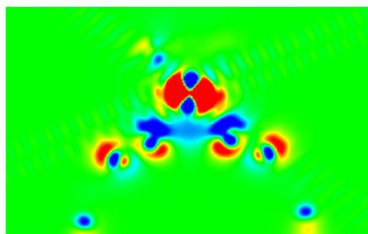


**Figure A11.** a) 3D-deformation charge density isosurface of CpFe/CNT (6,6) complex, where red and green denote positive and negative values, respectively. The isovalue is chosen to be  $0.03 e^-$ , b) cross-section of the system, c) cross-section of the deformation charge density across the iron atom and Cp ring. The red and blue colors represent values from  $-0.01e^-$  to  $0.01e^-$ , respectively, d) ELF cross-section of the CpFe/CNT (6,0) complex. The value of ELF ranges from 0 to 0.8, colored blue to red, respectively.

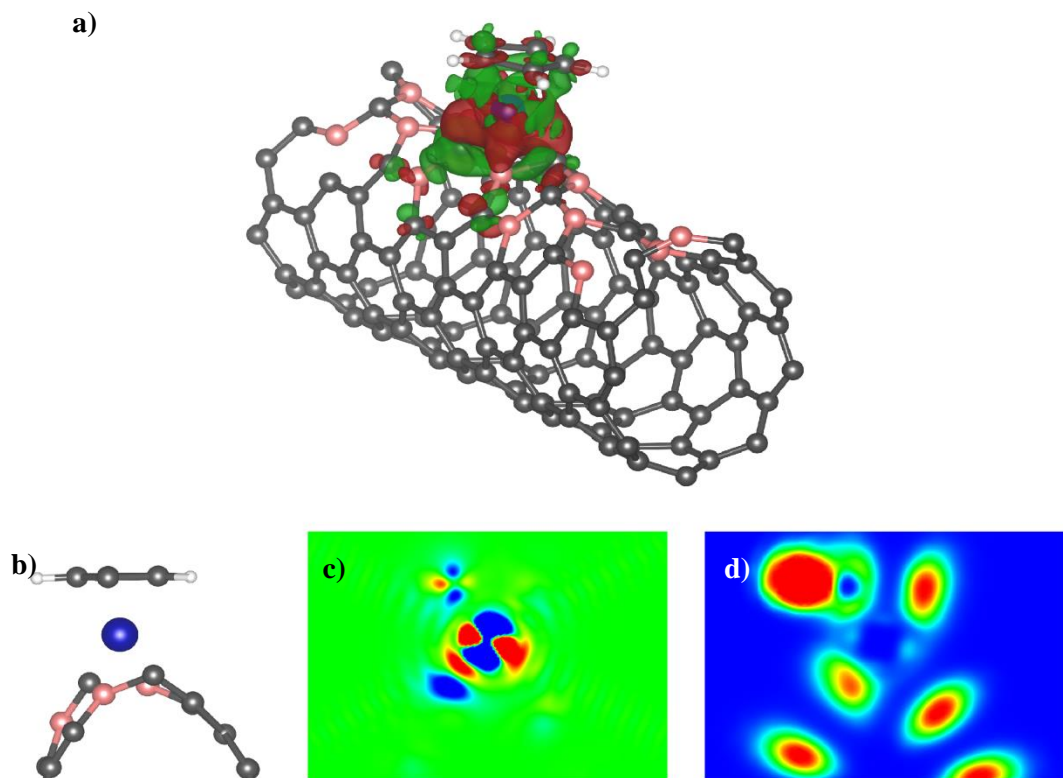


**Figure A12.** a) 3D-deformation charge density isosurface of CpFe/B-CNT (8,0) complex, b) cross section of the system, c) cross section of the deformation charge density across the iron atom and Cp ring and d) ELF cross section of the CpFe/B-CNT (8,0) complex. The isovalues and coloring schemes were the same as in Figure A11.

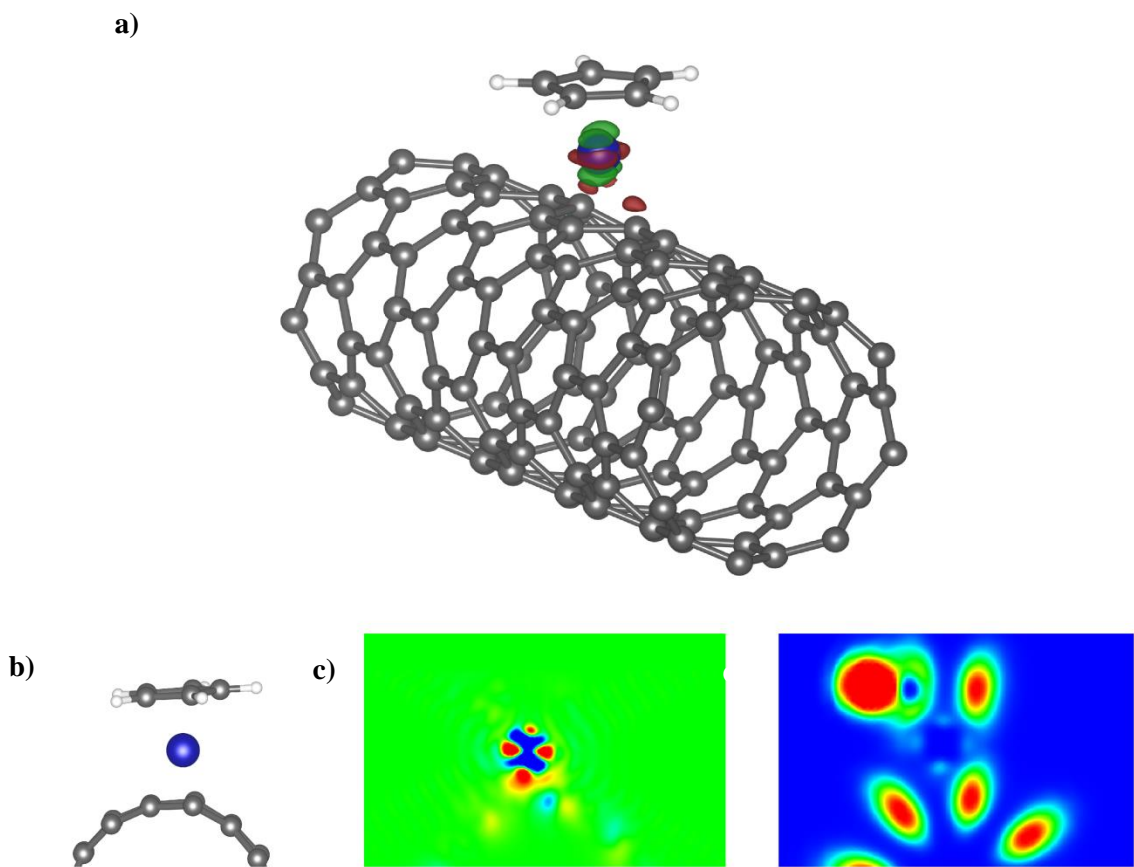


**Figure A13.** a) 3D-deformation charge density isosurface of CpFe/CNT (8,0) complex, b) cross section of the system, c) cross section of the deformation charge density across the iron atom and Cp ring and d) ELF cross section of the CpFe/B-CNT (8,0) complex. The isovalues were chosen to be  $0.03 e^-$  and coloring range of b) were  $-0.02$  to  $0.02 e^-$ , ELF were plotted as same isovalues as in Figure A11.

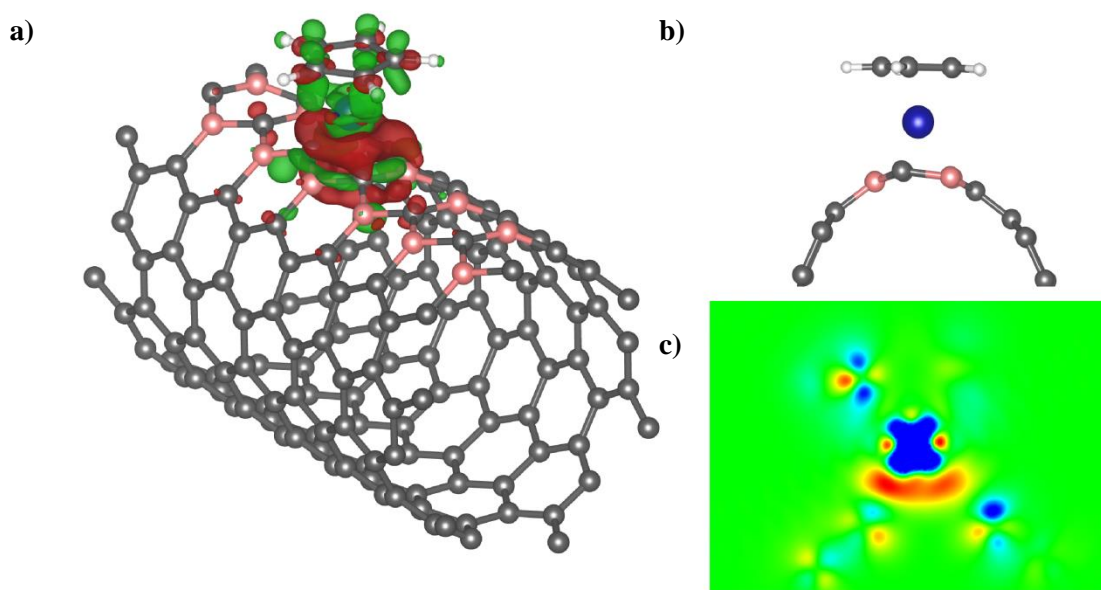


**Figure A14.** a) 3D-deformation charge density isosurface of CpCo/B-CNT (6,6) complex, b) cross section of the system, c) cross section of the deformation charge density across the cobalt atom and Cp ring and the isovalues and coloring schemes were the same as in Figure A11.

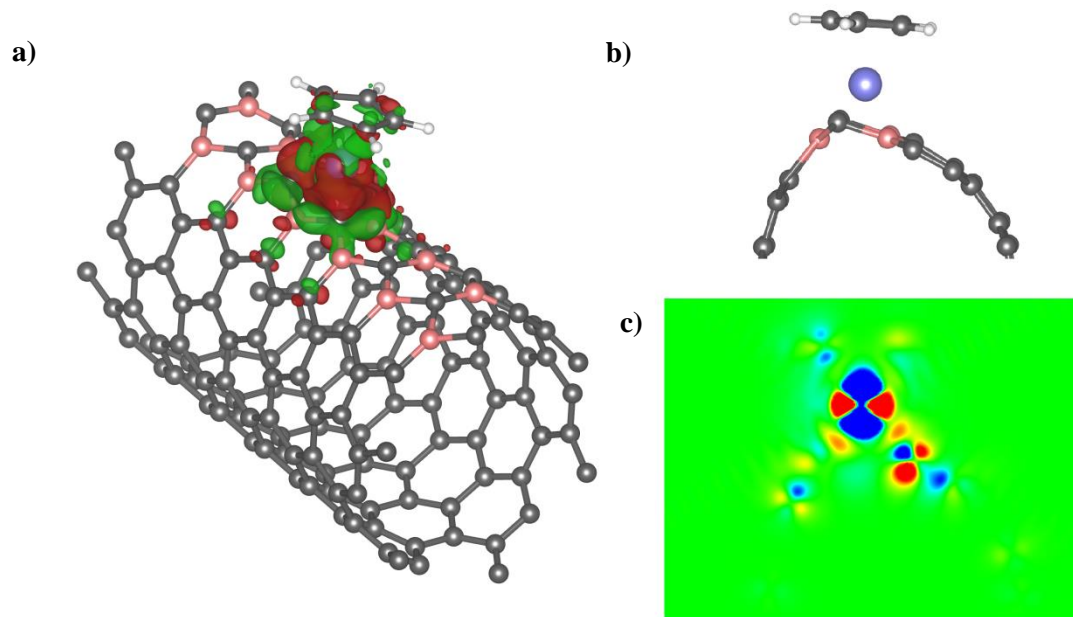


**Figure A15.** a) 3D-deformation charge density isosurface of CpCr/B-CNT (6,6) complex, b) cross section of the system, c) cross section of the deformation charge density across the chromium atom and Cp ring. The isovalues and coloring schemes were the same as in Figure A11.

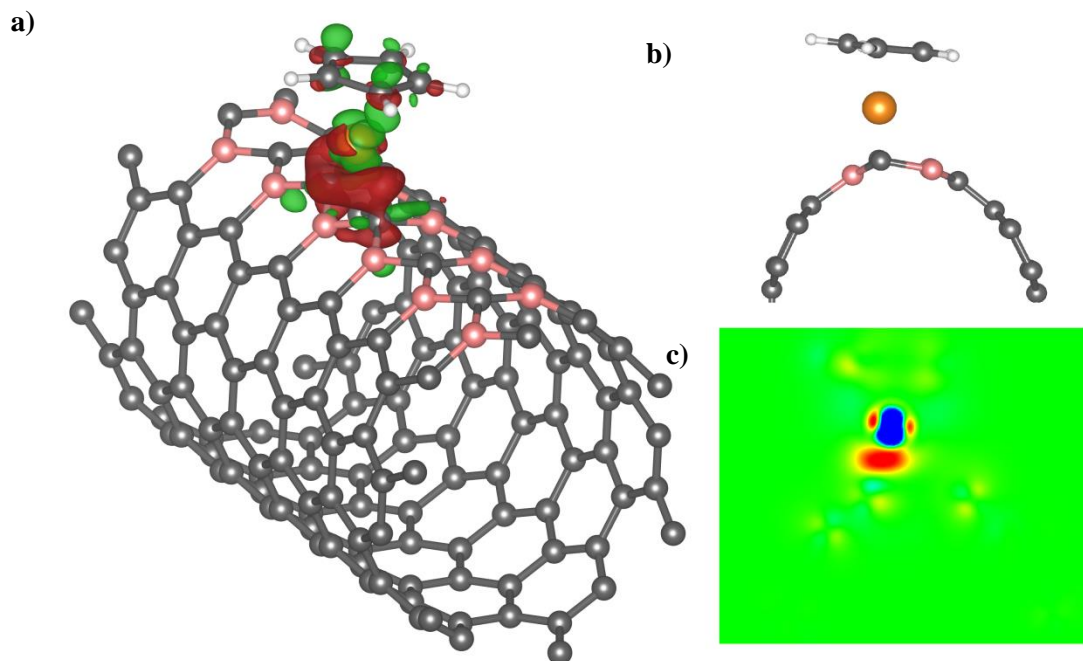


**Figure A16.** a) 3D-deformation charge density isosurface of CpCu/B-CNT (6,6) complex, b) cross section of the system, c) cross section of the deformation charge density across the copper atom and Cp ring. The isovalues and coloring schemes were the same as in Figure A11.

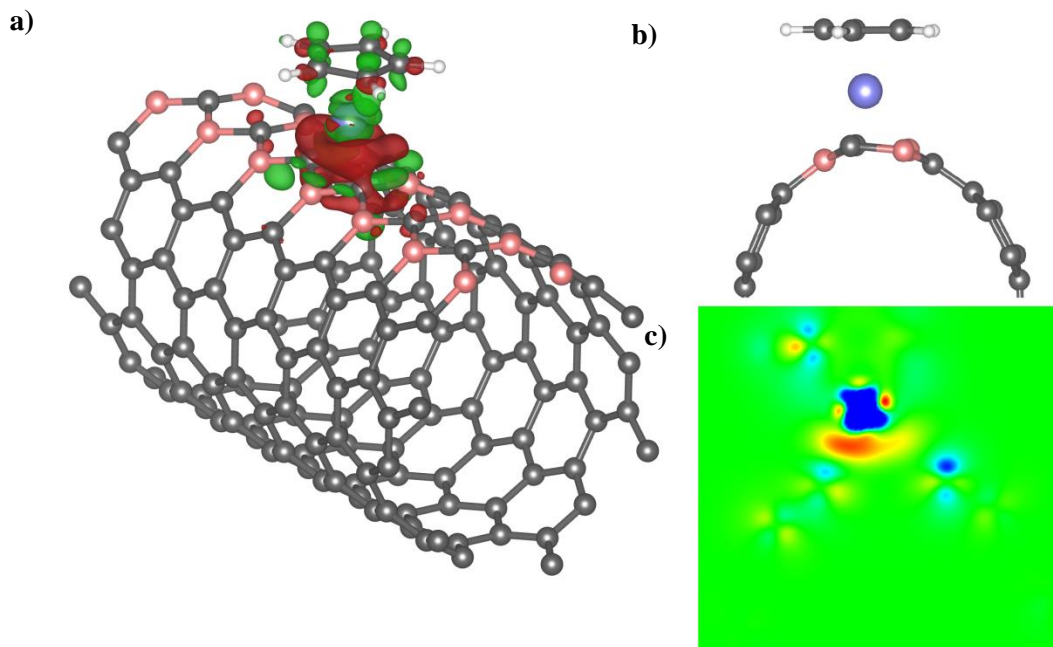


**Figure A17.** a) 3D-deformation charge density isosurface of CpNi/B-CNT (6,6) complex, b) cross section of the system, c) cross section of the deformation charge density across the nickel atom and Cp ring. The isovalues and coloring schemes were the same as in Figure A11.

## CHAPTER 3

### REDOX PROPERTIES OF GRAPHENES FUNCTIONALIZED WITH CYCLOPENTADIENE–TRANSITION METAL COMPLEXES: A POTENTIAL REDOX- ACTIVE MATERIAL\*

#### 3.1 Introduction

Ferrocene ( $\text{Cp}_2\text{Fe}$ , where Cp = cyclopentadienyl) and other metallocene-based compounds ( $\text{Cp}_2\text{TM}$ , where TM = transition metal) have been widely used in catalysis, solar energy generation, hydrogen storage, cancer therapy, and nano-magnetism.<sup>1-3</sup> Among the structural, electronic and catalytic properties of metallocenes and their derivatives, they can serve as excellent electron donor-receptors in many electrochemical systems. For instance, ferrocene can act as a rapid and stable electron transfer mediator between glucose oxidase (GOD) and a graphitic electrode, which leads to a fast and accurate measurement of blood glucose level.<sup>4</sup> Other ferrocene-mediated enzyme electrodes also play important roles in electrochemical sensors for glucose, glycolate, amino-acid, and other bio-molecules.<sup>4, 5</sup> Moreover, redox-active organic monolayers can be used as potential materials for dynamic random access memory (DRAM) memories due to the nature of the charge storage/release mechanism inherent to the redox reactions.<sup>6-9</sup>

A critical challenge of the metallocene-based redox systems is the stabilization of the redox-active centers on the electrode, also called “redox-smart” material design. Most of these

---

\* Reprinted with permission from Journal of Physical Chemistry C, doi: 10.1021/jp508279n. Copyright 2014 American Chemical Society.

previous studies have focused on stabilizing the redox-active centers (such as ferrocene or porphyrins) on hydrogen-terminated silicon using complex sidechains,<sup>10-15</sup> or ferrocene-containing “pendant” sidechain-based polymers.<sup>16-18</sup> For instance Grelaud et al. recently reported the attachment of a dinuclear ferrocenyl/ruthenium(II) alkynyl redox-active side chain onto hydrogen-terminated silicon.<sup>19</sup> However, most of these synthesis efforts involve multistep synthesis processes of the complex side chains and some high-value (noble metal) materials to improve the resulting conductivity and stability.

In contrast to the current experimental approaches to attach metallocenes on supports, our previous simulation study identified an extraordinarily strong direct immobilization of cyclopentadienyl-transition metal complexes (CpTM) onto B-doped nanocarbons (including carbon nanotubes (CNTs) and graphene supports).<sup>20</sup> In addition to the CpTM redox-active centers, the B-doped nanocarbon supports have good conductivity and stability as a support material in electrochemical applications. For example, B-doped electrodes have been shown to exhibit better sintering, corrosion, and poisoning tolerance in fuel cell applications.<sup>21-23</sup> Moreover, B-CNT coated electrodes (in combination with glucose oxidase) were found to have better sensitivity, selectivity, and stability for electrochemical glucose sensing, as compared to a glassy carbon or a pristine CNT electrode.<sup>24</sup> Considering the similarity of the CpFe complex and the ferrocene molecule, CpFe/B-nanocarbon complexes are interesting candidates for integrated redox-active materials. However, it is critical for the CpFe centers to retain their ferrocene-like redox activity after being attached to the B-doped nanocarbon supports.

There are several related studies indicating that these hybrid materials could provide the following benefits:

(a) Good stability, as the binding energy of CpFe on B-doped CNT(8,0) is predicted to even surpassed the isolated Fe atom or H-F bond energy,<sup>20</sup>

(b) Good conductivity and corrosion resistance, which are inherit properties of B-doped nanocarbons;

(c) Economy, compared with immobilizing complex synthesized ferrocenyl sidechains on silicon. The attachment of CpFe on B-doped nanocarbon is a single step process<sup>20, 25-27</sup> and does not require noble metal compounds or multiple-step synthesis techniques.

However, the credibility of these CpFe/B-doped nanocarbon complexes for electrochemical applications as redox-active materials still requires an evaluation of their redox properties. In addition to the experimental techniques, density functional calculations (DFT) combined with an appropriate solvation model, such as the conductor-like polarizable continuum model (CPCM),<sup>28</sup> has been previously shown to accurately predict redox potentials in different solutions.<sup>29-34</sup> For instance, Cossi et al. reported a combined computational and experimental study of the redox potential of ferrocene stabilized on silica.<sup>29</sup> They calculated the redox potentials of ferrocene with different side chains in acetonitrile, which resulted in less than 3% difference with the experimental values.<sup>29</sup> In addition, Liu et al. benchmarked a series of different functionals and basis sets to calculate the redox potential of a protonated adrenaline/protonated adrenaline quinone couple.<sup>34</sup> The B3LYP functional with the 6-31+G(d,p) basis set was found to predict reasonable redox potentials compared to the experiments (an experimental value of 0.557 V versus a theoretical value of 0.581 V).

Since our previously-reported CpTM/B-doped nanocarbon complexes may be a competitive substitute for the redox-active monolayers in electrochemical sensing and other applications, in this work, we use a DFT-based approach to evaluate the redox properties of these

materials. The redox potentials of CpFe supported on B-doped, N-doped, and pristine graphene complexes in water and in acetonitrile have been calculated and benchmarked in order to identify the electrochemical sensing properties of our proposed complexes.

Our goal is to identify a material that exhibits a redox potential comparable to ferrocene or ferrocene derivatives. For the design of ferrocene-based electron donor-receptors, the desired redox potential ranges from 0.3 V to 0.9 V SHE,<sup>4, 29</sup> and the redox value of an isolated ferrocene molecule is 0.64 V in water and 0.67 V in acetonitrile.<sup>33</sup> For data storage applications, a lower potential is desired for energy-saving purposes. For instance, Choi et al. synthesized and investigated a ferrocene-based nonvolatile memory material with a redox potential of about 0.58 V.<sup>9</sup> In this paper, our simulations indicate that it is possible to achieve redox potential values of CpFe/BGr complexes close to those of the ferrocene molecule, which implies that these materials may be a latent substitute for ferrocene as a redox-active monolayer for electrochemical sensing (and possible DRAM applications).

### 3.2 Computational methods and models

In this paper, graphene clusters were chosen to model the nanocarbon supports (shown in Figure 3.1) with different doping elements and patterns: C<sub>42</sub> (Gr), C<sub>41</sub>B (BGr), C<sub>35</sub>B<sub>7</sub> (BC5Gr), and C<sub>41</sub>N (NGr). The models were created by placing the CpTM complex near the doped site of the support, with the edge of the graphene clusters terminated with hydrogen. In our work, redox potentials of the following cases are benchmarked:

- (a) CpFe supported on Gr, BGr, Gr and NGr;
- (b) CpFe supported on BGr with different side chains on the Cp ring (methyl, ethyl, vinyl, and ethynyl attachments);

- (c) CpFe supported on BGr in different solutions (water and acetonitrile);
- (d) CpTM support on BGr with TM = Fe, Co, Ni;
- (e) CpFe supported on BC5Gr, as in our previous work.<sup>20, 35</sup>

According to previous redox calculations of related systems,<sup>29, 34</sup> unless otherwise specified, all DFT calculations were performed using the Gaussian 03 package at the B3LYP/6-31G+(d,p) level of theory.<sup>36, 37</sup> All of the initial geometries were fully optimized without constraints, both in vacuum and in solutions (water or acetonitrile). The solvation energies were modeled using the CPCM model,<sup>28</sup> with the UAHF atomic radii sets.<sup>36</sup>

The redox potential versus standard hydrogen electrode (SHE) in solution can be obtained from the DFT-calculated energies of the species in vacuum and in solution, along with a proper thermodynamic cycle. In this work, we followed the thermodynamic cycle (shown in Figure 3.2).

According to Figure 3.2, the redox potential vs. SHE can be obtained using following equation:

$$E^{\circ} = -\frac{(\Delta G^{\circ}_{(gas)} + \Delta G^{\circ}_{(sol,complex\ cation)} - \Delta G^{\circ}_{(sol,complex)})}{nF} - 4.43V \quad (1)$$

In Eq. 1,  $E^{\circ}$  is the redox potential vs. SHE,  $n$  is the number of transferred electrons ( $n = 1$  in our case),  $F$  is the Faraday constant,  $\Delta G^{\circ}$  is the energy of the neutral and charged species in vacuum and in solution, and 4.43 V is the difference between the absolute electrode and the SHE. This routine has been benchmarked for a number of different systems, including a ferrocene-silica system, adrenaline, and many organic compounds, all yielding good agreement with the experimental values.<sup>29, 34, 38</sup> In this paper, unless specified, all redox potential values are normalized to the SHE.

To improve efficiency, we assumed that the differences of free energies were equal to the

difference of electronic SCF energies from the DFT results. This same approximation has been used in previous calculations involving ferrocene/silica complexes, still yielding reliable results.<sup>29</sup> To further validate our approximations, benchmarking was performed to evaluate the differences between the redox potentials calculated by using the SCF energies directly and by using free energies (with frequency calculations), and the differences were all shown to be less than 8%. Additional details are provided in the results and discussion section. In addition, we calculated the initial configurations of CpFe on BGr, Gr and NGr supports with different spin multiplicities and all of them preferred a low spin configuration. Therefore, in the following discussions, all of the calculations correspond to the lowest spin state.

In order to quantify charges, natural bond orbital (NBO) population analyses were performed, and deformation charge density plots and localized orbital locator (LOL) plots were developed to clarify the charge transfer mechanisms in our systems.<sup>39-41</sup> The deformation charge density is defined as:

$$\Delta\rho = \rho_{\text{red}} - \rho_{\text{ox}}, \quad (2)$$

where  $\rho_{\text{ox}}$  and  $\rho_{\text{red}}$  are the charge densities of the oxidized and reduced complexes, respectively. The localized orbital locator is a descriptor for the degree of the electron localization, which ranges from 0 to 1. According to this descriptor, the LOL value of spin-neutral free-electron gas is defined as 0.5. Therefore, a value lower than 0.5 denotes that the electrons at a certain point are more delocalized, whereas a value higher than 0.5 indicates high electron localization. The LOLs were calculated using the Multiwfn 3.3.4 software.<sup>42</sup>

### **3.3 Results and discussions**

#### *3.3.1 Geometries and energetics*

The optimized geometries of the neutral complexes in solution are shown in Figure 3.1. The geometries of CpFe on B-doped CNTs and pristine CNTs and graphene (in vacuum) were discussed extensively in our previous paper.<sup>20</sup> The effects of the solvation and changes in the total charge (according to a redox cycle) on the geometries of all complexes are small. For instance, the Fe-B distances within the neutral CpFe/BGr complex in vacuum and water are 2.247 Å and 2.254 Å, whereas the Fe-B distances of the CpFe<sup>+1</sup>/BGr cation in vacuum and water are 2.260 Å and 2.259 Å, respectively. The CpFe complex occupies the hollow site of the six-membered ring on BGr, Gr and NGr, as does CpCo on BGr. On the other hand, the CpNi complex prefers to adsorb near the B-C bond bridge site. These adsorbate structures are consistent with our previous results, which can be explained by the 18-electron rule (complexes with 18 valence electrons in their TM center, comparable to the ferrocene molecule, are more stable than other complexes).<sup>20</sup> In addition, for the complexes with hydrocarbon sidechains, the sidechains are oriented parallel to the BGr support.

In terms of the substrate geometry, both the B and N dopants induce slight geometric distortions, where the effect of N doping is stronger.<sup>43</sup> In CNT systems, the N doping causes the tube diameter to expand by approximately 14%. This effect can be explained by the electron-rich nature of the N dopant, which favors a more tetrahedral coordination than the carbon host.<sup>43</sup> In this work, a similar phenomenon can also be observed in CpFe/NGr in Figure 3.1, where the N-doped site is highly curved.

The binding energies of the neutral complexes are consistent with our previous work. However, for the cations, because of the strong charge redistribution during the redox procedure (which will be discussed later), the effects of the formal charges on the CpTM complexes and the substrate must be taken into consideration. The binding energies of the neutral complexes and

cations in water are shown in Figure 3.3. The binding energies (BE) are calculated by the following equation:

$$BE = E_{CpTM} + E_{graphene} - E_{CpTM+graphene}, \quad (3)$$

where  $E_{CpTM+graphene}$ ,  $E_{CpTM}$ , and  $E_{graphene}$  are the total energies of the complexes, the CpTM ligands, and the graphene substrate (which includes both pristine and doped cases), respectively. For the +1 cations, the  $E_{CpTM+graphene}$ ,  $E_{CpTM}$ , and  $E_{graphene}$  are assigned +1, +2, and -1 formal charges, respectively. These individual charges are consistent with an NBO analysis of the +1 complex. For the BEs of the neutral complexes, the trends generally agree with our previous work in vacuum.<sup>20</sup> The CpFe/BGr and CpCo/BGr have the highest BE, while the species adsorbed on Gr or NGr support yield a lower BE. However, the BEs of the cations are increased by 20%, 297%, 290%, 11%, and 176% compared to the neutral complexes for CpFe/BGr, CpFe/Gr, CpFe/NGr, CpCo/BGr, CpNi/BGr, respectively. It can be seen that the neutral complexes with lower stabilities are more affected by the oxidation. This phenomenon can be explained by the charge transfer during oxidation, which is discussed in detail later. For the application of CpTM/nanocarbons, especially for those less stable neutral complexes on pristine or N-doped supports, these results indicate that their stability may be improved by converting them into a salt, as a cation.

The binding between the Cp ring, TM atom, and the support can be seen on the LOL plot (Figure 3.4 and Figures B1 and B2 in the Supporting Information), where the delocalized interactions between CpFe and the support are illustrated, as well as the  $\pi$ -stacking interactions between the Cp ring and the support. These interactions as well as the delocalization of orbitals can also be seen in our MO analysis in section 3.3.4.

### 3.3.2 Redox potentials of CpFe/pristine, N-doped, and B-doped graphene complexes

Before we calculated the redox potentials of our complexes, the redox potentials of ferrocene molecules in water and acetonitrile were benchmarked using the thermodynamic cycle illustrated in Figure 3.2. The benchmark results are shown in Table B1 of the Supporting Information. For the ferrocene molecules in water and acetonitrile, the difference between the computational values and experimental values are smaller than 0.03 V, which provides good verification of the quantitative accuracy of our methods. Also, the effect of the zero-point energies (ZPE) on the redox potential of the CpFe/BGr complex is shown in Table B1, where a 0.04 V contribution to the free energy is found. Due to the purpose of this work, which is to survey the properties of prototype materials, these benchmarks demonstrate acceptable accuracy.

The calculated redox potentials of all complexes are shown in Figure 3.5. Generally speaking, the complexes with CpFe active centers and B-doped supports yield redox potential values close to the ferrocene molecule and its derivatives. As discussed in the introduction, the targeted redox potential values of the complexes are from 0.3 V to 0.9 V SHE, which corresponds to the characteristics of many ferrocene-based redox sensors. As a comparison, the redox potentials of silica-supported ferrocenes with different sidechains in acetonitrile have been found to vary from 0.6 V to 0.9 V.<sup>29</sup> Moreover, Cass et al. investigated a series of ferrocene derivatives for glucose sensing with redox potentials ranging from 0.34 V to 0.64 V.<sup>4</sup> For the CpFe/BC5Gr complex, the more electron-deficient B dopants raise the redox potential to 0.72 V, but it still falls within the 0.3 V to 0.9 V range. When comparing the redox potentials of different doping concentrations (2.3% for BGr and 16.6% for BC5Gr), it is observed that the effect of the doping concentration is only moderate, especially since the BC5Gr would be the upper doping limit of the experimental material.

The CpFe/Gr and CpFe/N-graphene complexes are predicted to have redox potentials of -1.17 V and -0.91 V, which indicates that they would act as strong reducing reagents. Thus, although the CpFe complexes on Gr and NGr may not be suitable as redox-active electrochemical sensing materials, their redox properties may conform to the needs of other electrochemical applications (as reducing agents).

As a comparison, the redox potential of the CpFe complex on BGr in acetonitrile has been evaluated, since acetonitrile is a popular solvent for ferrocene-based electrochemical sensing. The calculated redox potential is 0.67 V for the CpFe complex on BGr, which is higher than the potential in water. This shift in the redox value is consistent with experimental studies of ferrocene, in which the redox potential of ferrocene is found to be 0.64 V in water versus 0.69 V in acetonitrile.<sup>4</sup>

In ferrocene-based electrochemical systems, the presence of sidechains on the Cp ring of the active center plays an important role. These sidechain ligands can tune the redox properties of the ferrocene, and they can also stabilize the system in different environments. Therefore, we have performed additional calculations to evaluate the effects of the sidechains on the Cp ring, by characterizing complexes with different ligands (corresponding to varying the degree of unsaturation), as summarized in Figure 3.5. The Cp rings with methyl, ethyl, and vinyl sidechains are found to have lowered redox potentials, while the ethynyl sidechain corresponds to a higher value. In Cossi et al.'s work, ethyl, vinyl and ethynyl ferrocene were benchmarked both experimentally and computationally. The ethyl-ferrocene exhibited the lowest redox potential whereas the ethynyl-ferrocene showed the highest.<sup>29</sup> Our predicted trends of the redox potential, with respect to varying sidechains, closely matches the trends from Cossi et al.'s study of ferrocene on silica.<sup>29</sup> This trend can be explained by the electron-donating tendencies of the

sidegroups, which (in the case of methyl, ethyl, and vinyl) cause the Cp ring to grow more nucleophilic, and thus quench the redox potential. Meanwhile, the highly unsaturated sidechain (the ethyl group) is more electron-withdrawing, which tends to make the conjugated system more electrophilic.

The effects of B-doping (p-type doping) and N-doping (n-type doping) within nanocarbons have been studied extensively by our group using computational techniques.<sup>20, 21, 35, 43-46</sup> With respect to both B-doped and N-doped carbons, the doping tends to both enhance the adsorption and increase the conductivity of the supports. For the B-doping, our previous study<sup>35, 43-45</sup> and that of Groves et al.<sup>47</sup> found that the dopants invoke a strong charge imbalance of the surrounding carbon atoms, which provides a large contribution to the enhanced binding. Similar to the effects of the sidechains on the Cp ring, the electron-deficient B dopant and the electron-rich N dopant also directly affected the redox properties, due to their corresponding electron affinity. However, since a large conjugated system like graphene may be involved with both the charge transfer and the redox reaction, the details of the dopant effects on the redox properties are discussed later.

### *3.3.3 Redox potentials of CpCo and CpNi/B-doped graphene complexes*

Both the cobaltocene and nickelocene are known to be unstable compounds, which can easily react with oxygen in the air.<sup>48</sup> However, due to the stabilization of CpCo and CpNi on B-CNT that we found in our previous work,<sup>20</sup> CpCo and CpNi/BGr complexes are included in the present study. The optimized geometries are shown in Figure 3.1. The redox potentials of CpCo/BGr and CpNi/BGr in water are predicted to be -0.10 V and -0.31 V, respectively. In addition, slightly higher redox potentials of 0.06 V and -0.18V are calculated in acetonitrile for

CpCo/BGr and CpNi/BGr, respectively. According to these redox potentials, both of these complexes function as reducing agents with large negative potential values or as weak oxidation agents with very small positive values in water and acetonitrile. These results indicate these complexes would be unsuitable as redox-active materials in ferrocene-related applications.

### 3.3.4 Charge transfer and frontier orbital analysis of the redox process

The charge transfer during the redox reaction process can be directly visualized using deformation charge density plots. In our previous work, the deformation charge densities were used to analyze the binding of CpTM complexes on B-doped carbon nanotubes (B-CNT).<sup>20</sup> These plots indicated that the enhanced binding was correlated to the increased charge transfer between CpTM and B-CNT. The charge transfer before/after the redox process of the CpFe/BGr complex is visualized in Figure 3.6. Large charge redistribution can be seen among the CpFe complex and the BGr support. In addition, for the CpFe complex on the NGr support, the charges are redistributed through the support (but less obvious compared to the BGr support). On the contrary, for the CpFe complex and the Gr support, the charge transfer is more localized around the Fe atom and the Cp ring.

According to frontier orbital theory, the redox properties are related to the highest occupied orbitals (HOMO) and lowest unoccupied orbitals (LUMO). For instance, by analyzing the HOMO and LUMO using DFT calculations, Karr et al. was able to identify the electron transfer sites of porphyrin-attached supramolecular complexes.<sup>49</sup> Thus, in this work, the HOMO and LUMO of solvated CpFe/BGr complexes are visualized in Figures 3.7 and 3.8. It is found that the HOMO and LUMO of the CpFe/BGr molecule and +1 cation are delocalized through the CpFe active center and the BGr support, and the one-electron redox reaction mainly takes place

in the HOMO. Combining results from the charge deformation plots and the HOMO/LUMO analysis, we conclude that both the CpFe active center and the BGr support contribute to the redox properties. In addition, the HOMOs and LUMOs of the neutral and +1 charged complexes are close in energy. The HOMOs of the CpFe/Gr and NGr are more localized, which are consistent with the deformation charge densities.

To quantitatively analyze the charge transfer, NBO partial charge analyses are shown in Figure 3.9, for the FeCp complexes and the supports. When comparing the partial charges of the same oxidation states in vacuum and in solution, the differences are small. However, the redox process makes the covalently-bound neutral complex into a more “ionic” positively-charged cation. The neutral complexes are consistent with our previous work, where the bonding of the CpFe and the support is covalent in nature, and the partial charge of Fe is around +0.7 to +0.8.<sup>20</sup> However, the cation exhibits a charge distribution that is close to the formal charges of -1, +3, and -1 for the Cp ring, Fe atom, and the BGr support, respectively. The formal charges of the Fe atom and the two Cp rings in ferrocenium ( $\text{Cp}_2\text{Fe}^{+1}$ ) are similar to these results (i.e., 1, +3, and -1). Thus, a reasonable comparison of the redox potentials of CpFe/BGr and ferrocene can be made, by consideration of the dopant properties and the degree of the orbital delocalization. In addition, the sum of the partial charges of the six-membered ring within the support near the CpFe complex of CpFe/BGr, CpFe/Gr and CpFe/NGr is +1.51, +2.13 and +1.54 (highlighted in Figure 3.9), respectively. Besides the less delocalized CpFe/Gr, both CpFe/BGr and CpFe/NGr show similar local charges of the six-membered ring within the support near the CpFe complex, which indicates that the effects of the CpFe complex on different doped local supports is comparable. This similarity of local environment despite of different supports implies that the redox properties of CpFe based complexes are likely to be retained as the properties (e.g. doping

pattern, size, etc.) of the supports vary.

As discussed previously, electron-withdrawing dopants will increase the redox potential, while the electron-donating dopants will decrease it. Moreover, a more delocalized HOMO will facilitate the charge redistribution throughout the support and make the final charge distribution close to the ferrocenium. Thus, the observed redox potentials of these complexes can be seen as resulting from a combination of these two mechanisms. For instance, the CpFe/BGr has both an electron-withdrawing B dopant and a more delocalized HOMO. Therefore, it exhibits the highest and closest redox potential to the ferrocene. On the contrary, the lowest redox potential is found for the CpFe/Gr complex, due to its localized HOMO. In the CpFe/NGr case, the N dopant promotes the HOMO delocalization, but the N dopant is electron-donating. Therefore, the final redox potential of the CpFe/NGr complex lies between the complexes with the BGr and Gr supports. The relationship between the redox potential and the nature of the dopant enables future design of redox-active materials with desired redox properties.

### **3.4 Conclusions**

In summary, the redox properties of CpTM adsorbed on different graphitic substrates (BGr, Gr and NGr) have been studied with DFT calculations, combined with implicit solvation models. In search of an integrated redox-smart material, our intent was to identify materials with comparable redox properties to ferrocene and other ferrocene-based electrochemical systems. Accordingly, complexes with a variety of transition metal cores, Cp sidechains, and doped graphene supports were evaluated in different solution environments. Among the materials evaluated, CpFe/BGr complexes (with different sidechains) exhibited similar redox properties to a ferrocene molecule and to other ferrocene-based electrochemical sensors, which implies that

these complexes may serve as direct replacements in some electrochemical systems. In addition, the frontier orbital analyses, the deformation charge densities, and the NBO partial charges demonstrate that the charge transfer during the redox process is redistributed through the CpFe active center and the support, which makes the charge distributions of positively-charged complexes closer to an ionic formal charge state.

Though these CpFe/B-doped nanocarbon complexes have not been experimentally synthesized, syntheses strategies for similar compounds have been developed and tested extensively.<sup>25-27, 50</sup> Considering the direct attachment procedure, the high stability, and high conductivity, these complexes may be new candidates for redox-smart materials.

### **Acknowledgments**

This work was supported by the NSF CAREER Award (no. 0747690). Supercomputer resources were provided by the Alabama Supercomputer Center.

**Supporting Information Available:** Table of the benchmarks of our computational method. 2D LOL plots of the neutral CpFe/Gr and CpFe/NGr in water. This material is available in Appendix B.

## References

- (1) Long, N. J., *Metallocene: an Introduction to Sandwich Complexes*. Blackwell Science: Oxford, OX ; Malden, MA, USA, **1998**.
- (2) Wu, X. J.; Zeng, X. C., Double Metallocene Nanowires. *J. Am. Chem. Soc.* **2009**, *131*, 14246- 14248.
- (3) Zhang, X. Y.; Wang, J. L.; Gao, Y.; Zeng, X. C., Ab Initio Study of Structural and Magnetic Properties of TMn(ferrocene)(n+1) (TM = Sc, Ti, V, Mn) Sandwich Clusters and Nanowires (n = infinity). *ACS Nano* **2009**, *3*, 537-545.
- (4) Cass, A. E. G.; Davis, G.; Francis, G. D.; Hill, H. A. O.; Aston, W. J.; Higgins, I. J.; Plotkin, E. V.; Scott, L. D. L.; Turner, A. P. F., Ferrocene-mediated Enzyme Electrode for Amperometric Determination of Glucose. *Anal. Chem.* **1984**, *56*, 667-671.
- (5) Dicks, J. M.; Aston, W. J.; Davis, G.; Turner, A. P. F., Mediated Amperometric Biosensors for D-galactose, Glycolate and L-amino-acids Based on a Ferrocene-modified Carbon Paste Electrode. *Anal. Chim. Acta* **1986**, *182*, 103-112.
- (6) Roth, K. M.; Yasseri, A. A.; Liu, Z. M.; Dabke, R. B.; Malinovskii, V.; Schweikart, K. H.; Yu, L. H.; Tiznado, H.; Zaera, F.; Lindsey, J. S.; Kuhr, W. G.; Bocian, D. F., Measurements of Electron-Transfer Rates of Charge-Storage Molecular Monolayers on Si(100). Toward Hybrid Molecular/Semiconductor Information Storage Devices. *J. Am. Chem. Soc.* **2003**, *125*, 505-517.
- (7) Waser, R.; Dittmann, R.; Staikov, G.; Szot, K., Redox-Based Resistive Switching Memories - Nanoionic Mechanisms, Prospects, and Challenges. *Adv. Mater.* **2009**, *21*, 2632.
- (8) Jin, C.; Lee, J.; Lee, E.; Hwang, E.; Lee, H., Nonvolatile Resistive Memory of Ferrocene Covalently Bonded to Reduced Graphene Oxide. *Chem. Commun.* **2012**, *48*, 4235-4237.
- (9) Choi, T. L.; Lee, K. H.; Joo, W. J.; Lee, S.; Lee, T. W.; Chae, M. Y., Synthesis and Nonvolatile Memory Behavior of Redox-Active Conjugated Polymer-Containing Ferrocene. *J. Am. Chem. Soc.* **2007**, *129*, 9842- 9843.
- (10) Cummings, S. P.; Savchenko, J.; Ren, T., Functionalization of Flat Si Surfaces with Inorganic Compounds-Towards Molecular CMOS Hybrid Devices. *Coord. Chem. Rev.* **2011**, *255*, 1587-1602.
- (11) Zigah, D.; Herrier, C.; Scheres, L.; Giesbers, M.; Fabre, B.; Hapiot, P.; Zuilhof, H., Tuning the Electronic Communication between Redox Centers Bound to Insulating Surfaces. *Angew. Chem. Int. Ed. Engl.* **2010**, *49*, 3157-3160.
- (12) Hauquier, F.; Ghilane, J.; Fabre, B.; Hapiot, P., Conducting Ferrocene Monolayers on Nonconducting Surfaces. *J. Am. Chem. Soc.* **2008**, *130*, 2748- 2749.

- (13) Fabre, B., Ferrocene-Terminated Monolayers Covalently Bound to Hydrogen-Terminated Silicon Surfaces. Toward the Development of Charge Storage and Communication Devices. *Acc. Chem. Res.* **2010**, *43*, 1509-1518.
- (14) Fabre, B.; Hauquier, F., Single-component and Mixed Ferrocene-Terminated Alkyl Monolayers Covalently Bound to Si(111) Surfaces. *J. Phys. Chem. B* **2006**, *110*, 6848-6855.
- (15) Decker, F.; Cattaruzza, F.; Coluzza, C.; Flamini, A.; Marrani, A. G.; Zanoni, R.; Dalchiele, E. A., Electrochemical Reversibility of Vinylferrocene Monolayers Covalently Attached on H-terminated p-Si(100). *J. Phys. Chem. B* **2006**, *110*, 7374-7379.
- (16) Crumbliss, A. L.; Cooke, D.; Castillo, J.; Wisianneilson, P., Redox Properties of Phosphazene Polymers with Pendant Ferrocene Groups. *Inorg. Chem.* **1993**, *32*, 6088-6094.
- (17) Horikoshi, R.; Ueda, M.; Mochida, T., Side-chain Coordination Polymers Containing Redox-Active Pendants: Complexation of Ferrocene-Based Bidentate Ligands with M(hfac)(2) (hfac=1,1,1,5,5,5-hexafluoroacetylacetonate, M = Mn, Ni, Cu, Zn) and CuX (X = I, Br). *New J. Chem.* **2003**, *27*, 933-937.
- (18) Hardy, C. G.; Ren, L. X.; Tamboue, T. C.; Tang, C. B., Side-Chain Ferrocene-Containing (Meth)acrylate Polymers: Synthesis and Properties. *J. Polym. Sci., Part A: Polym. Chem.* **2011**, *49*, 1409-1420.
- (19) Grelaud, G.; Gauthier, N.; Luo, Y.; Paul, F.; Fabre, B.; Barriere, F.; Ababou-Girard, S.; Roisnel, T.; Humphrey, M. G., Redox-Active Molecular Wires Derived from Dinuclear Ferrocenyl/Ruthenium(II) Alkynyl Complexes: Covalent Attachment to Hydrogen-Terminated Silicon Surfaces. *J. Phys. Chem. C* **2014**, *118*, 3680-3695.
- (20) Zhang, Z. T.; Turner, C. H., Structural and Electronic Properties of Carbon Nanotubes and Graphenes Functionalized with Cyclopentadienyl-Transition Metal Complexes: A DFT Study. *J. Phys. Chem. C* **2013**, *117*, 8758-8766.
- (21) Acharya, C. K.; Li, W.; Liu, Z. F.; Kwon, G.; Turner, C. H.; Lane, A. M.; Nikles, D.; Klein, T.; Weaver, M., Effect of Boron Doping in the Carbon Support on Platinum Nanoparticles and Carbon Corrosion. *J. Power Sources* **2009**, *192*, 324-329.
- (22) Wang, S. Y.; Cochell, T.; Manthiram, A., Boron-doped Carbon Nanotube-Supported Pt Nanoparticles with Improved CO Tolerance for Methanol Electro-Oxidation. *Phys. Chem. Chem. Phys.* **2012**, *14*, 13910-13913.
- (23) Wang, J. J.; Chen, Y. G.; Zhang, Y.; Ionescu, M. I.; Li, R. Y.; Sun, X. L.; Ye, S. U.; Knights, S., 3D Boron Doped Carbon Nanorods/Carbon-Microfiber Hybrid Composites: Synthesis and Applications in a Highly Stable Proton Exchange Membrane Fuel Cell. *J. Mater. Chem.* **2011**, *21*, 18195-18198.
- (24) Deng, C. Y.; Chen, J. H.; Chen, X. L.; Mao, C. H.; Nie, L. H.; Yao, S. Z., Direct Electrochemistry of Glucose Oxidase and Biosensing For Glucose Based on Boron-Doped Carbon Nanotubes Modified Electrode. *Biosens. Bioelectron.* **2008**, *23*, 1272-1277.

- (25) Nakamura, E.; Koshino, M.; Saito, T.; Niimi, Y.; Suenaga, K.; Matsuo, Y., Electron Microscopic Imaging of a Single Group 8 Metal Atom Catalyzing C-C Bond Reorganization of Fullerenes. *J. Am. Chem. Soc.* **2011**, *133*, 14151-14153.
- (26) Amaya, T.; Sakane, H.; Hirao, T., A Concave-bound CpFe Complex of Sumanene as a Metal in a Pi Bowl. *Angew. Chem. Int. Ed. Engl.* **2007**, *46*, 8376-8379.
- (27) Petrukhina, M. A., Coordination of Buckybowls: The First Concave-bound Metal Complex. *Angew. Chem. Int. Ed. Engl.* **2008**, *47*, 1550-1552.
- (28) Barone, V.; Cossi, M., Quantum Calculation of Molecular Energies and Energy Gradients in Solution by a Conductor Solvent Model. *J. Phys. Chem. A* **1998**, *102*, 1995-2001.
- (29) Cossi, M.; Iozzi, M. F.; Marrani, A. G.; Lavecchia, T.; Galloni, P.; Zanoni, R.; Decker, F., Measurement and DFT Calculation of Fe(cp)(2) Redox Potential in Molecular Monolayers Covalently Bound to H-Si(100). *J. Phys. Chem. B* **2006**, *110*, 22961-22965.
- (30) Phillips, K. L.; Sandler, S. I.; Chiu, P. C., A Method to Calculate the One-Electron Reduction Potentials for Nitroaromatic Compounds Based on Gas-Phase Quantum Mechanics. *J. Comput. Chem.* **2011**, *32*, 226-239.
- (31) Psciuk, B. T.; Lord, R. L.; Munk, B. H.; Schlegel, H. B., Theoretical Determination of One-Electron Oxidation Potentials for Nucleic Acid Bases. *J. Chem. Theory Comput.* **2012**, *8*, 5107-5123.
- (32) Merli, D.; Dondi, D.; Pesavento, M.; Profumo, A., Electrochemistry of Olanzapine and Risperidone at Carbon Nanotubes Modified Gold Electrode through Classical and DFT Approaches. *J. Electroanal. Chem.* **2012**, *683*, 103-111.
- (33) Namazian, M.; Lin, C. Y.; Coote, M. L., Benchmark Calculations of Absolute Reduction Potential of Ferricinium/Ferrocene Couple in Nonaqueous Solutions. *J. Chem. Theory Comput.* **2010**, *6*, 2721-2725.
- (34) Liu, T.; Du, C. M.; Yu, Z. Y.; Han, L. L.; Zhang, D. J., Prediction of Redox Potentials of Adrenaline and Its Supramolecular Complex with Glycine: Theoretical and Experimental Studies. *J. Phys. Chem. B* **2013**, *117*, 2081-2087.
- (35) Acharya, C. K.; Turner, C. H., Stabilization of Platinum Clusters by Substitutional Boron Dopants in Carbon Supports. *J. Phys. Chem. B* **2006**, *110*, 17706-17710.
- (36) Frisch, M. J.; Trucks, G. W.; Schlegel, H. B.; Scuseria, G. E.; Robb, M. A.; Cheeseman, J. R.; Scalmani, G.; Barone, V.; Mennucci, B.; Petersson, G. A. et al. Gaussian 03, Revision D.02. Wallingford CT, **2004**.
- (37) Becke, A. D., Density-functional Thermochemistry .3. The Role of Exact Exchange. *J. Chem. Phys.* **1993**, *98*, 5648-5652.
- (38) Fu, Y.; Liu, L.; Yu, H. Z.; Wang, Y. M.; Guo, Q. X., Quantum-chemical Predictions of

- Absolute Standard Redox Potentials of Diverse Organic Molecules and Free Radicals in Acetonitrile. *J. Am. Chem. Soc.* **2005**, *127*, 7227-7234.
- (39) Reed, A. E.; Curtiss, L. A.; Weinhold, F., Intermolecular Interactions from a Natural Bond Orbital, Donor-Acceptor Viewpoint. *Chem. Rev.* **1988**, *88*, 899-926.
- (40) Silvi, B.; Savin, A., Classification of Chemical-Bonds Based on Topological Analysis of Electron Localization Functions. *Nature* **1994**, *371*, 683-686.
- (41) Schmider, H. L.; Becke, A. D., Chemical Content of The Kinetic Energy Density. *J. Mol. Struct. (Theochem.)* **2000**, *527*, 51-61.
- (42) Lu, T.; Chen, F. W., Multiwfn: A multifunctional wavefunction analyzer. *J. Comput. Chem.* **2012**, *33*, 580-592.
- (43) An, W.; Turner, C. H., Chemisorption of Transition-Metal Atoms on Boron- and Nitrogen-Doped Carbon Nanotubes: Energetics and Geometric and Electronic Structures. *J. Phys. Chem. C* **2009**, *113*, 7069-7078.
- (44) Acharya, C. K.; Sullivan, D. I.; Turner, C. H., Characterizing the Interaction of Pt and Pt<sub>n</sub> Clusters with Boron-Doped, Nitrogen-Doped, and Activated Carbon: Density Functional Theory Calculations and Parameterization. *J. Phys. Chem. C* **2008**, *112*, 13607-13622.
- (45) An, W.; Turner, C. H., Transition-Metal Strings Templated on Boron-Doped Carbon Nanotubes: A DFT Investigation. *J. Phys. Chem. C* **2009**, *113*, 15346-15354.
- (46) An, W.; Turner, C. H., Structural, Electronic, and Magnetic Features of Platinum Alloy Strings Templated on A Boron-Doped Carbon Nanotube. *Phys. Rev. B* **2010**, *81*, 205433.
- (47) Groves, M. N.; Malardier-Jugroot, C.; Jugroot, M., Improving Platinum Catalyst Durability with a Doped Graphene Support. *J. Phys. Chem. C* **2012**, *116*, 10548-10556.
- (48) Gubin, S. P.; Smirnova, S. A.; Denisovich, L. I., Redox Properties of Cyclopentadienylmetal Compounds .2. Cobaltocene, Nickelocene and Related Compounds. *J. Organomet. Chem.* **1971**, *30*, 257-265.
- (49) Karr, P. A.; Zandler, M. E.; Beck, M.; Jaeger, J. D.; McCarty, A. L.; Smith, P. M.; D'Souza, F., Predicting the Site of Electron Transfer Using DFT Frontier Orbitals: Studies on Porphyrin Attached Either to Quinone or Hydroquinone, and Quinhydrone Self-Assembled Supramolecular Complexes. *J. Mol. Struct. (Theochem.)* **2006**, *765*, 91-103.
- (50) Sarkar, S.; Niyogi, S.; Bekyarova, E.; Haddon, R. C., Organometallic Chemistry of Extended Periodic Pi-Electron Systems: Hexahapto-Chromium Complexes of Graphene and Single-Walled Carbon Nanotubes. *Chem. Sci.* **2011**, *2*, 1326-1333.

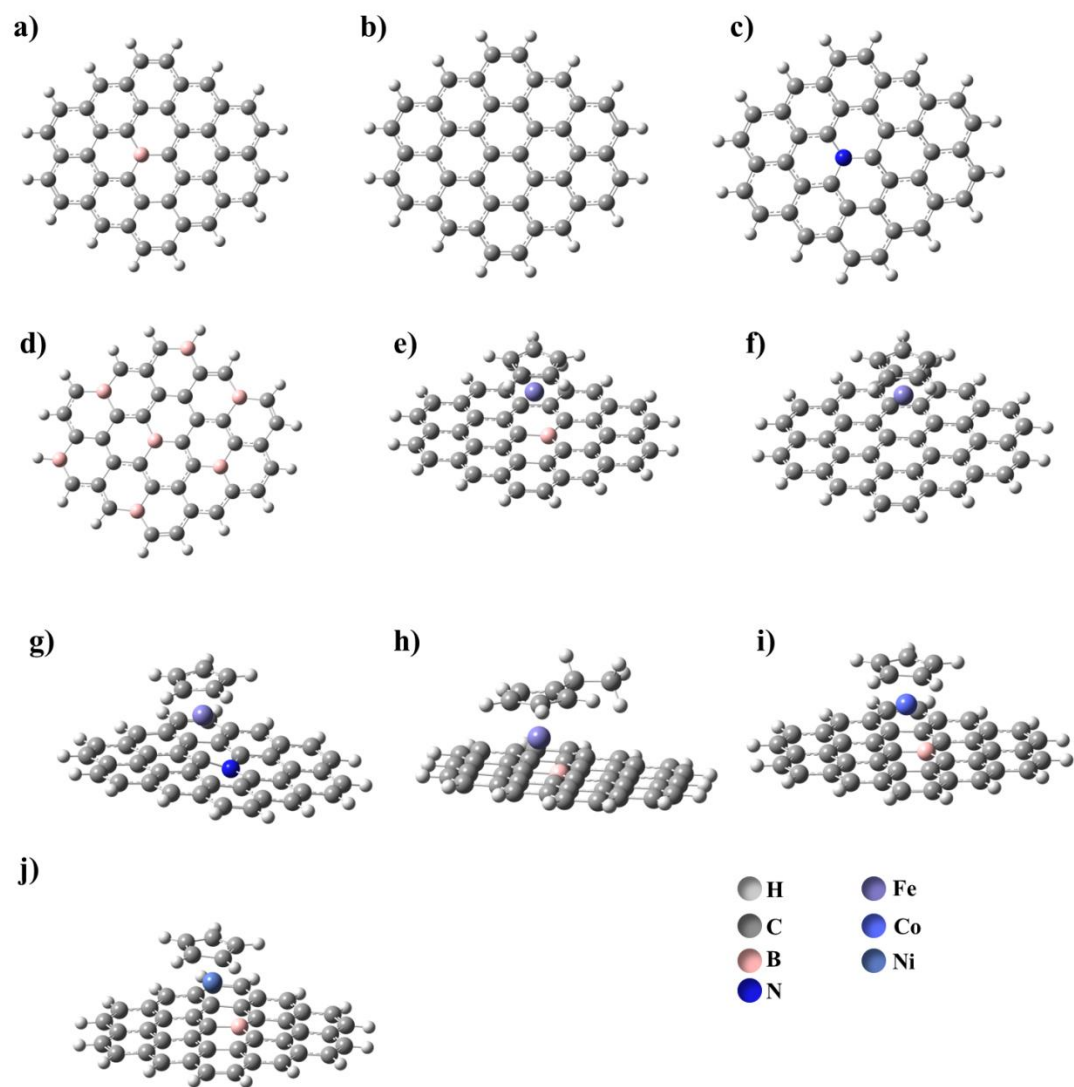


**Figure 3.1.** Optimized structures of a) BGr support; b) Gr support; c) NGr support; d) BC5Gr support; E) CpFe/BGr in water; f) CpFe/Gr in water; g) CpFe/NGr in water; h) CpFe/BGr in water with vinyl sidechain on the Cp ring; i) CpCo/BGr in water; and j) CpNi/BGr in water.

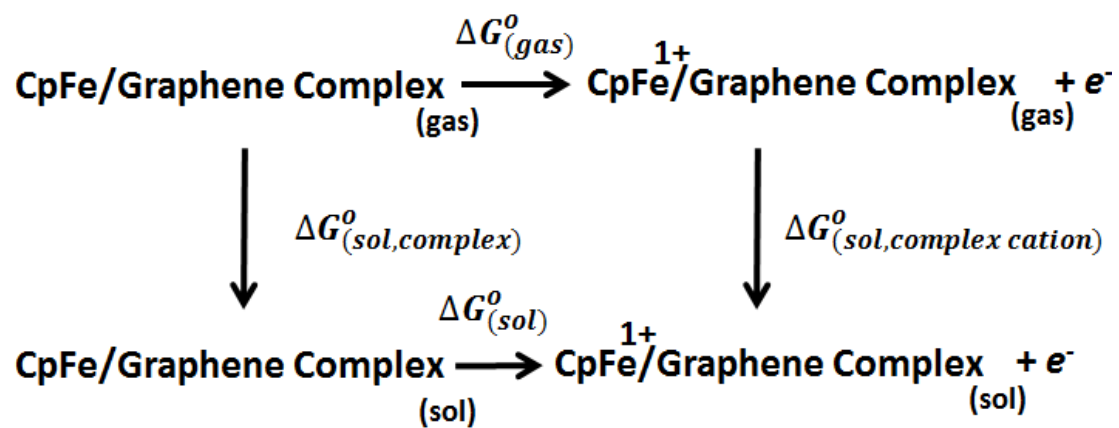


**Figure 3.2.** Thermodynamic cycle used for the redox potential calculation.

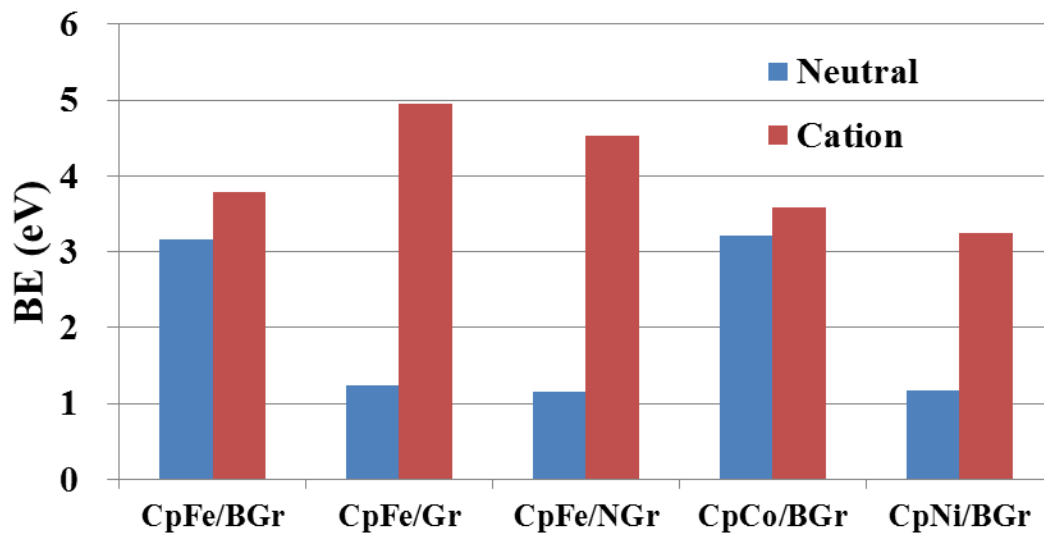


**Figure 3.3.** Binding energies of different neutral and positive charged complexes in water.

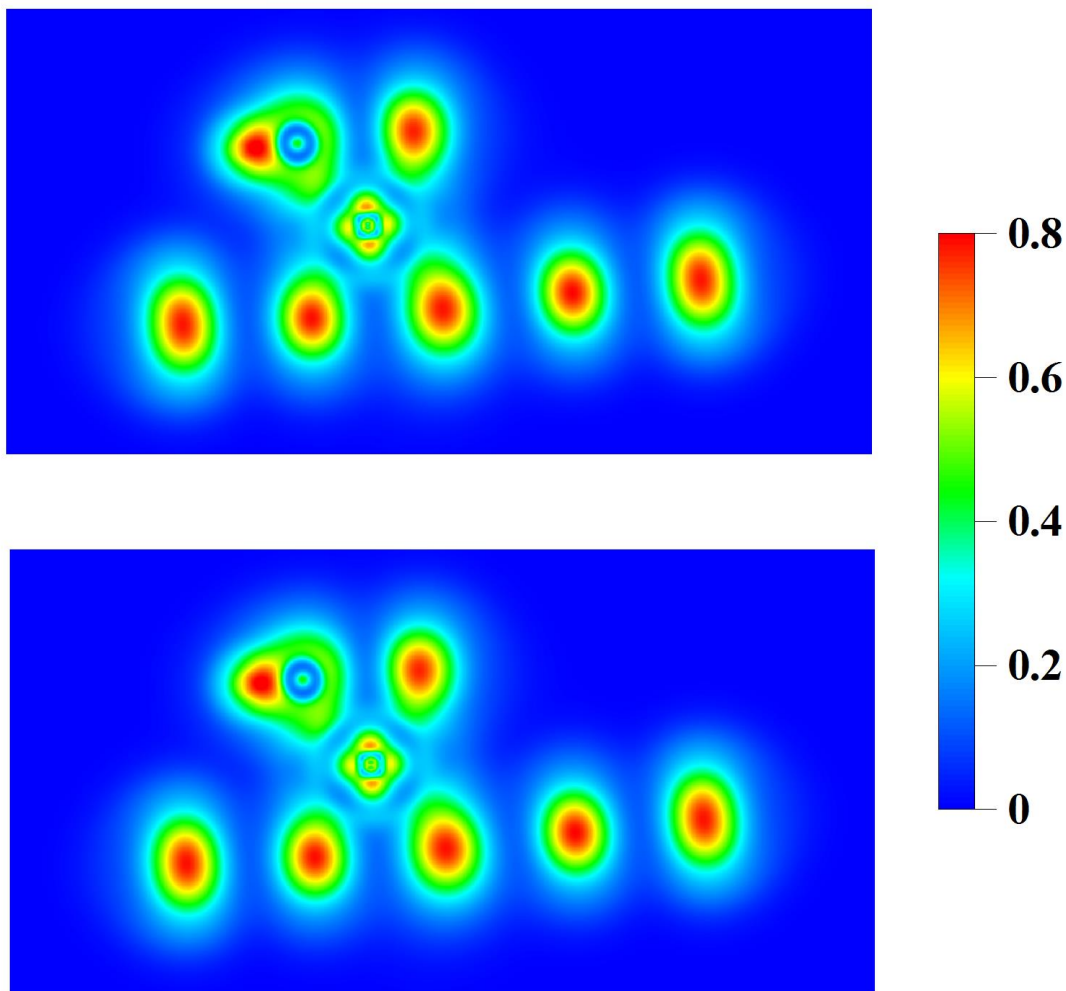


**Figure 3.4.** 2D LOL plot of a) the neutral CpFe/BGr and b) charged CpFe<sup>+</sup>/BGr in water. The value of LOL ranges from 0 (delocalized) to 0.8 (highly localized).

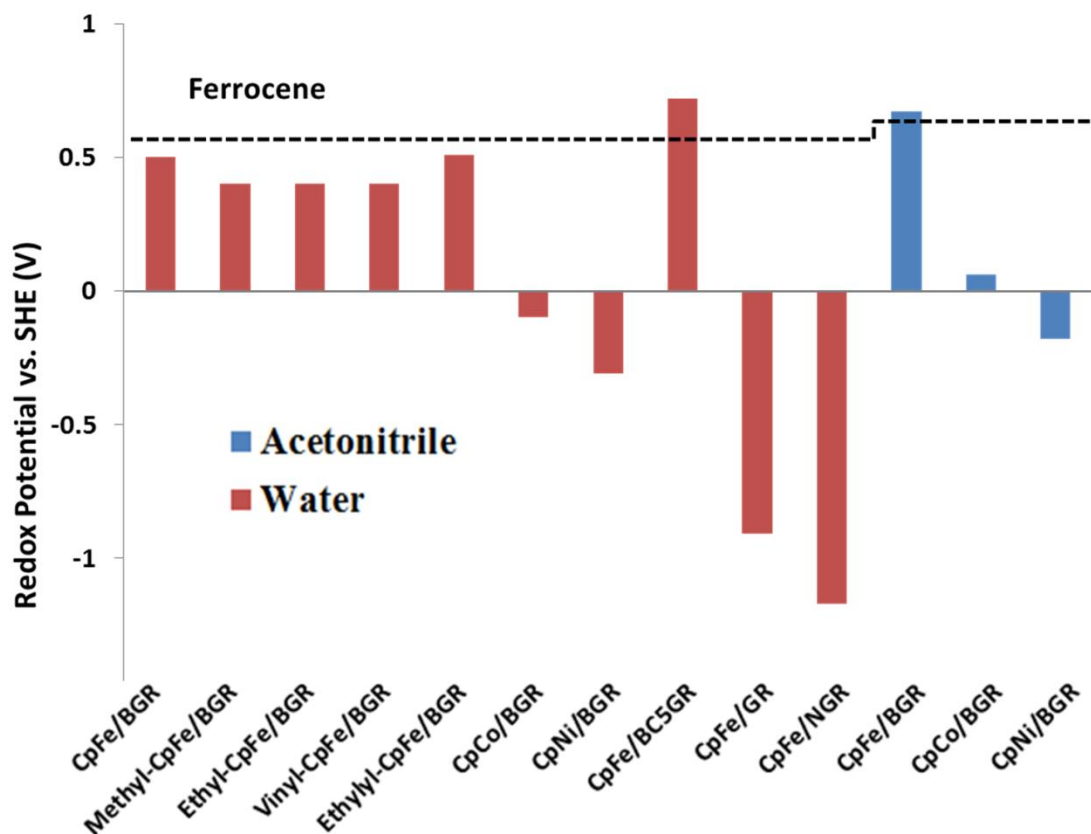


**Figure 3.5.** Redox potential of CpTM complexes with different TMs, sidechains, and solvents. The redox potentials in water and acetonitrile are colored red and blue, respectively. The dashed black line correspond to the redox potential of a ferrocene molecule in water and in acetonitrile for comparison. Note that the step in the dashed line corresponds to the difference of the ferrocene redox potential in water and in acetonitrile.

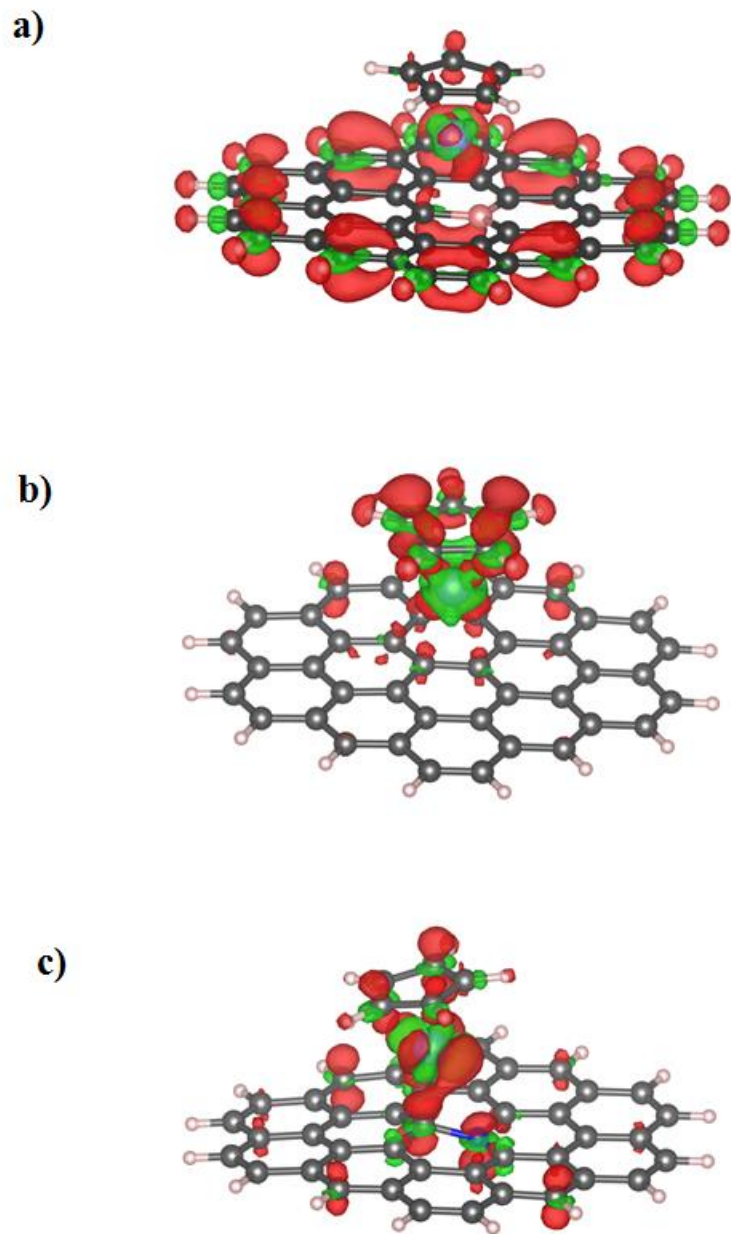


**Figure 3.6.** 3D-deformation charge density isosurface of a) CpFe/BGr complex; b) CpFe/Gr complex; and c) CpFe/NGr complex after the redox process, where red and green color denotes positive and negative values, respectively. The isovalue was chosen to be 0.02.

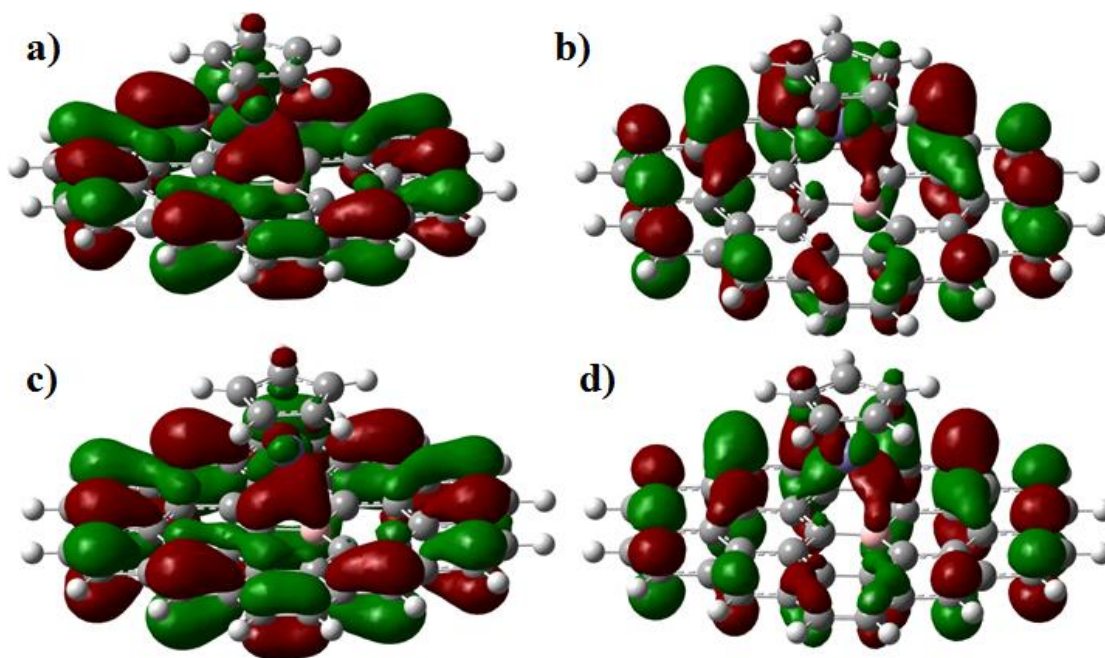


**Figure 3.7.** 3D orbital isosurface of CpFe/BGr complexes in water: a) HOMO of neutral CpFe/BGr complex; b) LUMO of neutral CpFe/BGr complex; c) HOMO of charged CpFe<sup>+</sup>/BGr complex; and d) LUMO of charged CpFe<sup>+</sup>/BGr complex. The red and green color denote positive and negative values, respectively. The isovalue was chosen to be 0.02.

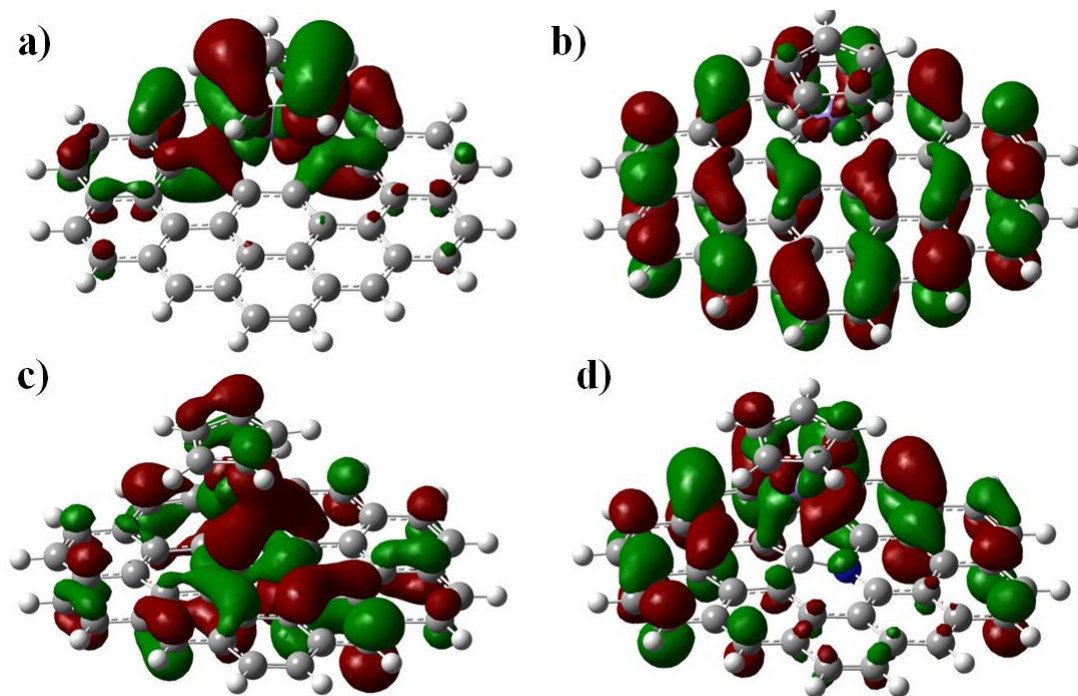


**Figure 3.8.** 3D orbital isosurface of CpFe/Gr and CpFe/NGr complexes in water: a) HOMO of neutral CpFe/Gr complex; b) LUMO of neutral CpFe/Gr complex; c) HOMO of neutral CpFe/NGr complex; and d) LUMO of neutral CpFe/NGr complex. The red and green color denoted to positive and negative values, respectively. The isovalue was chosen to be 0.02.

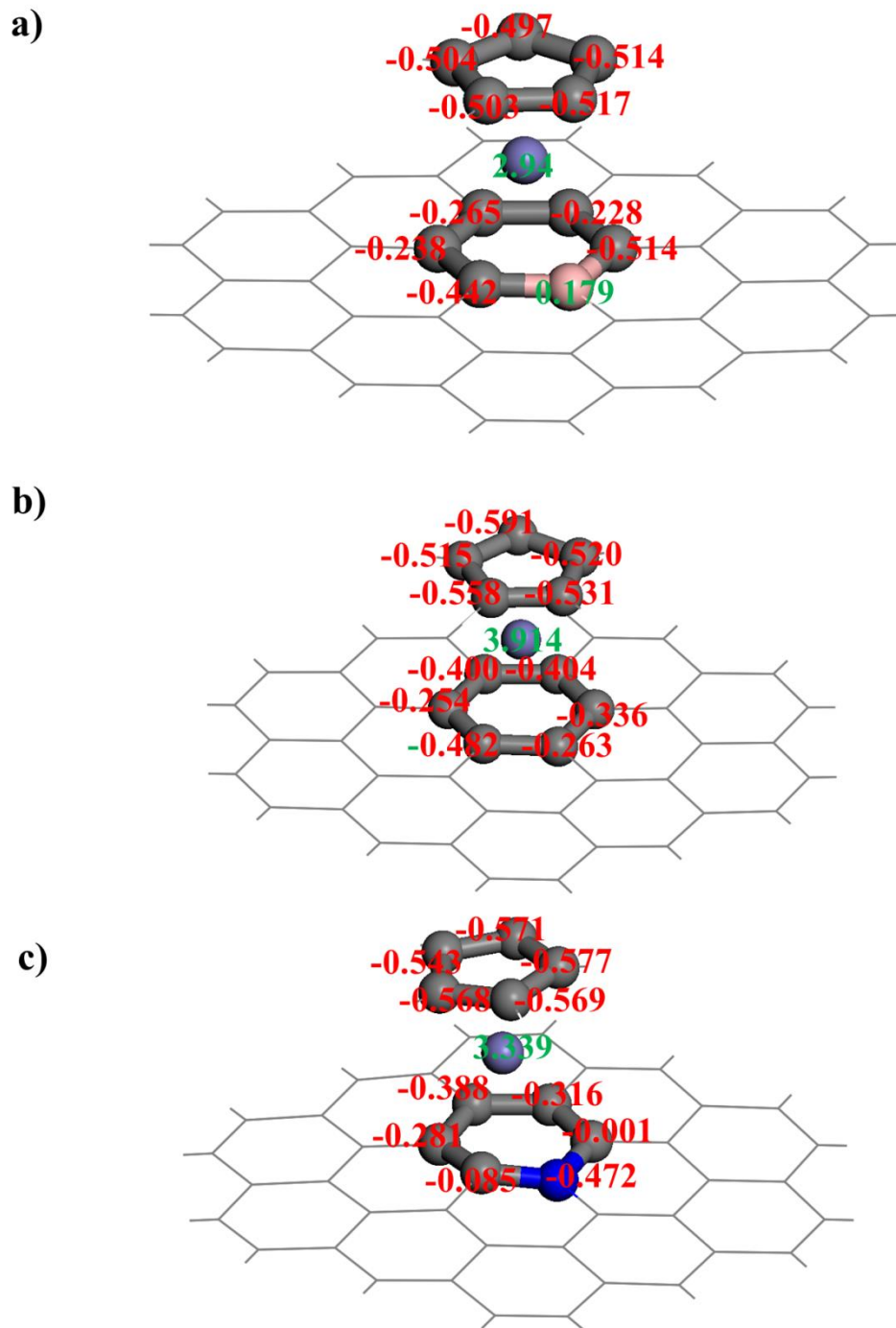


**Figure 3.9.** NBO partial charges of: a) charged  $\text{CpFe}^{+1}/\text{BGr}$ ; b) charged  $\text{CpFe}^{+1}/\text{Gr}$ ; and c) charged  $\text{CpFe}^{+1}/\text{NGr}$  in water. H atoms are omitted for clarity.

Appendix B. Supporting Information for Chapter 3.

**Table B1.** Benchmarks of our computational method.

<i>System</i>	<b>Pontential vs. SHE (V)</b>		
	<i>Experimental</i>	<i>DFT with Free Energy</i>	<i>DFT without Free energy</i>
<b>Ferrocene/Water</b>	0.64		0.59
<b>Ferrocene/Acetonitrile</b>	0.69		0.67
<b>CpFe/BGr</b>		0.46	0.50

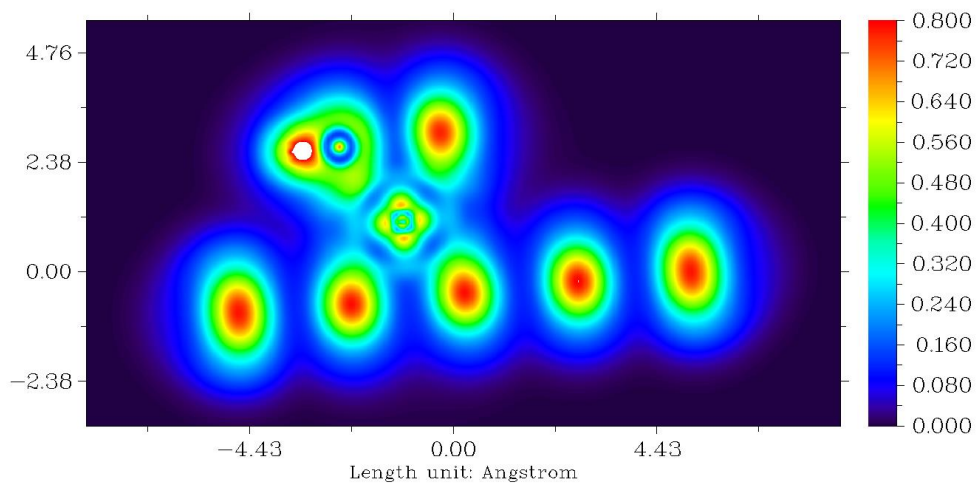


**Figure B1.** 2D LOL plot of the neutral CpFe/Gr in water. The value of LOL ranged from 0 to 0.8 and colored from blue to red.

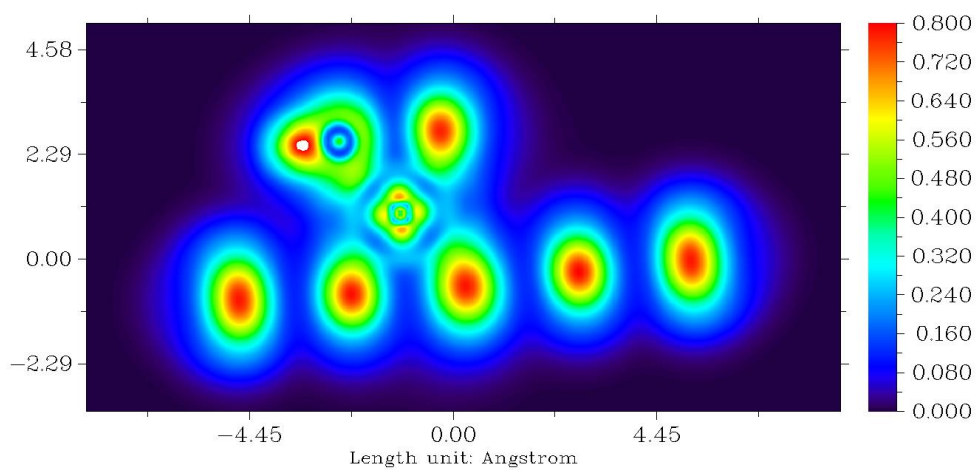


**Figure B2.** 2D LOL plot of the neutral CpFe/NGr in water. The value of LOL ranged from 0 to 0.8 and colored from blue to red.

CHAPTER 4  
WATER-INDUCED INTERACTIONS BETWEEN BORON-DOPED CARBON  
NANOTUBES\*

#### 4.1 Introduction

The dispersion of carbon nanotubes (CNT)<sup>1</sup> and other nanocarbons is an important aspect in a variety of real-world applications. A stable dispersion of CNTs is needed for effectively separating, purifying and incorporating these materials into their final applications (from structural reinforcements<sup>2</sup> to electronic materials<sup>3</sup>). However, due to the strong inter-tubular van der Waals interactions leading to hydrophobic behavior, CNTs are known to aggregate after synthesis.<sup>4</sup> Therefore, the homogenous dispersion of CNTs (with varying diameters, lengths, and chiralities) in aqueous solutions is considered to be one of the major challenges of CNT-related applications.

Recently, many additives have been reported to improve the dispersion of CNTs in aqueous solution, including surfactants,<sup>5-7</sup> dyes,<sup>8</sup> polymers,<sup>9</sup> ionic liquids,<sup>10</sup> and biomolecules.<sup>11</sup> These additives can be very effective dispersants in certain situations, but there can be limitations (in terms of thermal stability, pH sensitivity, etc.). Similar to our approach reported here, Blackburn et al. performed an experimental study on the dispersion properties of pristine and boron-doped CNTs (B-CNTs) in aqueous solution with the addition of surfactants.<sup>12</sup> Using Raman

---

\* Reprinted with permission from Journal of Physical Chemistry C, 2014, Volume 118, Page 17838-17846. Copyright 2014 American Chemical Society.

spectroscopy, the dispersion of the B-CNT materials was found to be enhanced, and this observation provides evidence that atomic doping may be an effective route for dispersing or separating CNTs. However, the origin of the dispersion phenomena is currently not well understood, and to the best of our knowledge, no following studies have been reported on the dispersion of B-CNTs. In addition, we have previously reported that B-doped carbon materials can provide unique material properties, showing potential applications in catalysis, sensing, and novel electronic materials.<sup>13-19</sup> Among those B-CNT based system, the hydration behavior of B-CNTs is a key performance factor. Therefore, a molecular simulation study of B-CNT dispersion can provide insight into the underlying interactions that dictate the solvation behavior, and this can lead to rational design strategies for improving dispersion properties.

In previous studies, molecular dynamics (MD) simulations have been extensively used for quantifying the hydration and molecular-level interactions of pristine CNTs in aqueous solution.<sup>20, 21</sup> For instance, MD simulations of the dispersion of CNTs and other nanocarbons have been conducted in water, water solutions with polymers, and with surfactants. Using MD simulations, Walther et al.<sup>22</sup> investigated the hydration and debundling of C<sub>60</sub> and CNTs in water by calculating and analyzing their potential of mean force (PMF) and water density profiles. A vapor-liquid-like interface was found to form at the hydrophobic-hydrophilic regions in their simulations. In addition, Walther et al. also reported that their dispersed CNTs tended to reaggregate together.

When performing MD simulations of B-CNTs, one important challenge is to correctly parameterize the strongly polarized B-C bonds in the B<sub>x</sub>C<sub>y</sub> materials.<sup>17, 18, 23</sup> Therefore, a force-field containing partial charges calculated from first-principles calculations, like density functional theory (DFT), is necessary for performing accurate MD simulations of B-CNT

systems. A rigorous population analysis method is important for obtaining suitable partial charges from first-principle calculations, since crude partial charge assignments may significantly alter the MD results. For example, Aluru et al.<sup>24</sup> conducted MD investigations on boron-nitride nanotube (BNNT) systems with similar B-N polarized bonds, and as input to the simulations, CHELPG partial charges<sup>25</sup> were predicted from DFT calculations using cluster models. This choice was motivated by CHELPG's ability to reproduce accurate electrostatic potentials (ESP) of the system.<sup>24, 26</sup> In addition, several population analysis methods have been used to generate accurate ESPs of periodic systems, like REPEAT (repeating electrostatic potential extracted atomic) charge by Campana et al.<sup>27</sup> and its improved version by Karl Johnson et al.,<sup>28</sup> plus the DDEC (density derived electrostatic and chemical) charge developed by Manz et al.<sup>29, 30</sup> These methods have been benchmarked with calculations of metal-organic frameworks, solid structures, and other nanostructures.<sup>30</sup> In particular, benchmarks using the DDEC method showed that DDEC was suitable for generating correct partial charges for periodic BNNT similar to our B-CNT system.<sup>29, 30</sup> Therefore, in this work, partial charges parameterized for our B-CNT force-field were calculated from DFT using both the CHELPG and the DDEC method, and comparison are made.

In this work, we develop a partial charge parameterization of several different B-CNT models: (a) periodic B-CNT (6,6) with two different doping patterns; (b) B-CNT (10,10); and (c) B-CNT (12,12) (B concentration ranges from 16.6% for our BC<sub>5</sub> model down to 12.5% for our B<sub>3</sub> model). We then perform MD simulations of the hydration, the potential of mean force (PMF), the water-induced interactions, and the debundling behavior of the B-CNT models (pairs and triplets) within aqueous solutions. The effective intertubular interactions between our B-CNT models are then used to parameterize Lennard-Jones (LJ) and Stockmayer potentials for

future coarse-grain simulations.<sup>31, 32</sup> Enhanced B-CNT-water interactions, as well as shifted interaction distances are observed (as compared to pristine CNTs). The simulation results provide important insight into the effects of B-doping on their dispersion behavior of CNTs, which is a key issue for engineering new substitutionally-doped CNT/graphene materials.

## 4.2 Computational methods

The structures of our B-CNT models were first optimized with DFT using the Vienna Ab-initio Simulation Package (VASP) with a periodic supercell model.<sup>33, 34</sup> Several different B-CNT models were tested, as well as a pristine CNT model:

- (a) **BC-I**: a periodic (6,6) B-CNT supercell with a  $BC_5$  stoichiometry;
- (b) **BC-II**: a periodic (6,6) B-CNT supercell with a “three-B” cluster doping pattern;
- (c) **BC-III**: a periodic (10,10) B-CNT supercell with a  $BC_5$  stoichiometry;
- (d) **BC-IV**: a periodic (12,12) B-CNT supercell with a  $BC_5$  stoichiometry; and
- (e) **C-I**: a periodic (6,6) CNT supercell.

The doping patterns of all B-CNT models are shown in Figure 4.1. The  $BC_5$  model has uniformly distributed B-doping sites, with a relatively high doping concentration (16.6%, compared with the highest experimental synthesis of about 15%).<sup>35</sup> Because both theoretical predictions and experimental evidence indicates the existence of boron clusters in B-doped nanocarbons,<sup>36, 37</sup> a  $B_3$  cluster model (BC-II) was modeled by randomly substituting  $B_3$  clusters with the CNT structure. This pattern leads to stronger local charges, curvature, and strain. These different doping concentrations and configurations are intended to probe the sensitivity of the results to the specific doping details (which are difficult to control experimentally). To provide the benchmark baseline for the B-CNTs, a pristine CNT(6,6) (C-I) was also included in our

simulations.

In addition, unless otherwise specified, the parameters of the DFT calculations were consistent with our previous DFT calculations of pristine and B-doped CNTs.<sup>13-15</sup> The generalized gradient approximation (GGA) functional of Perdew, Burke, and Ernzerhof (PBE)<sup>38</sup> and the projector-augmented wave (PAW)<sup>39</sup> method were used. The energy cutoff of the plane wave basis sets was 400 eV, and the Brillouin zone integration was performed by using  $1 \times 1 \times 5$  k-points within the Monkhorst-Pack scheme,<sup>40</sup> and first-order Methfessel-Paxton smearing of 0.2 eV was used for the geometry optimizations of the B-CNT models.<sup>41</sup> All geometries of the B-CNT models were fully optimized without constraints using the conjugate-gradient method, with a convergence of  $10^{-4}$  eV for the total energy and  $10^{-2}$  eV/Å in force on each atom. To generate accurate charge densities for DDEC partial charge fitting, a self-consistent field calculation on the optimized geometry was conducted using  $1 \times 1 \times 10$  k-points and  $288 \times 288 \times 96$  FFT integration grids. The partial charges were fitted from the DFT-calculated ESP and charge densities using the DDEC scheme.<sup>29, 30</sup> In addition, geometry optimization and partial charge analysis of analogous B-CNT models (shown in Figure C1) were performed using the Gaussian 09 package<sup>42</sup> at the B3LYP/6-31G\*\* level of theory with the CHELPG scheme.<sup>25</sup> These calculations were compared against the DDEC charges (considered our benchmark), in order to validate the use of CHELPG charges through the rest of our study. In addition, to further evaluate the reliability of CHELPG charges, a comparison was made between the PMFs of a solvated BC-I pair using DDEC and CHELPG partial charges. For simulation efficiency, CHELPG partial charges were preferred, and were thus used to parameterize the B-CNT models, whereas the DDEC partial charges were only generated for the BC-I model.

The molecular dynamics (MD) simulations were conducted using the Gromacs 4.54

simulation package.<sup>43</sup> Several different simulation runs were performed, corresponding to different box sizes, number of water molecules, and simulation times (for single, double and triple B-CNT systems), as shown in Table 3.1. The simulation cells were performed with periodic boundary conditions along all three dimensions, and larger simulation cells were used for the triple B-CNT systems to eliminate unwanted periodic interactions (cell dimension listed in Table 3.1). The pristine/B-doped CNTs were modeled as four supercells (optimized by DFT calculations),<sup>13</sup> and they were placed along the z-axis of the simulation box to represent infinitely long nanotubes. The structures of the nanotubes were kept rigid in all of the MD simulations, which is a reasonable approximation that has also been applied to other MD simulations of CNT dispersion.<sup>9, 21</sup> For the initial configurations, the angular orientations of each individual B-CNT about the z-axis within a bundle were optimized to their minimal values in vacuum. For the pristine CNTs, the energy differences between different initial angular configurations can be neglected. The Lennard-Jones parameters of the B and C atoms were taken from Kang and Hwang,<sup>44</sup> and these parameters were previously used to simulate fullerene interactions with CNT/BNNT and BN nanotube systems with water.<sup>24, 26, 44, 45</sup> Water molecules were modeled with the extended simple point charge (SPC/E) model,<sup>46</sup> which has been widely used and proven reliable for modeling water-CNT systems.<sup>20, 21, 24, 26, 45, 47</sup> The SETTLE algorithm was implemented for constraining the bond lengths and angles of SPC/E water.<sup>48</sup> All other LJ parameters for water-CNT interactions were calculated through Lorentz-Berthelot mixing rules,<sup>31</sup> truncated at a distance of 1.4 nm, with long-range dispersion corrections.<sup>31</sup> For all B-CNT models, partial charge sites with CHELPG calculated values were used (plus DDEC values were tested for the BC-I model), while all carbon atoms were neutral within the pristine CNT model. The coulomb interactions were modeled by the particle mesh Ewald (PME) method<sup>49</sup> with a 1.4

nm real space cut-off and a 0.16 nm FFT grid space. During the MD simulations, a leap-frog algorithm with a 1 fs time step was used to integrate the equations of motion. A canonical ensemble (NVT) with the Nose-Hoover thermostat<sup>50</sup> was used in all MD simulations to maintain the temperature at 300 K. The systems were calibrated by adjusting the x dimension of the simulation box until the bulk density of water was equal to the density of SPC/E water at 300 K according to the value of van der Spoel et al. (997kg/m<sup>3</sup>).<sup>51</sup> The snapshots of example simulation boxes with single, double, and triple B-CNT systems are shown in Figure 4.2.

## 4.3 Results and discussions

### 4.3.1 Partial charge calculation

The DDEC-calculated partial charges of the BC-I model are visualized in Figure 4.3, with the exact numerical values shown in Table C1. For comparison, the corresponding CHELPG charges with the same model are shown in Figure 4.3 and Table C1. For the average charges of B atoms, the DDEC calculated value (+0.244  $e$ ) was in good agreement with the CHELPG value (+0.235  $e$ ). Since our simulation model was periodic to mimic an infinitely long B-CNT, the difference between the partial charges located near the center and near the edge should be eliminated. As a comparison, the partial charge distributions of B atoms along the c-axis obtained by the periodic DDEC and non-periodic CHELPG methods are shown in Figure 4.3 for comparison. From Figure 4.3, both DDEC and CHELPG models demonstrate consistent partial charge distribution values and trends along the c-axis. This consistency is further validated by our MD simulation of the PMFs of the solvated BC-I nanotube with DDEC and CHELPG calculated partial charges (shown in Supporting Information, Figure C9). Virtually identical PMFs are obtained using either DDEC or CHELPG parameters.

### 4.3.2 CNT-CNT interactions in vacuum

#### 4.3.2.1 MD simulations

The potential of mean force (PMF) as a function of separation distance is a good descriptor for quantifying the direct and water-induced CNT-CNT interactions, since the PMF directly includes the contribution of the surrounding solvent molecules. The PMF is calculated by summing the contributions of interactions from direct nanotube-nanotube interactions and the contributions of water interactions along a series of different nanotube-nanotube distances. Thus, a positive value of the PMF indicates a repulsive interaction, while a negative value indicates an attraction between CNTs. In many studies of fullerenes, CNTs, and graphene interactions in water and/or surfactant environments, PMFs have been calculated and identified as a good criterion for evaluating water-induced interactions and dispersion properties.<sup>20-22, 52, 53</sup> In our simulations with two nanotubes present, the PMFs of pristine and B-doped CNTs interactions were obtained by selecting the x-axis as the reaction coordinate and then sampling the center of mass (COM) distance between the two nanotubes from 1.10 nm to 2.5 nm (25 total points).

The PMF results in vacuum are shown in Figure 4.4. To simplify our comparison of CNTs with different diameters, the CNT-CNT distance is defined as the minimal distance between two CNT atom centers, which is calculated using the diameter of the nanotube (distance from the nanotube COM to an atom center) subtracted from the COM distance. Generally speaking, all pristine and B-doped CNT bundles exhibit a repulsion-attraction curve, which is consistent with previous work on fullerenes, CNTs, and graphenes.<sup>53, 54</sup> For the pristine CNT-CNT PMF, the energy minimum is located at a separation distance of 0.316 nm, which is in good agreement with Girifalco et al.'s result (reported as a 1.128 nm COM distance, and equivalent to a 0.314 nm

CNT-CNT distance), obtained using a LJ-based continuum model.<sup>54</sup> For all of our B-CNT PMFs, the curves show similar repulsion-attraction patterns to the pristine CNTs at short separations, whereas attractive interactions tend to extend beyond those of the pristine CNT. For the BC-I models, the minimum PMF value is slightly higher than that of the pristine CNT (~4 kcal/mol), and the CNT-CNT distance corresponding to the PMF minimum is located at about 0.42 nm (a COM distance of 1.16 nm). This PMF difference can be attributed to the larger LJ  $\epsilon$  parameter for B than C (but a similar LJ  $\sigma$  value), plus the contributions of the Coulomb interactions at longer-range.<sup>44</sup>

The PMFs of BC-II pairs (B-CNT (6,6) containing B<sub>3</sub> clusters) exhibited a PMF comparable to the BC-I model, with slightly weaker interactions (likely due to the reduced doping concentration). Throughout our simulations, the general behavior of the B-CNT (6,6) models (BC-I and BC-II) was insensitive to the doping pattern, which implies that the experimental results would mimic this same insensitivity (relieving the experimental challenge of obtaining a specific doping arrangement). In addition, the B-CNT (10,10) (BC-III) and B-CNT (12,12) (BC-IV) exhibit a PMF minimum at 0.35 nm and 0.34 nm CNT-CNT distances (corresponding to 1.72 nm and 2.00 nm COM distances), respectively. These results also demonstrate a shifted potential-well distance, as compared with the pristine CNT (COM distance of 1.67 nm for BC-III and 1.94 nm for BC-IV). Because there is more contact area between nanotubes that have larger diameters, the potential wells decrease as the diameters of the B-CNT increase, and this trend is consistent with the PMFs of pristine CNTs in vacuum.<sup>54</sup>

#### 4.3.2.2 Coarse grain model parameterization

The PMFs of B-CNT bundles can be parameterized to provide models for future coarse-grain simulations of B-doped CNTs at larger scales. For example, Liba et al. established a

coarse-grain model for CNTs using LJ-style intertubular potentials with dissipative particle dynamics (DPD) simulations, and they obtained good agreement with respect to the intertubular interaction behavior, as compared to the experimental observations.<sup>55</sup> Therefore, we parameterized the intermolecular interactions between all four of our B-CNT models. Using weighted nonlinear least-square regression, the parameters for LJ potentials as well as Stockmayer potentials are fitted to the separation distance vs. PMF, normalized to the unit length of the B-CNTs. In this paper, the 12-6 style LJ potential function shown in Eq. 1 is used.<sup>31</sup>

$$u_{LJ} = 4\varepsilon\left[\left(\frac{\sigma}{r}\right)^{12} - \left(\frac{\sigma}{r}\right)^6\right] \quad (1)$$

Where  $u_{LJ}$  is the potential energy,  $r$  is the distance between two B-CNT surfaces, and  $\varepsilon$  and  $\sigma$  are the energy and length parameters, respectively. To better describe the interactions between dipoles, which the LJ potential lacks, a Stockmayer potential function is also parameterized. Because our models only describe parallel B-CNTs, the Stockmayer potential function can be simplified as shown in Eq. 2:<sup>32</sup>

$$u_{Stockmayer} = 4\varepsilon\left[\left(\frac{\sigma}{r}\right)^{12} - \left(\frac{\sigma}{r}\right)^6\right] - \frac{C}{r^3} \quad (2)$$

In Eq. 2, the meaning of  $r$ ,  $\varepsilon$  and  $\sigma$  are consistent with Eq. 1, and the  $C$  parameter describes the dipole interaction. The fitted parameters are shown in Table 4.2. The curves of the fitted and the original data corresponding to the BC-I model are shown in Figure 4.5, while the details of the fitting and the curves of BC-II, BC-III, and BC-IV are provided in the Supporting Information. Both the LJ and the Stockmayer models accurately reproduce the potential well depth, whereas the Stockmayer potential is clearly more accurate at longer ranges, as expected.

#### 4.3.3 CNT-CNT interactions in water

The PMFs of pristine and B-doped CNT(6,6) pairs (C-I and BC-I, respectively) solvated in

water are shown in Figure 4.6, while the PMFs of solvated BC-II, BC-III and BC-IV are shown in Figure C6, C7 and C8. The water-induced repulsion can be clearly observed in Figure 4.6, with the introduction of several new peaks. For the pristine CNTs (C-I), three repulsion peaks are located at COM distances of 1.3 nm, 1.6 nm, and 1.9 nm, which agree with previous MD simulation results.<sup>21</sup> In comparison to the pristine CNTs, the solvated PMF of B-CNT(6,6) pairs with the BC<sub>5</sub> pattern (BC-I) show a shifted and slightly prolonged water-induced repulsion peak at a COM distance from 1.2 nm to 1.4 nm. The repulsion maximum (and attenuated maxima at longer distances) is consistent with the features of the hydration layers shown in Figures 4.10 and 4.11, where the peaks and valleys correspond to the interactions of the first and second hydration layers. This is discussed in detail in section 4.3.3. In addition, the differences of aqueous-phase PMFs between the BC-I and BC-II models are small, with the maxima and minima differences of less than 1 kcal/mol at the same COM distance, again indicating that the solvation behavior is independent of the doping pattern.

The PMFs of BC-III and BC-IV pairs in water (Figures C7 and C8) show similar patterns to the (6,6) nanotube pairs. Interestingly, the trends of the height of the first repulsion peaks and the depth of the first and second attraction wells of B-CNT (6,6), (10,10), and (12,12) are generally proportional to their tube diameters (Figure 4.8). To investigate this trend, we decomposed the LJ and electrostatic contributions of the PMFs (shown in Figures 4.7, C6, C7, and C8). We can see that the contribution of the electrostatic interactions to the total PMFs increases with respect to the radius of the B-CNT. With respect to the first repulsion peak, the (repulsive) contributions of the coulomb interaction to the BC-I, BC-III and BC-IV PMFs are 5.8%, 7.1% and 7.5%, respectively. Interestingly, a sharp drop of the coulomb interactions can be seen at CNT-CNT distances of about 0.5 to 0.6 nm for all B-CNTs. These changes are likely caused by the water

molecules, which move in between the B-CNT at a well-defined distance, as shown in the 2D density profiles in Figures 4.10 and 4.11.

The PMF values of two pristine and B-doped CNTs in water are similar, but the curves are shifted, due to the different dispersion interactions introduced by the boron dopants. In order to investigate the aggregation behavior further, bundles of three BC-I and C-I tubes were modeled, with the PMFs shown in Figure 4.9. To ensure adequate sampling (as water molecules move in and out of the interior cavity created by the CNT bundles), each point on the PMF was averaged from three separate 5 ns runs. An increased repulsion energy peak as well as a prolonged interaction distance can be seen from the PMFs of the triple nanotube bundles. It can be seen from Figure 4.9 that the first repulsion maximum of B-CNT is about 5 kcal/mol higher (and displaced by 0.04 nm), as compared to the pristine CNT. The increased repulsion of the triple B-CNT bundles (as compared to the two B-CNT bundles) illustrates the importance of the neighboring interactions on the solvation behavior. Thus, considering the results of the triple-nanotube interactions, the B-CNTs are expected to provide a better dispersion than pristine CNTs. For the second and third repulsion peaks, the B-CNT bundle exhibits a comparable but prolonged interaction versus the pristine one, which is consistent with the results from the two CNTs bundles.

In addition, a PMF analysis of “squeezing” back the solvated triple CNT bundles has been conducted to further study the dispersion and hysteresis differences between pristine and B-doped CNTs. The PMFs of compressing the solvated B-doped and pristine CNTs are shown in Figure 4.9. A strong repulsion caused by the water structure surrounding the individual CNTs can be seen in Figure 4.9. For pristine CNTs, the PMFs of compression have two intersections with the expansion PMF curve at 1.36 nm and 1.45 nm, which indicates that the waters in the cavity

of three CNTs at that distance decrease the repulsion. For B-CNTs, however, much stronger repulsions during compression are observed, which indicates that the immediate surrounding water molecules are significantly stabilized, as compared to the water molecules surrounding the pristine CNTs. The stronger repulsion of water in the cavity of B-CNT than CNT can be explain by the prolonged interaction of B-CNT due to the larger  $\epsilon$  value for B than C as well as the electrostatic interaction. These phenomena indicate that once solvated, B-CNTs are more resistant to reagglomeration than pristine CNTs. Previous MD simulations showed that solvated pristine CNTs tend to permit water molecules to easily escape from neighboring nanotubes, allowing them to join together into large insoluble bundles.<sup>22</sup> Thus, although B-doping only imparts a moderate nanotube-nanotube repulsion interaction, as compared to the effects of surfactants or with the covalent attachment of hydrophilic function groups ( $\sim 10$  kcal/mol repulsion increase between two CNTs bundles),<sup>21</sup> the strong aggregation resistance of B-CNTs may play an important role in practical CNT-based technologies that prevent the application of traditional dispersants.

In this work, all of the CNT bundles are modeled using a parallel configuration, similar to most other molecular simulation studies of CNT hydration.<sup>20-22, 52, 53</sup> This is because CNTs tend to aggregate into parallel arrangements, due to strong intertubular interactions. However, the variation of the CNT orientation may also play a role in the hydration behavior. For instance, Angelikopoulos, et al.<sup>56</sup> reported a simulation study of perpendicular CNTs with amphiphilic coatings, which promoted a stable perpendicular configuration (improving the CNT dispersion). Therefore, an exploration of the B-CNT orientation during hydration would be a worthwhile topic for a future investigation.

#### 4.3.4 Water density profile and hydration properties

The water density profiles surrounding two BC-I and C-I bundles are shown in Figures 4.10 and 4.11, respectively. To better visualize the water solvation layers around the nanotubes, a 3D isosurface of water density profiles are also shown in Figures 4.10 and 4.11. For the hydrophobic CNTs in water, higher density peaks of water layers than the bulk water density can be seen in the density profile.<sup>22</sup> Two layers of solvation (with elevated densities) can be identified from the plots at 0.75 nm and 1.05 nm for BC-I, and similar positions correspond to the C-I model. The interactions between these layers correspond to the repulsion and attraction features on the PMF plots. For example, the first peak-to-valley of B-doped and pristine CNT around 1.4 nm to 1.5 nm COM distance correspond to the first hydration shell, as well as the second peak-to-valley corresponds to the low density areas between first and second hydration shell.

The water-nanotube interaction can also be interpreted by calculating the PMF of a single water molecule and the CNT using following equation:

$$\Delta A_{PMF}(r) = -k_B T \ln \frac{\rho(r)}{\rho_{Bulk}} \quad (3)$$

In this equation,  $k_B$  is the Boltzmann constant, T is the temperature in Kelvin,  $\rho(r)$  is the density of water in specific position, and  $\rho_{Bulk}$  is the density of bulk water (about 33 water molecules per nm<sup>3</sup>). The radial water PMF vs. water-CNT distance plots are shown in Figure 4.12, and the average number of the hydrogen bonds are shown in Figure C10. Generally speaking, the PMFs of water show comparable features and magnitudes with both B-doped and pristine CNTs (with different diameters and doping patterns), and this confirms that the hydration environments surrounding the B-doped and pristine CNTs are similar. This point can be further evaluated by following the average number of hydrogen-bond per water molecule (details provided in the Supporting Information). A decreased number of hydrogen-bonds per water molecule compared

to the bulk water (a value of about 3.6 in our simulation) at the first and second water layers are found, which indicates a vapor-liquid like interface between the nanotubes and water. These results are in good agreement with Li et al.'s results of pristine nanocarbons.<sup>52</sup> No significant difference is found between the B-doped and pristine nanotubes except for the B-CNTs with larger diameters like BC-III and BC-IV. The effects of the surface curvature dominate the first solvation layer, where fewer hydrogen bonds are found near the surface. These differences are in good agreement with the observations on pristine CNT.<sup>52</sup>

#### **4.4 Conclusions**

In summary, we have conducted a systematic investigation of the solvation behavior of B-doped CNTs. Our B-CNT simulation models have varying diameters and doping patterns, and the intertubular interactions are refined with DDEC and CHELPG derived partial charges. Our benchmarks show that the CHELPG charges derived from the cluster models are in good agreement with the DDEC charges derived from a periodic system. In our MD simulations, the repulsion of B-CNTs is moderately increased (more with the three B-CNTs in a bundle), and there is a prolonged interaction distance, as compared to pristine CNTs. The intertubular interactions of B-CNTs are fitted to the LJ and Stockmayer intermolecular potential functions for future coarse-grain simulations.

It is found that the magnitudes of repulsion and attraction peaks on the PMF plots of B-CNT in water increase with respect to the diameter of the B-CNT. On the other hand, the properties of the B-CNT(6,6) model indicates an insensitivity to the doping pattern. In addition, the hysteresis analysis of compression also revealed a more intense repulsion to compression of B-CNTs bundle than pristine bundles. However, it is recognized that the enhanced dispersion predicted by

our MD simulations is not as directly obvious in experimental systems. Due to the fact that the experimental techniques for synthesizing B-CNT (like using  $B_2O_3$  as the boron source) often introduce O impurities into the B-CNT and form hydrophilic OH groups,<sup>19, 57, 58</sup> these other functionalities will also contribute to the dispersion of B-CNTs. Due to the increased repulsion of B-CNTs in the larger bundles and significant reagglomeration resistance, substitutional boron doping is predicted to be an effective strategy for enhancing the dispersion of CNTs in aqueous environments.

### **Acknowledgments**

This work was supported by the NSF CAREER Award (no. 0747690). Supercomputer resources were provided by the Alabama Supercomputer Center.

**Supporting Information Available:** Table of DDEC and CHELPG charges. Figures of the parameterization of BC-II, BC-III and BC-IV pairs in vacuum; decomposed contributions of Coulomb and LJ interactions of the PMFs of solvated BC-II, BC-III, BC-IV pairs; benchmarks of solvated BC-I pairs PMFs with DDEC and CHELPG calculated partial charges. This material is available in Appendix C.

## References

- (1) Iijima, S.; Ichihashi, T. Single-shell Carbon Nanotubes of 1-nm Diameter. *Nature* **1993**, *363*, 603-605.
- (2) Coleman, J. N.; Khan, U.; Blau, W. J.; Gun'ko, Y. K. Small But Strong: A Review of the Mechanical Properties of Carbon Nanotube-Polymer Composites. *Carbon* **2006**, *44*, 1624-1652.
- (3) Park, S.; Vosguerichian, M.; Bao, Z. A. A Review of Fabrication and Applications of Carbon Nanotube Film-Based Flexible Electronics. *Nanoscale* **2013**, *5*, 1727-1752.
- (4) Henrard, L.; Hernandez, E.; Bernier, P.; Rubio, A. Van der Waals Interaction in Nanotube Bundles: Consequences on Vibrational Modes. *Phys. Rev. B* **1999**, *60*, 8521-8524.
- (5) Islam, M. F.; Rojas, E.; Bergey, D. M.; Johnson, A. T.; Yodh, A. G. High Weight Fraction Surfactant Solubilization of Single-Wall Carbon Nanotubes in Water. *Nano Lett.* **2003**, *3*, 269-273.
- (6) Moore, V. C.; Strano, M. S.; Haroz, E. H.; Hauge, R. H.; Smalley, R. E.; Schmidt, J.; Talmon, Y. Individually Suspended Single-Walled Carbon Nanotubes in Various Surfactants. *Nano Lett.* **2003**, *3*, 1379-1382.
- (7) Arnold, M. S.; Green, A. A.; Hulvat, J. F.; Stupp, S. I.; Hersam, M. C. Sorting Carbon Nanotubes by Electronic Structure Using Density Differentiation. *Nat. Nanotechnol.* **2006**, *1*, 60-65.
- (8) Hu, C. G.; Chen, Z. L.; Shen, A. G.; Shen, X. C.; Li, H.; Hu, S. S. Water-Soluble Single-Walled Carbon Nanotubes via Noncovalent Functionalization by A Rigid, Planar And Conjugated Diazo Dye. *Carbon* **2006**, *44*, 428-434.
- (9) O'Connell, M. J.; Boul, P.; Ericson, L. M.; Huffman, C.; Wang, Y. H.; Haroz, E.; Kuper, C.; Tour, J.; Ausman, K. D.; Smalley, R. E. Reversible Water-Solubilization of Single-Walled Carbon Nanotubes by Polymer Wrapping. *Chem. Phys. Lett.* **2001**, *342*, 265-271.
- (10) Di Crescenzo, A.; Cambré, S.; Germani, R.; Di Profio, P.; Fontana, A. Dispersion of SWCNTs with Imidazolium-Rich Surfactants. *Langmuir* **2014**, *30*, 3979-3987.
- (11) Nakashima, N.; Okuzono, S.; Murakami, H.; Nakai, T.; Yoshikawa, K. DNA Dissolves Single-Walled Carbon Nanotubes in Water. *Chem. Lett.* **2003**, *32*, 456-457.
- (12) Blackburn, J. L.; Engtrakul, C.; McDonald, T. J.; Dillon, A. C.; Heben, M. J. Effects of Surfactant And Boron Doping on The BWF Feature in The Raman Spectrum of Single-Wall Carbon Nanotube Aqueous Dispersions. *J. Phys. Chem. B* **2006**, *110*, 25551-25558.
- (13) An, W.; Turner, C. H. Chemisorption of Transition-Metal Atoms on Boron- and Nitrogen-Doped Carbon Nanotubes: Energetics and Geometric and Electronic Structures. *J. Phys. Chem. C* **2009**, *113*, 7069-7078.

- (14) An, W.; Turner, C. H. Structural, Electronic, and Magnetic Features of Platinum Alloy Strings Templated on A Boron-Doped Carbon Nanotube. *Phys. Rev. B* **2010**, *81*, 205433.
- (15) An, W.; Turner, C. H. Transition-Metal Strings Templated on Boron-Doped Carbon Nanotubes: A DFT Investigation. *J. Phys. Chem. C* **2009**, *113*, 15346-15354.
- (16) Zhang, Z. T.; Turner, C. H. Structural and Electronic Properties of Carbon Nanotubes and Graphenes Functionalized with Cyclopentadienyl-Transition Metal Complexes: A DFT Study. *J. Phys. Chem. C* **2013**, *117*, 8758-8766.
- (17) Acharya, C. K.; Turner, C. H. Stabilization of Platinum Clusters by Substitutional Boron Dopants in Carbon Supports. *J. Phys. Chem. B* **2006**, *110*, 17706-17710.
- (18) Acharya, C. K.; Sullivan, D. I.; Turner, C. H. Characterizing the Interaction of Pt And PtRu Clusters with Boron-Doped, Nitrogen-Doped, and Activated Carbon: Density Functional Theory Calculations and Parameterization. *J. Phys. Chem. C* **2008**, *112*, 13607-13622.
- (19) Acharya, C. K.; Li, W.; Liu, Z. F.; Kwon, G.; Turner, C. H.; Lane, A. M.; Nikles, D.; Klein, T.; Weaver, M. Effect of Boron Doping in the Carbon Support on Platinum Nanoparticles and Carbon Corrosion. *J. Power Sources* **2009**, *192*, 324-329.
- (20) Tummala, N. R.; Striolo, A. SDS Surfactants on Carbon Nanotubes: Aggregate Morphology. *ACS Nano* **2009**, *3*, 595-602.
- (21) Tummala, N. R.; Morrow, B. H.; Resasco, D. E.; Striolo, A. Stabilization of Aqueous Carbon Nanotube Dispersions Using Surfactants: Insights from Molecular Dynamics Simulations. *ACS Nano* **2010**, *4*, 7193-7204.
- (22) Walther, J. H.; Jaffe, R. L.; Kotsalis, E. M.; Werder, T.; Halicioglu, T.; Koumoutsakos, P. Hydrophobic Hydration of C-60 and Carbon Nanotubes in Water. *Carbon* **2004**, *42*, 1185-1194.
- (23) Groves, M. N.; Malardier-Jugroot, C.; Jugroot, M. Improving Platinum Catalyst Durability with a Doped Graphene Support. *J. Phys. Chem. C* **2012**, *116*, 10548-10556.
- (24) Won, C. Y.; Aluru, N. R. Structure and Dynamics of Water Confined in a Boron Nitride Nanotube. *J. Phys. Chem. C* **2008**, *112*, 1812-1818.
- (25) Breneman, C. M.; Wiberg, K. B. Determining Atom-centered Monopoles from Molecular Electrostatic Potentials - the Need for High Sampling Density in Formamide Conformational-analysis. *J. Comput. Chem.* **1990**, *11*, 361-373.
- (26) Won, C. Y.; Aluru, N. R. Water Permeation through a Subnanometer Boron Nitride Nanotube. *J. Am. Chem. Soc.* **2007**, *129*, 2748-2749.
- (27) Campana, C.; Mussard, B.; Woo, T. K. Electrostatic Potential Derived Atomic Charges for Periodic Systems Using a Modified Error Functional. *J. Chem. Theory Comput.* **2009**, *5*, 2866-2878.

- (28) Chen, D. L.; Stern, A. C.; Space, B.; Johnson, J. K. Atomic Charges Derived from Electrostatic Potentials for Molecular and Periodic Systems. *J. Phys. Chem. A* **2010**, *114*, 10225-10233.
- (29) Manz, T. A.; Sholl, D. S. Chemically Meaningful Atomic Charges That Reproduce the Electrostatic Potential in Periodic and Nonperiodic Materials. *J. Chem. Theory Comput.* **2010**, *6*, 2455-2468.
- (30) Manz, T. A.; Sholl, D. S. Improved Atoms-in-Molecule Charge Partitioning Functional for Simultaneously Reproducing the Electrostatic Potential and Chemical States in Periodic and Nonperiodic Materials. *J. Chem. Theory Comput.* **2012**, *8*, 2844-2867.
- (31) Allen, M. P.; Tildesley, D. J. *Computer Simulation of Liquids*. Oxford University Press: Oxford: 1989.
- (32) Stockmayer, W. H. Second Virial Coefficients of Polar Gases. *J. Chem. Phys.* **1941**, *9*, 398.
- (33) Kresse, G.; Furthmüller, J. Efficiency of Ab-initio Total Energy Calculations for Metals and Semiconductors Using a Plane-Wave Basis Set. *Comput. Mater. Sci.* **1996**, *6*, 15-50.
- (34) Hobbs, D.; Kresse, G.; Hafner, J. Fully Unconstrained Noncollinear Magnetism within the Projector Augmented-wave Method. *Phys. Rev. B* **2000**, *62*, 11556-11570.
- (35) Borowiak-Palen, E.; Rummeli, M.; Gemming, T.; Knupfer, M.; Kalenczuk, R. J.; Pichler, T. Formation of Novel Nanostructures Using Carbon Nanotubes as a Frame. *Synt. Met.* **2005**, *153*, 345-348.
- (36) Luo, X. Y.; Yang, J. H.; Liu, H. Y.; Wu, X. J.; Wang, Y. C.; Ma, Y. M.; Wei, S. H.; Gong, X. G.; Xiang, H. J. Predicting Two-Dimensional Boron-Carbon Compounds by the Global Optimization Method. *J. Am. Chem. Soc.* **2011**, *133*, 16285-16290
- (37) Yanagisawa, H.; Tanaka, T.; Ishida, Y.; Matsue, M.; Rokuta, E.; Otani, S.; Oshima, C. Phonon Dispersion Curves of a BC3 Honeycomb Epitaxial Sheet. *Phys. Rev. Lett.* **2004**, *93*, 177003.
- (38) Perdew, J. P.; Burke, K.; Ernzerhof, M. Generalized Gradient Approximation Made Simple. *Phys. Rev. Lett.* **1996**, *77*, 3865-3868.
- (39) Blochl, P. E.; Jepsen, O.; Andersen, O. K. Improved Tetrahedron Method for Brillouin-Zone Integrations. *Phys. Rev. B* **1994**, *49*, 16223-16233.
- (40) Monkhorst, H. J.; Pack, J. D. Special Points for Brillouin-Zone Integrations. *Phys. Rev. B* **1976**, *13*, 5188-5192.
- (41) Methfessel, M.; Paxton, A. T. High-precision Sampling for Brillouin-zone Integration in Metals. *Phys. Rev. B* **1989**, *40*, 3616-3621.
- (42) Frisch, M. J.; Trucks, G. W.; Schlegel, H. B.; Scuseria, G. E.; Robb, M. A.; Cheeseman, J.

- R.; Scalmani, G.; Barone, V.; Mennucci, B.; Petersson, G. A. et al. Gaussian 09, Revision B.01. Wallingford CT, 2009.
- (43) Hess, B.; Kutzner, C.; van der Spoel, D.; Lindahl, E. GROMACS 4: Algorithms for Highly Efficient, Load-Balanced, and Scalable Molecular Simulation. *J. Chem. Theory Comput.* **2008**, *4*, 435-447.
- (44) Kang, J. W.; Hwang, H. J. Comparison Of C-60 Encapsulations into Carbon and Boron Nitride Nanotubes. *J. Phys.: Condens. Matter* **2004**, *16*, 3901-3908.
- (45) Won, C. Y.; Aluru, N. R. Water Phase Transition Induced by a Stone-Wales Defect in a Boron Nitride Nanotube. *J. Am. Chem. Soc.* **2008**, *130*, 13649-13652.
- (46) Berendsen, H. J. C.; Grigera, J. R.; Straatsma, T. P. The Missing Term in Effective Pair Potentials. *J. Phys. Chem.* **1987**, *91*, 6269-6271.
- (47) Won, C. Y.; Joseph, S.; Aluru, N. R. Effect of Quantum Partial Charges on the Structure and Dynamics of Water in Single-Walled Carbon Nanotubes. *J. Chem. Phys.* **2006**, *125*, 114701.
- (48) Miyamoto, S.; Kollman, P. A. SETTLE - an Analytical Version of the SHAKE and RATTLE Algorithm for Rigid Water Models. *J. Comput. Chem.* **1992**, *13*, 952-962.
- (49) Essmann, U.; Perera, L.; Berkowitz, M. L.; Darden, T.; Lee, H.; Pedersen, L. G. A Smooth Particle Mesh Ewald Method. *J. Chem. Phys.* **1995**, *103*, 8577-8593.
- (50) Hoover, W. G. Canonical Dynamics - Equilibrium Phase-space Distributions. *Phys. Rev. A* **1985**, *31*, 1695-1697.
- (51) van der Spoel, D.; van Maaren, P. J.; Berendsen, H. J. C. A Systematic Study of Water Models for Molecular Simulation: Derivation of Water Models Optimized for Use with A Reaction Field. *J. Chem. Phys.* **1998**, *108*, 10220-10230.
- (52) Li, L. W.; Bedrov, D.; Smith, G. D. Water-Induced Interactions between Carbon Nanoparticles. *J. Phys. Chem. B* **2006**, *110*, 10509-10513.
- (53) Uddin, N. M.; Capaldi, F. M.; Farouk, B. Molecular Dynamics Simulations of the Interactions and Dispersion of Carbon Nanotubes in Polyethylene Oxide/Water Systems. *Polymer* **2011**, *52*, 288-296.
- (54) Girifalco, L. A.; Hodak, M.; Lee, R. S. Carbon Nanotubes, Buckyballs, Ropes, and a Universal Graphitic Potential. *Phys. Rev. B* **2000**, *62*, 13104-13110.
- (55) Liba, O.; Kauzlaric, D.; Abrams, Z. R.; Hanein, Y.; Greiner, A.; Korvink, J. G. A Dissipative Particle Dynamics Model of Carbon Nanotubes. *Mol. Simulat.* **2008**, *34*, 737-748.
- (56) Angelikopoulos, P and Bock, H. The Nanoscale Cinderella Problem-Design of Surfactant Coatings for Carbon Nanotubes. *J. Phys. Chem. Lett.* **2011**, *2*, 139.

- (57) Golberg, D.; Bando, Y.; Han, W.; Kurashima, K.; Sato, T. Single-Walled B-Doped Carbon, B/N-Doped Carbon and BN Nanotubes Synthesized from Single-Walled Carbon Nanotubes through a Substitution Reaction. *Chem. Phys. Lett.* **1999**, *308* (3-4), 337-342; Prylutsky, Y. I. et al. *Langmuir* **2014**, *30*, 3967-3970.
- (58) Prylutsky, Y. I. et al. On the Origin of C<sub>60</sub> Fullerene Solubility in Aqueous Solution. *Langmuir* **2014**, *30*, 3967-3970.

**Table 4.1.** Simulation parameters of different B-CNT and CNT systems.

<i>System</i>	<i>Number of waters in the box</i>	<i>Box dimensions <math>x \times y \times z</math> (nm)</i>	<i>Simulation time (ns)</i>
<b>BC-I</b>			
Single nanotube	2901	$7.72 \times 4 \times 2.98$	30
Double nanotube	2864	$7.85 \times 4 \times 2.98$	2
Triple nanotube	5844	$7.85 \times 8 \times 2.98$	15
<b>BC-II</b>			
Single nanotube	2901	$7.61 \times 4 \times 2.95$	30
Double nanotube	2864	$7.85 \times 4 \times 2.95$	2
<b>BC-III</b>			
Single nanotube	6141	$7.89 \times 8 \times 3.04$	30
Double nanotube	5861	$7.83 \times 8 \times 3.04$	5
<b>BC-IV</b>			
Single nanotube	6053	$7.88 \times 8 \times 3.04$	30
Double nanotube	9316	$9.85 \times 10 \times 3.04$	5
<b>C-I</b>			
Single nanotube	2901	$7.70 \times 4 \times 2.98$	30
Double nanotube	2904	$7.85 \times 4 \times 2.98$	2
Triple nanotube	5844	$7.85 \times 8 \times 2.98$	15

**Table 4.2.** Fitted parameters for B-CNT pairs for LJ and Stockmayer potential functions. Note that the  $\epsilon$  and C parameters are normalized per nm of B-CNT length.

<i>System</i>	<i>L-J parameters</i>		<i>Stockmayer parameters</i>		
	$\sigma(\text{nm})$	$\epsilon(\text{kcal/mol/nm})$	$\sigma(\text{nm})$	$\epsilon(\text{kcal/mol/nm})$	$C(\text{kcal/mol/nm}^{-4})$
<b>BC-I</b>	0.30	16.86	0.34	3.40	0.60
<b>BC-II</b>	0.31	16.40	0.34	3.77	0.56
<b>BC-III</b>	0.30	23.81	0.34	3.28	0.87
<b>BC-IV</b>	0.29	26.21	0.34	2.82	0.93

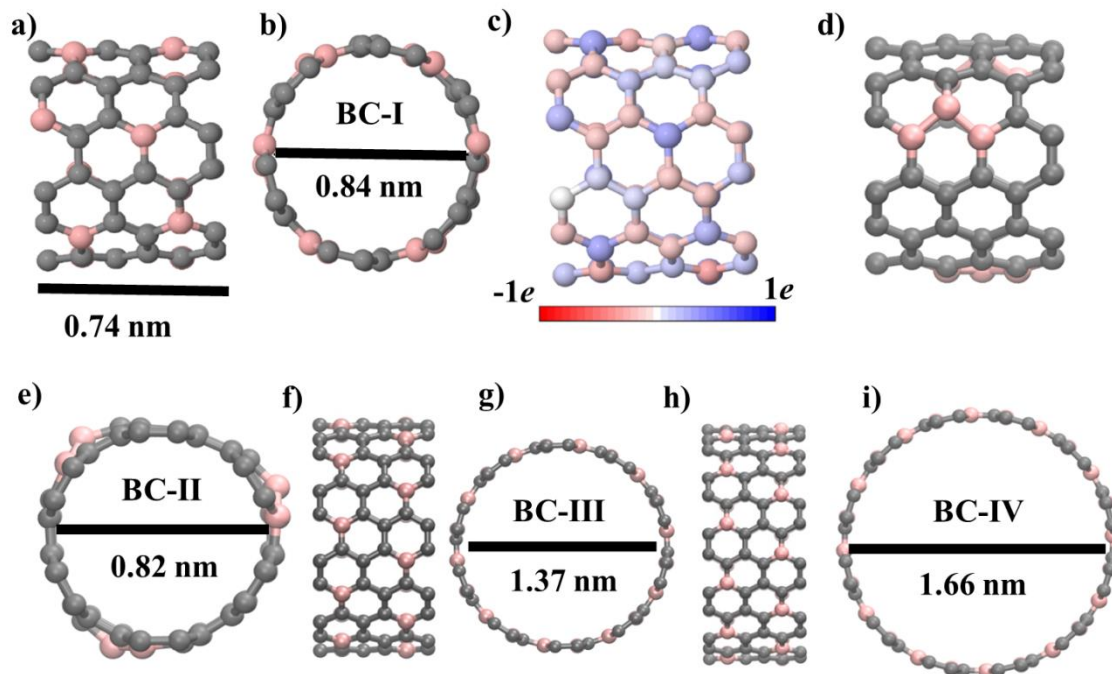


**Figure 4.1.** a) Side view and b) top view of *the* B-CNT(6,6) supercell with the BC<sub>5</sub> doping pattern (BC-I). The B and C atoms are colored pink and gray, respectively. c) DFT-calculated DDEC partial charge results. d) Side view and e) top view of the B-CNT(6,6) supercell with a B<sub>3</sub> doping pattern (BC-II). f) Side view and g) top view of B-CNT(10,10) supercell with the BC<sub>5</sub> doping pattern (BC-III). h) Side view and i) top view of B-CNT(12,12) supercell with the BC<sub>5</sub> doping pattern (BC-IV). All of the z-axis lengths of the B-CNT supercells are approximately 0.74 nm.

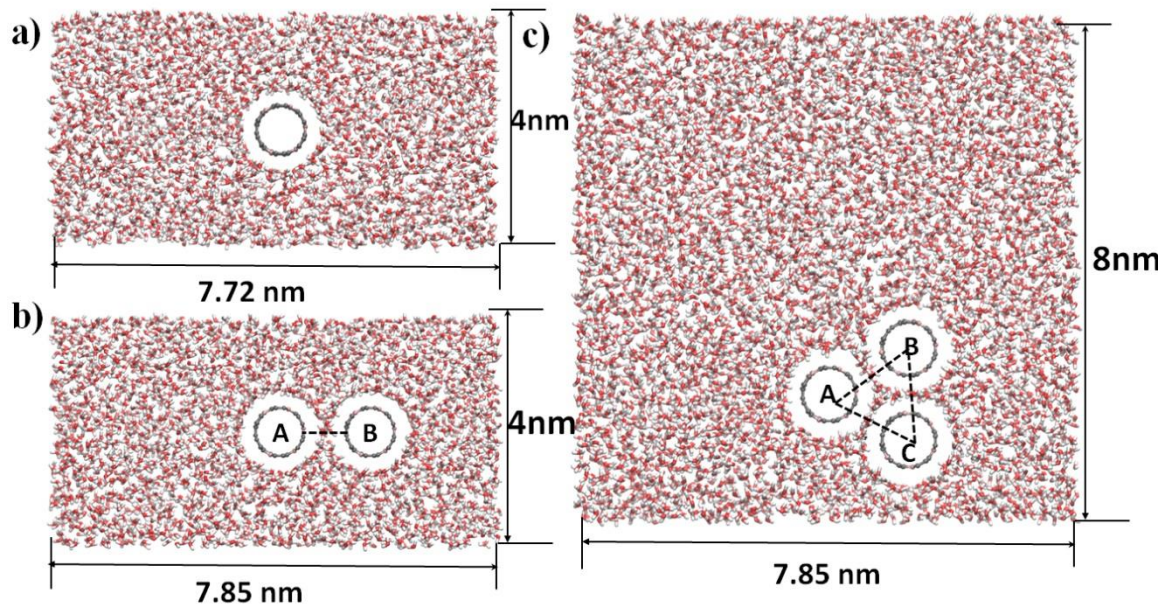


**Figure 4.2.** Simulation boxes containing (a) one B-CNT, (b) two B-CNTs and (c) three B-CNTs in a bundle, showing the dimensions of the simulation box and the arrangements of B-CNT (6,6) with the  $BC_5$  doping pattern (BC-I). The other CNTs are arranged in a similar way with slightly different box dimensions (shown in Table 4.1).

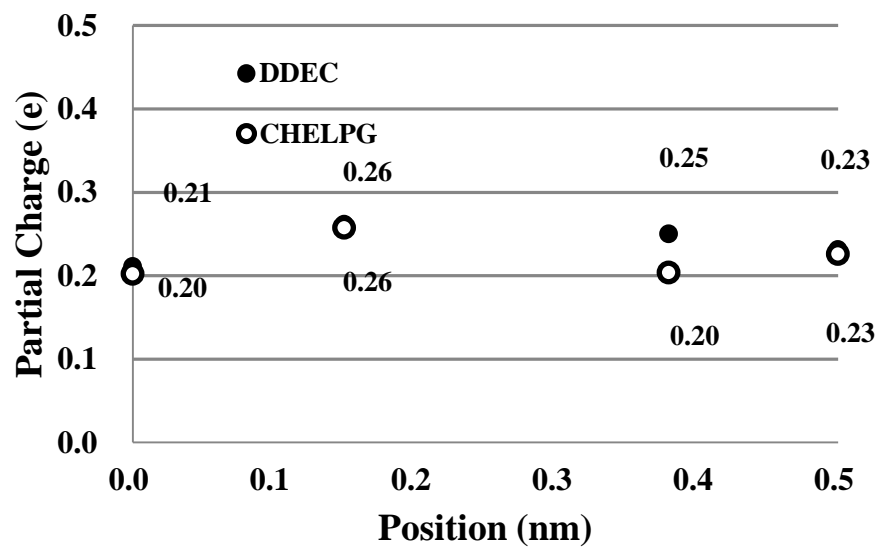


**Figure 4.3.** Partial charge distributions of the B atoms along the c-axis of the BC-I model obtain by DDEC (solid circles) and CHELPG (hollow circles).

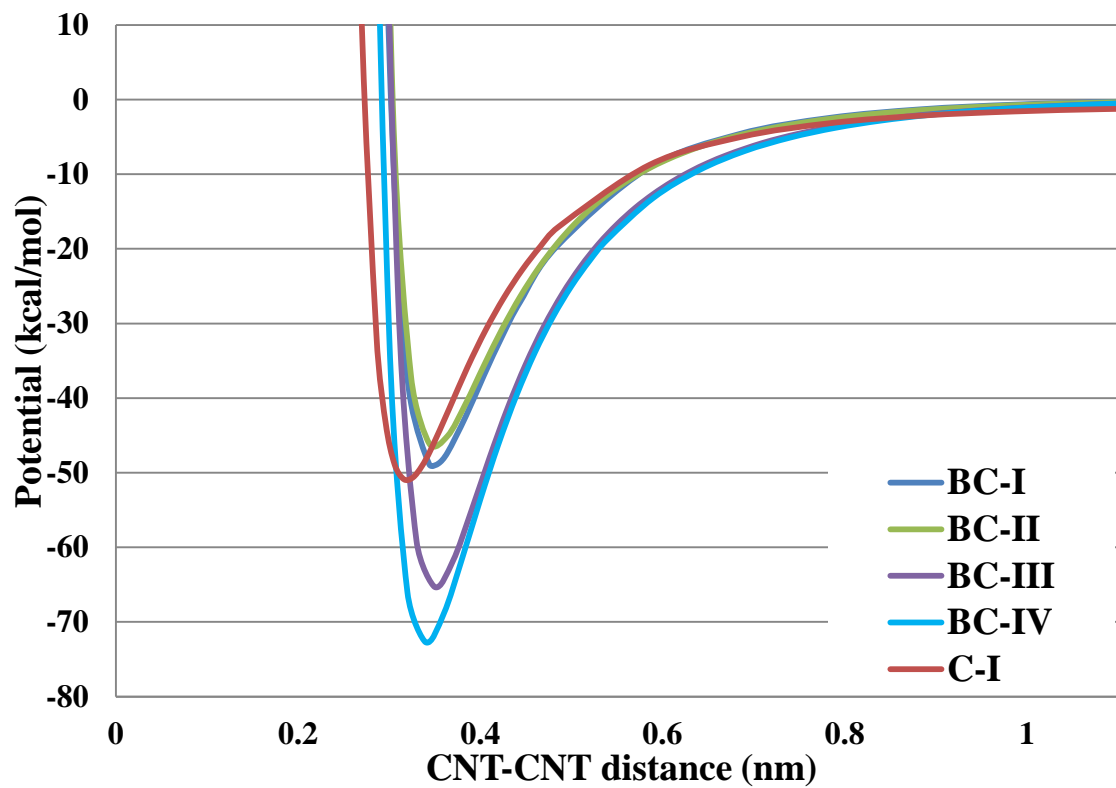


**Figure 4.4.** The calculated PMFs of nanotube pairs in vacuum from MD simulations.

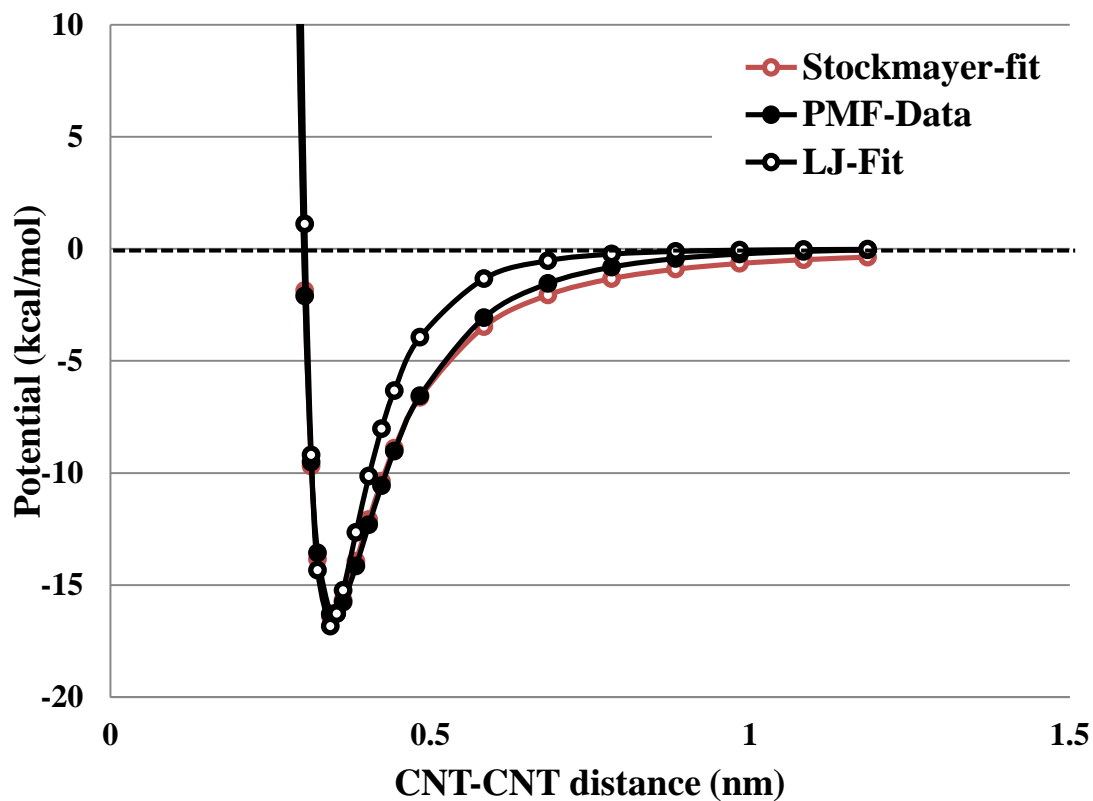


**Figure 4.5.** PMF of B-CNT(6,6) with a BC<sub>5</sub> doping pattern (BC-I) and fitted potentials, showing the PMF data (black solid circles), Stockmayer fit (red hollow circles), and LJ fit (black hollow circles). Additional potential fittings are shown in the Supporting Information.

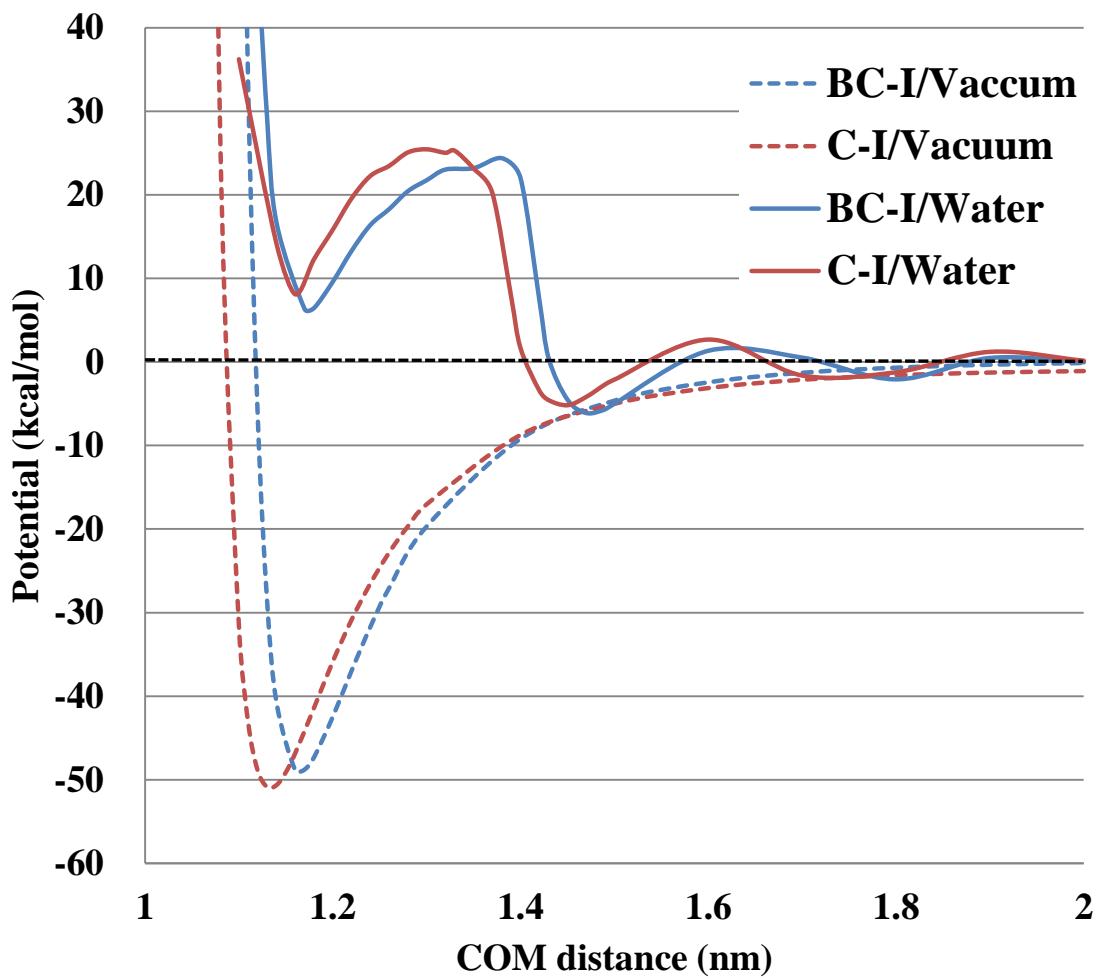


**Figure 4.6.** PMFs of B-CNT(6,6) (BC-I) and pristine CNT(6,6) (C-I) in water (solid lines) and vacuum (dashed lines) calculated from MD simulation.

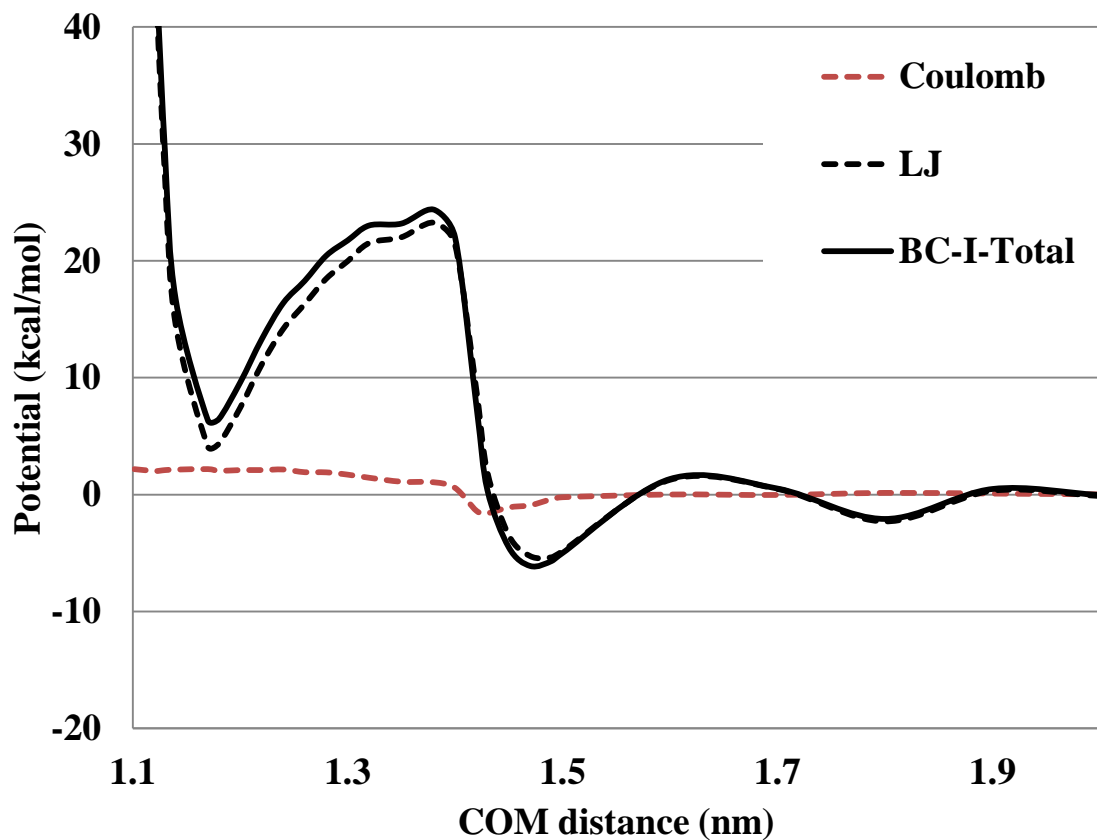


**Figure 4.7.** Total and decomposed PMFs of B-CNT(6,6) with the BC<sub>5</sub> doping pattern (BC-I), showing the total PMF (black solid line), the Coulomb contribution of PMF (red dashed line) and the LJ contribution of PMF (black dashed line).

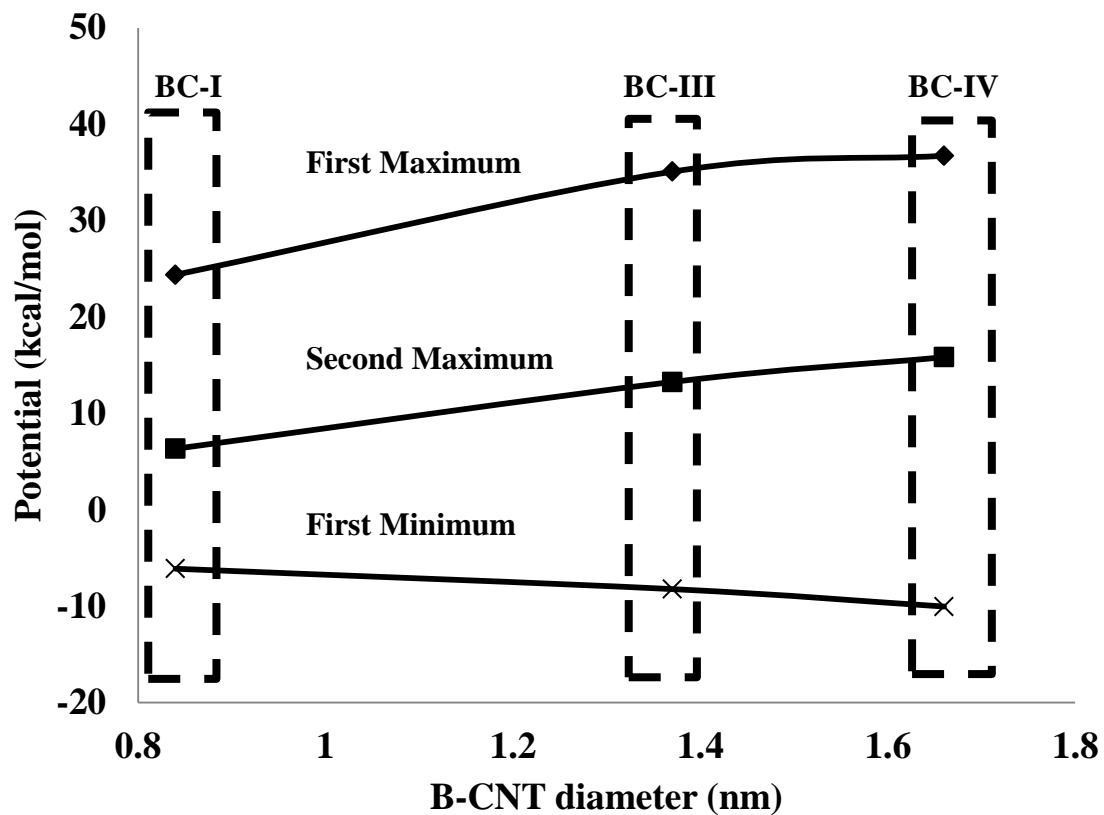


**Figure 4.8.** The trends of the PMFs' first minima, first maxima, and second minima energy vs. the tube diameter of BC-I, BC-III, and BC-IV models (with BC<sub>5</sub> doping patterns).

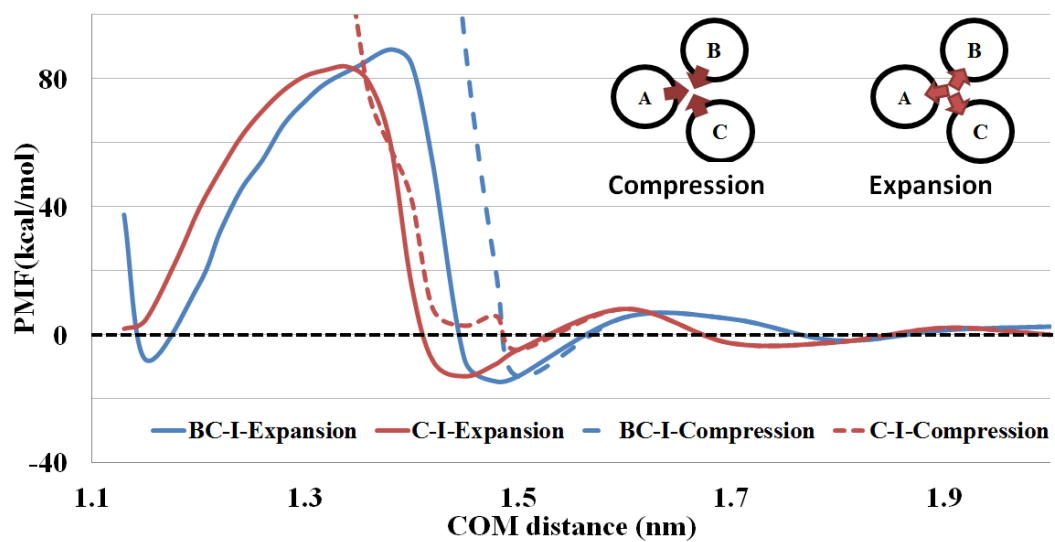


**Figure 4.9.** Illustration of hysteresis corresponding to the expansion and compression PMFs of three C-I and BC-I nanotube bundles.

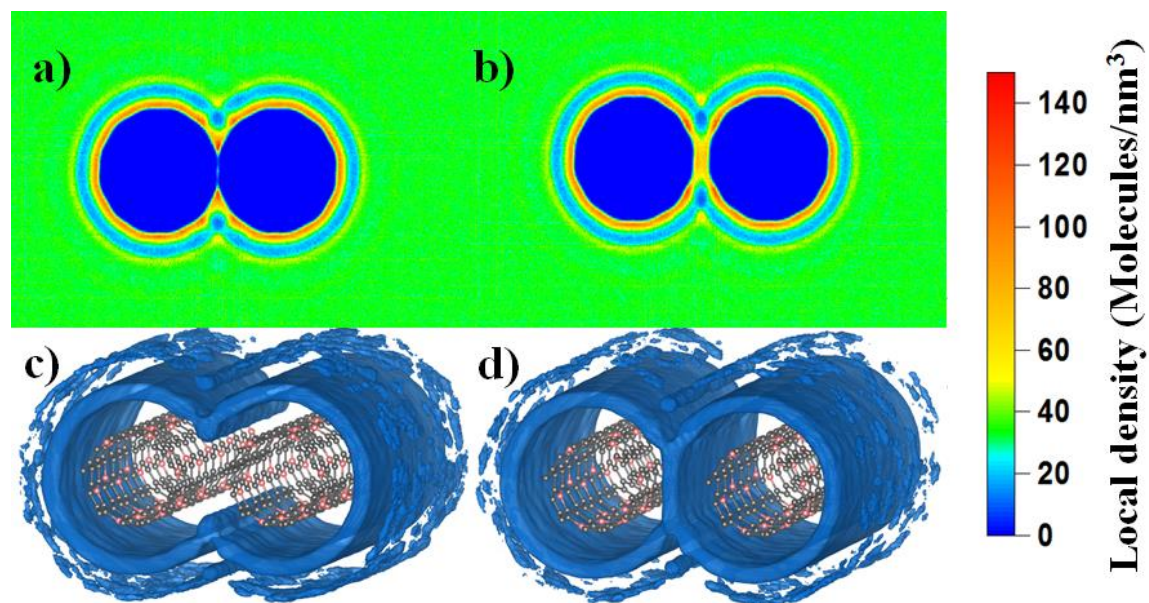


**Figure 4.10.** 2D and 3D density profiles of solvated BC-I pairs. (a) and (b) 2D density profile of water at 1.4 and 1.6 nm COM distances, respectively. Note that the number density of bulk water is around 33.4 molecules per nm<sup>3</sup>. (c) and (d) 3D density profiles of water at 1.4 and 1.6 nm COM distances, respectively. The isovalues are chosen to show the solvation layer clearly.

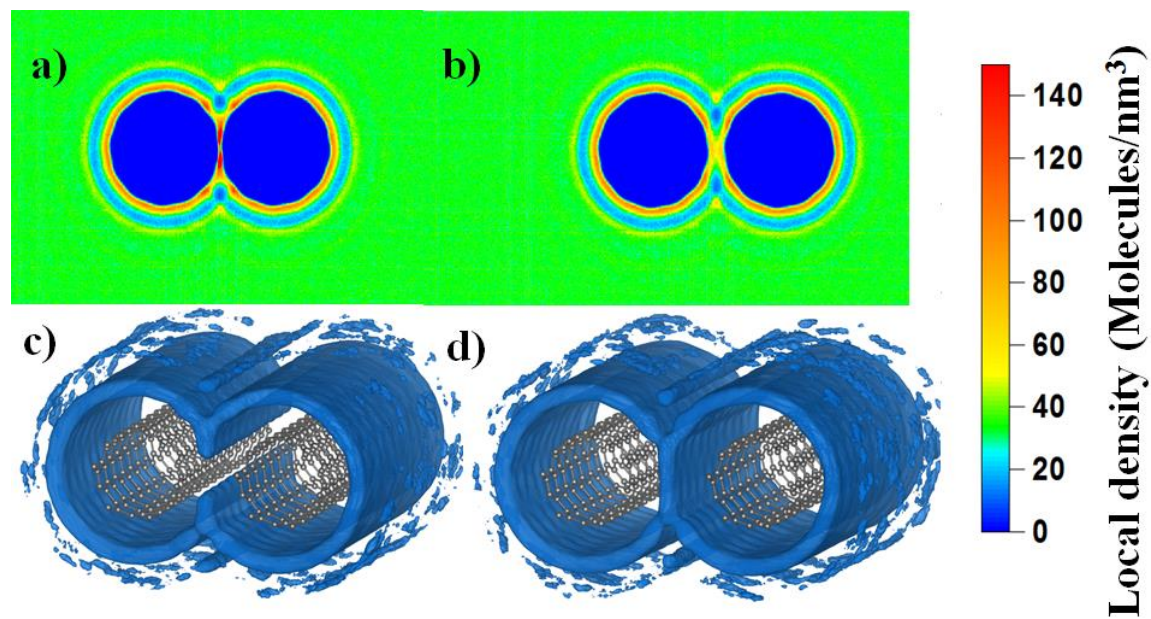


**Figure 4.11.** 2D and 3D density profile of solvated C-I pairs. (a) and (b) 2D density profiles of water at 1.4 and 1.6 nm COM distances, respectively. (c) and (d) 3D density profiles of water at 1.4 and 1.6 nm COM distances, respectively. The isovalues are chosen to show the solvation layer clearly.

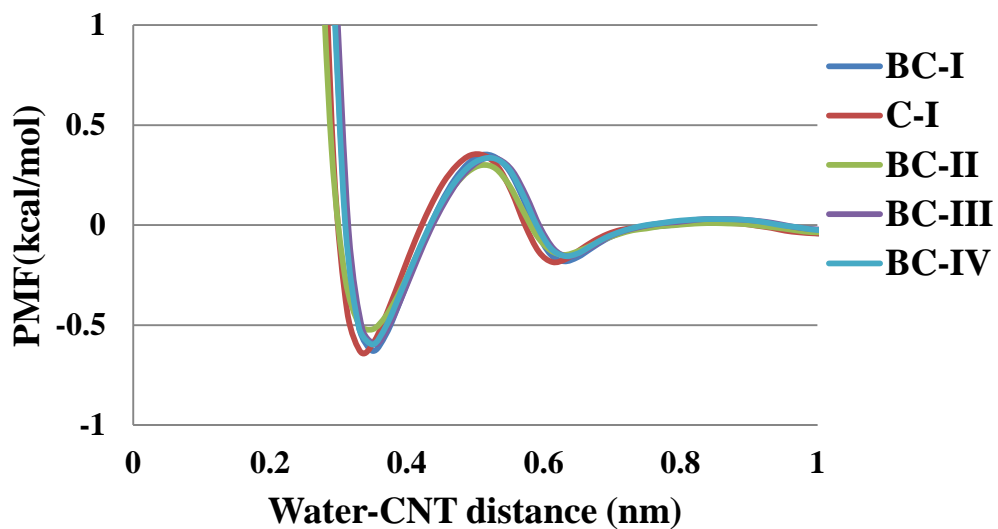


**Figure 4.12.** Radial PMF of single water molecule around pristine CNT and B-CNT. The radial water PMF were calculated from six 5 ns run of single CNT in simulation box with 166 sampling bins from 0.2 to 1.5 nm radius from the CNT surface.

Appendix C. Supporting Information for Chapter 4.

**Table C1.** Calculated geometry and partial charges of BC-I model.

Atom	Coordinates(Å)			Partial charges(e)		
	X	Y	Z	DDEC	CHELPG	CHELPG with H summed into B and C
B	9.0353	4.2915	1.3886	0.27	0.22	0.22
B	5.7614	7.0924	1.3845	0.27	0.27	0.27
B	1.6621	5.7456	1.3872	0.24	0.32	0.32
B	0.7293	2.2414	0.1522	0.21	0.48	0.20
B	4.1834	-1.2800	1.3769	0.27	0.24	0.24
B	8.2473	0.0601	1.3883	0.25	0.23	0.23
B	0.9181	1.4705	3.8414	0.25	0.20	0.20
B	9.2327	3.4859	5.0779	0.24	0.26	0.26
B	6.5804	6.8762	5.0776	0.23	0.27	0.27
B	2.3564	6.1888	5.0661	0.24	0.17	0.17
B	3.3627	-1.2078	5.0764	0.20	0.18	0.18
B	7.6209	-0.5102	5.0738	0.25	0.25	0.25
C	9.1678	3.5047	0.1260	-0.16	-0.26	-0.19
C	7.7360	6.0696	0.1478	0.10	0.16	0.18
C	8.2686	5.6200	1.3877	-0.20	-0.27	-0.27
C	3.5672	6.8855	0.1411	0.12	0.13	0.16
C	6.5173	6.8157	0.1225	-0.14	-0.27	-0.21
C	2.2814	6.2354	0.1145	-0.16	-0.32	-0.25
C	4.2249	7.1087	1.3830	-0.24	-0.27	-0.27
C	0.7094	3.7649	0.1583	-0.14	-0.10	-0.03
C	0.8838	4.4352	1.3786	-0.14	-0.21	-0.21
C	2.2013	-0.2459	0.1337	0.03	-0.22	-0.06
C	0.9863	1.4856	1.4163	-0.10	-0.18	-0.18
C	3.4243	-0.9939	0.1183	-0.12	-0.12	-0.07
C	1.7205	0.2496	1.4035	0.08	0.14	0.14
C	6.3654	-1.1088	0.1417	0.11	0.11	0.14
C	5.7126	-1.3307	1.3796	-0.22	-0.27	-0.27
C	9.1307	2.0742	0.1486	0.12	0.18	0.19
C	7.6315	-0.4432	0.1198	-0.14	-0.24	-0.17
C	9.0090	1.3887	1.3882	-0.22	-0.30	-0.30
C	9.1653	3.5056	2.6547	-0.14	-0.07	-0.07
C	8.9869	4.2451	3.8153	-0.12	-0.11	-0.11

C	7.7425	6.0722	2.6261	0.10	0.13	0.13
C	8.2936	5.4969	3.8378	0.14	0.14	0.14
C	3.5842	6.8591	2.6258	0.12	0.11	0.11
C	6.5236	6.8222	2.6486	-0.14	-0.11	-0.11
C	5.8016	7.0383	3.8091	-0.11	-0.06	-0.06
C	2.3225	6.1771	2.6529	-0.17	-0.11	-0.11
C	1.8151	5.5846	3.8075	-0.09	0.02	0.02
C	4.3712	7.0441	3.8310	0.12	0.06	0.06
C	0.8030	3.6681	2.5797	0.12	0.13	0.13
C	1.0756	4.3565	3.8230	0.05	-0.03	-0.03
C	2.1991	-0.3400	2.6377	0.09	0.11	0.11
C	0.7873	2.2384	2.5723	-0.16	-0.12	-0.12
C	3.4226	-1.0803	2.6426	-0.15	-0.07	-0.07
C	4.1382	-1.3562	3.8037	-0.12	-0.12	-0.12
C	1.6035	0.1098	3.8476	-0.12	-0.18	-0.18
C	6.3616	-1.1255	2.6261	0.11	0.06	0.06
C	5.5790	-1.3393	3.8304	0.13	0.19	0.19
C	9.1271	2.0750	2.6298	0.11	0.11	0.11
C	7.6244	-0.4482	2.6507	-0.16	0.01	0.01
C	8.1638	0.0843	3.8118	-0.12	-0.17	-0.17
C	8.9005	1.3087	3.8371	0.12	0.17	0.17
C	8.9851	4.2431	6.3439	-0.10	-0.27	-0.20
C	7.8692	6.0489	5.0775	-0.24	-0.31	-0.31
C	8.2907	5.4946	6.3191	0.13	0.18	0.21
C	3.6897	6.9395	5.0688	-0.23	-0.20	-0.20
C	5.7931	7.0394	6.3399	-0.12	-0.24	-0.19
C	1.7738	5.6604	6.3319	-0.12	-0.13	-0.09
C	4.3602	7.0572	6.3154	0.12	0.05	0.11
C	0.8778	3.6950	5.0928	0.06	-0.01	-0.01
C	1.0301	4.4390	6.3270	0.10	-0.03	0.03
C	2.0675	-0.4045	5.0679	-0.14	-0.09	-0.09
C	0.7974	2.2596	5.1055	-0.14	0.00	0.00
C	0.9680	1.4999	6.2615	-0.11	-0.13	-0.06
C	4.1477	-1.2855	6.3422	-0.12	-0.19	-0.15
C	1.6417	0.2389	6.2690	0.13	0.04	0.09
C	6.2653	-1.2337	5.0723	-0.25	-0.29	-0.29
C	5.5818	-1.3080	6.3151	0.13	0.09	0.13
C	9.1655	1.9534	5.0769	-0.23	-0.24	-0.24
C	8.1723	0.0814	6.3378	-0.12	-0.19	-0.14
C	8.9075	1.3094	6.3153	0.12	0.10	0.14

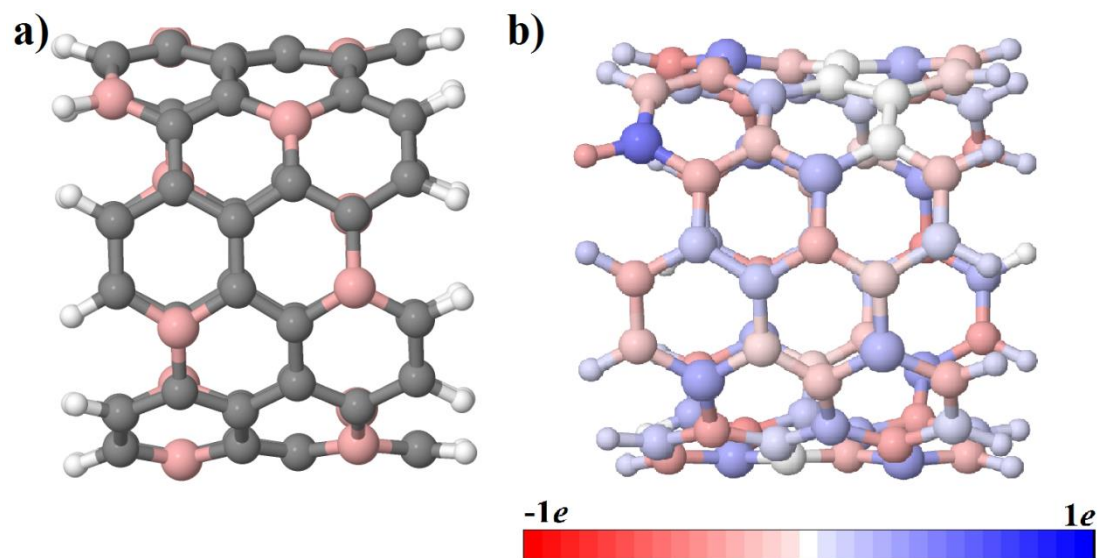


**Figure C1.** a) geometry and b) CHELPG partial charges of the cluster model of (6, 6) BC<sub>5</sub> B-CNT.

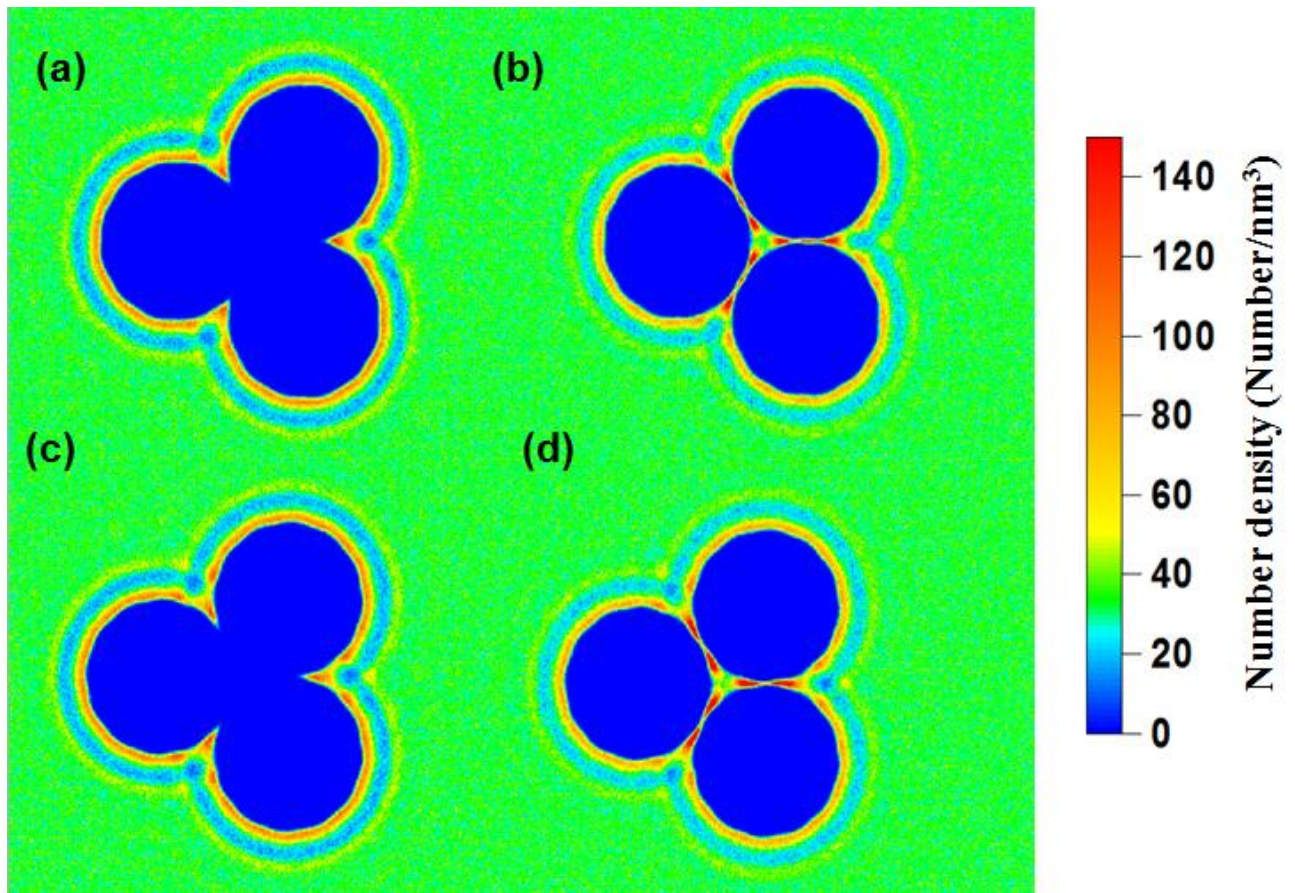


**Figure C2.** 2D density profile of three CNT bundles expansion and compression at 1.38 nm. (a) B-CNT expansion. (b) B-CNT compression. (c) CNT expansion. (d) CNT compression.

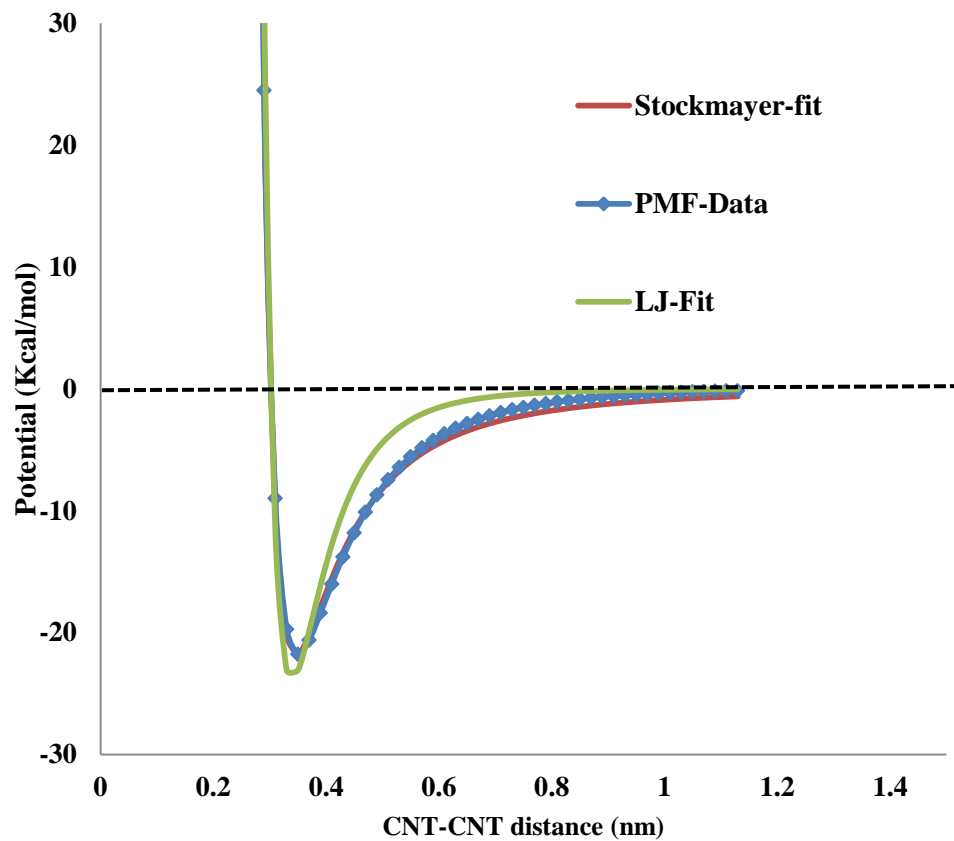


**Figure C3.** LJ and Stockmayer potential fitting of MD calculated PMFs of BC-III model (B-CNT(10,10) with BC<sub>5</sub> doping pattern).

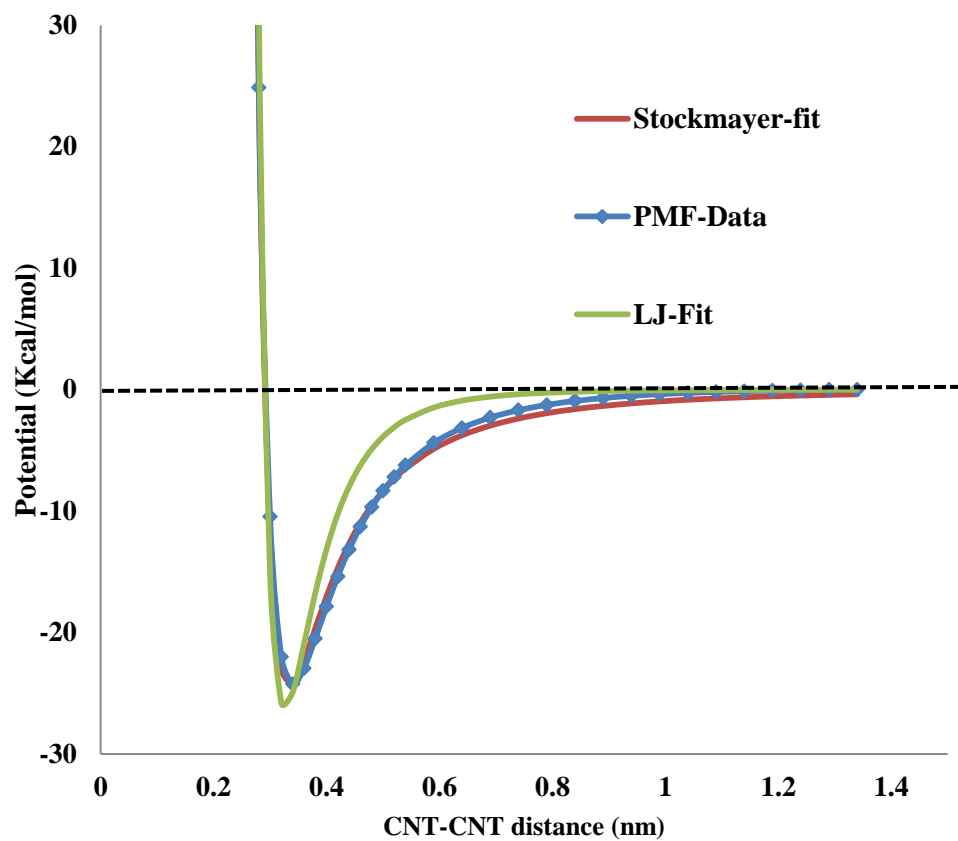


**Figure C4.** LJ and Stockmayer potential fitting of MD calculated PMFs of BC-IV model (B-CNT(12,12) with BC<sub>5</sub> doping pattern).

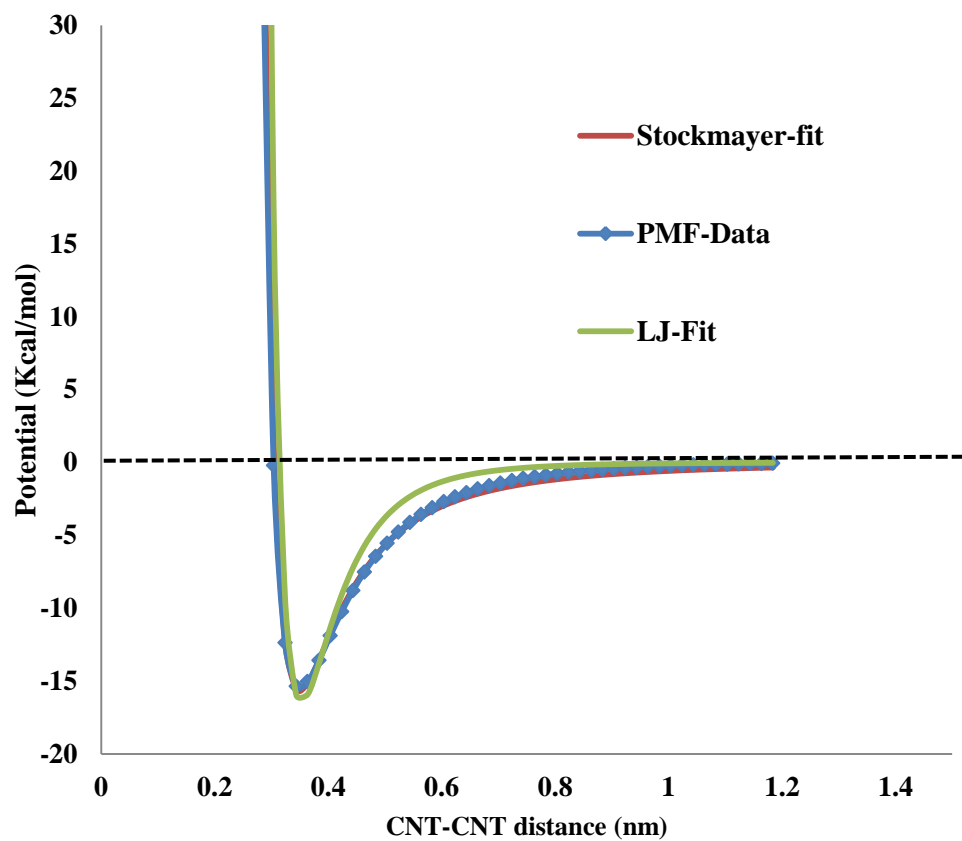


**Figure C5.** LJ and Stockmayer potential fitting of MD calculated PMFs of BC-II model (B-CNT(6,6) with B<sub>3</sub> doping pattern).

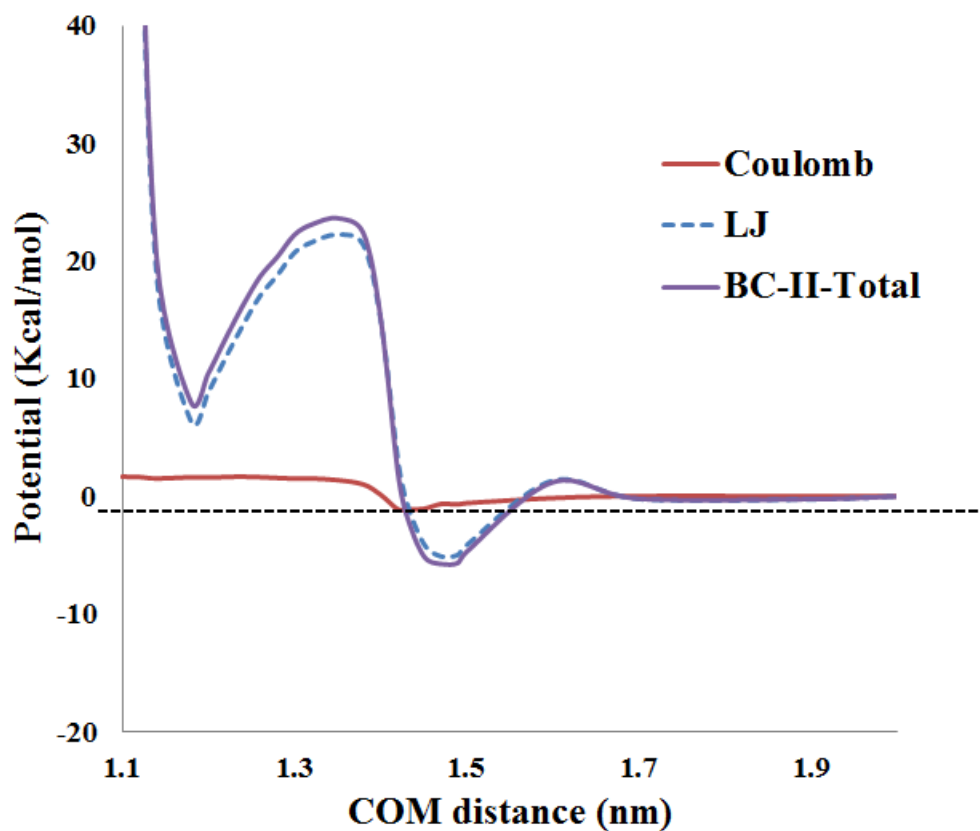


**Figure C6.** Total and decomposed PMFs of B-CNT(6,6) with B<sub>3</sub> doping pattern (BC-II), showing the total PMF(purple), the Coulomb contribution of PMF(red) and the LJ contribution of PMF(dashed blue).

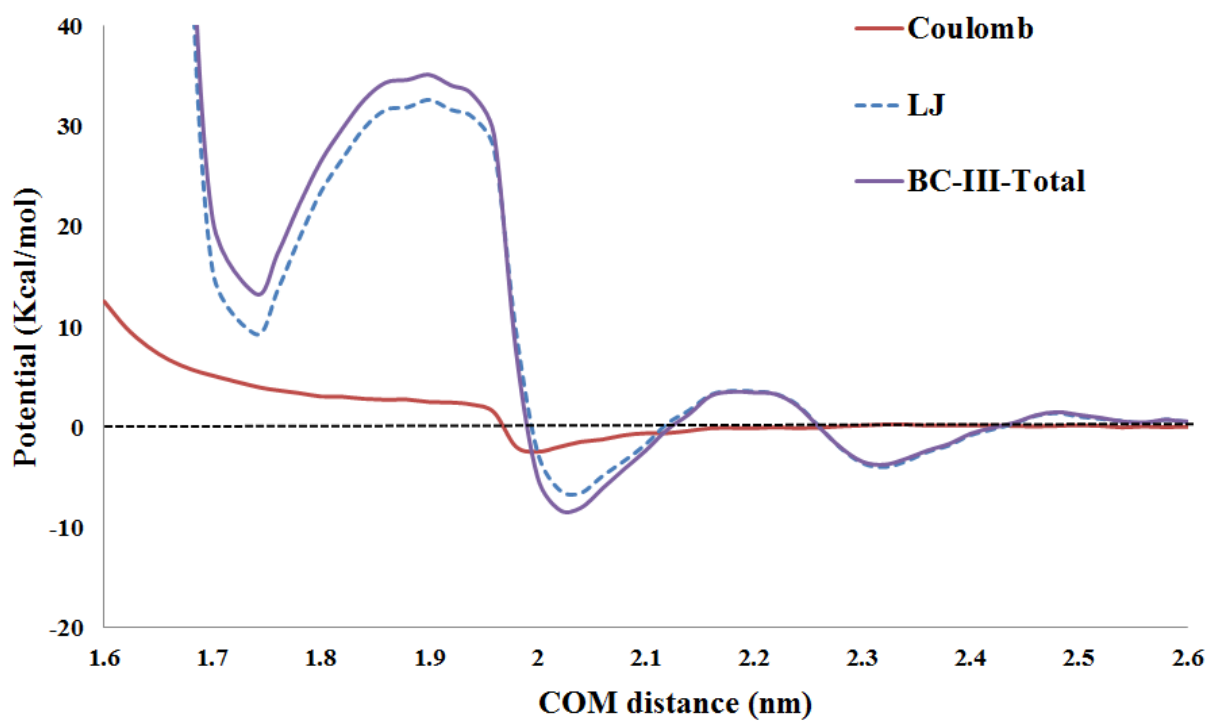


**Figure C7.** Total and decomposed PMFs of B-CNT(10,10) with BC<sub>5</sub> doping pattern (BC-III), showing the total PMF(purple), the Coulomb contribution of PMF(red) and the LJ contribution of PMF(dashed blue).

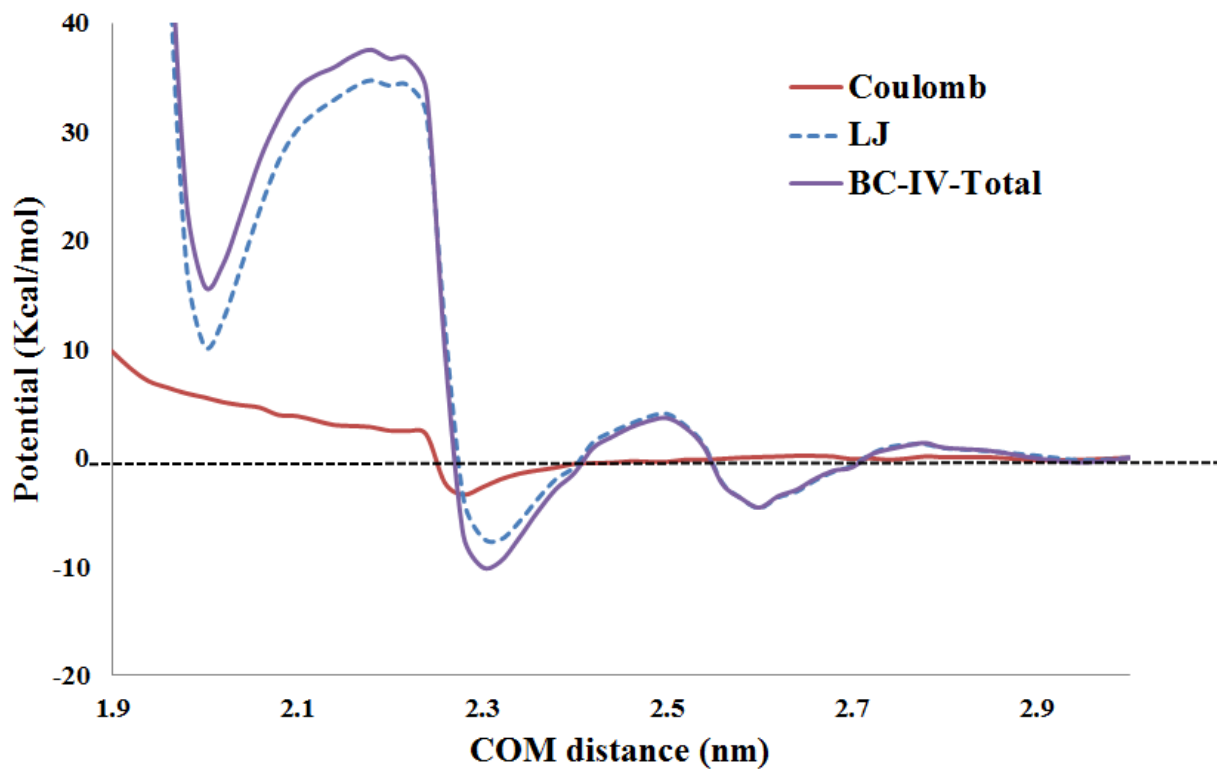


**Figure C8.** Total and decomposed PMFs of B-CNT(12,12) with BC<sub>5</sub> doping pattern (BC-IV), showing the total PMF(purple), the Coulomb contribution of PMF(red) and the LJ contribution of PMF(blue).

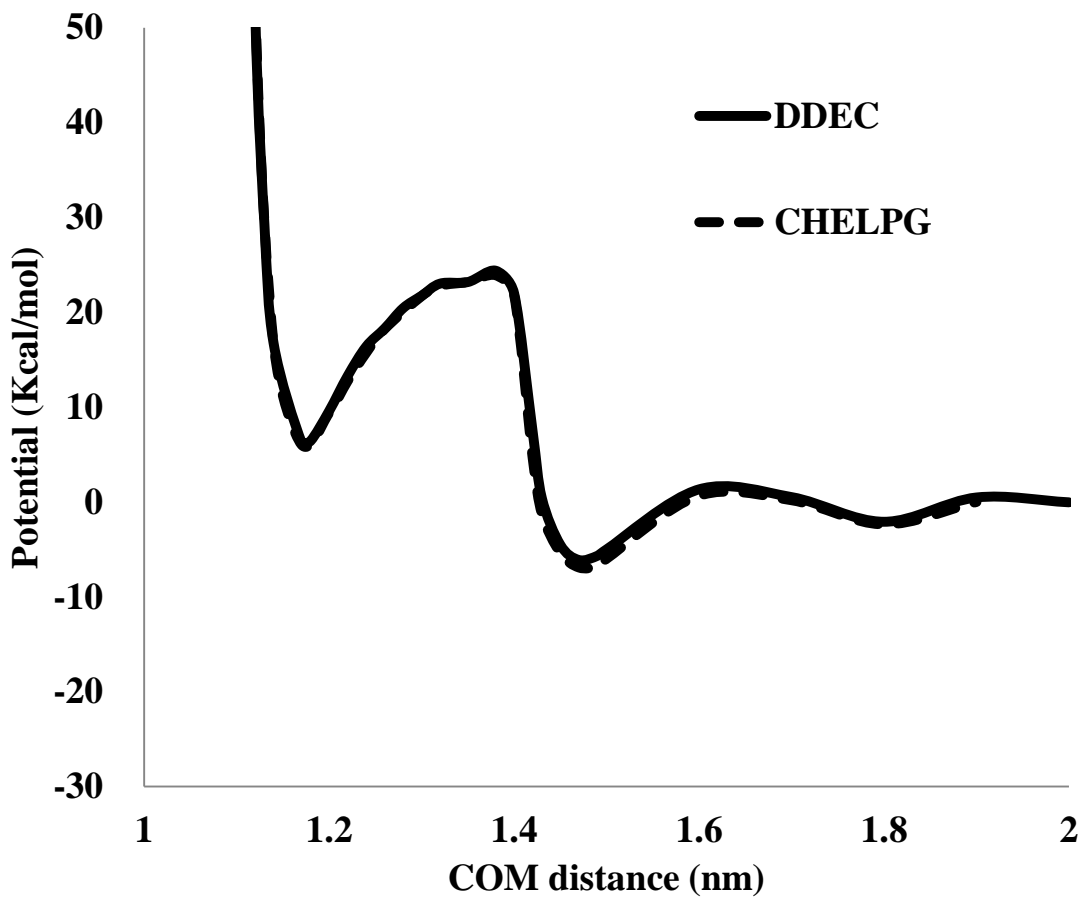


**Figure C9.** PMFs of solvated BC-I pair with DDEC and CHELPG calculated partial charges.

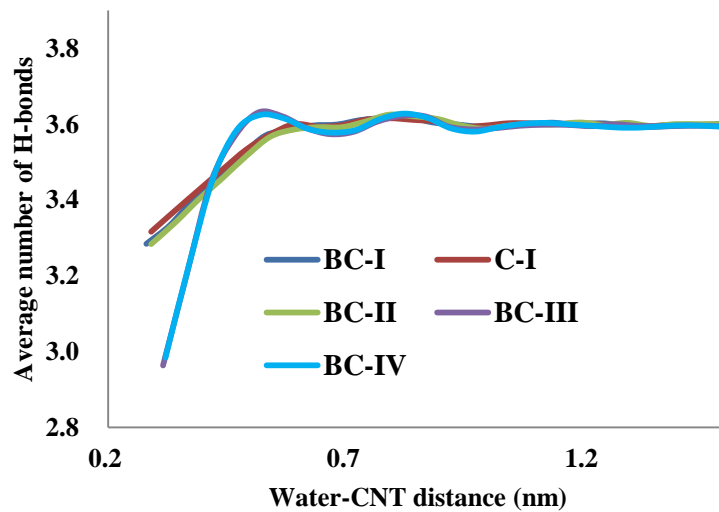


**Figure C10.** Average number of hydrogen-bond per water molecule around pristine CNT and B-CNT. The average number of hydrogen-bond per water molecule were calculated from six 5ns run of single CNT in simulation box with 50 sampling bins from 0.7 to 2.0nm radius of the CNT mass center.

## CHAPTER 5

### SUMMARY

A series of computational studies have been conducted to explore the properties of organometallic-doped nanocarbon complexes for electrochemical applications. In this work, a theoretical systematic characterization of the geometric, energetic, and electronic properties of CpTM (TM=Fe, Ni, Co, Cr, Cu) ligands adsorbed on pristine and boron-doped single-walled CNT complexes and graphenes has been conducted. Spin-polarized density functional theory calculations reveal remarkable stabilization of the CpTM adsorbed on the boron-doped nanocarbon support. The binding energies between CpTM and boron-doped CNTs and graphenes have been found to surpass the adsorption strength of the isolated metal atoms by approximately 2 eV, which is often considered to be the upper limit of the binding energy. Thus, the exceptional stability of CpTM/B-doped nanocarbon is predicted to provide a solid foundation for immobilizing ferrocene-based active centers for electrochemical systems.

In addition to the binding energies, our electronic structure analyses indicate that the interactions between the  $2p$ -states of B and C and the  $d$ -states of the TM, as well as the  $\pi$ -stacking interactions between the Cp ring and the carbon supports contribute to the stability. Moreover, tunable metallicities of these complexes are predicted to arise from different CpTM ligands, and this behavior indicates potential applications in nanoelectronics and sensing. In addition, the adsorption of O<sub>2</sub> molecules on CpFe/B-doped CNT was studied as a preliminary indicator of catalytic performance. Both chemisorption (with an elongated O-O bond) and dissociative chemisorption were found on CpFe/B-CNT (8,0) complexes, and possible pathways

were revealed with AIMD calculations

The redox properties of CpTM on B-doped, N-doped, and pristine graphene complexes were studied with DFT calculations (combined with the CPCM implicit solvation model) to probe the potential applications of these complexes as redox-active materials. Complexes with different transition metal cores, Cp sidechains, and doped graphene supports were benchmarked by evaluating their redox properties in different solution environments, including water and acetonitrile. Most of the materials were not viable substitutes for ferrocene. However, the redox potential of CpFe/BGr was found to be comparable to the ferrocene molecule and its derivatives, which implies the possibility of using these complexes to function within ferrocene-based electrochemical systems. Also, the redox potentials of CpFe/BGr were found to be insensitive to the B-doping concentrations (from 3% to 16%) or patterns (single atom vs. BC5). In addition, using the deformation charge densities, frontier orbitals, and NBO population analyses, the charge transfer mechanism during the redox process showed large charge redistributions. These charge redistributions were found to be relevant to the redox properties. In addition, the bonding between the TM centers and the supports are transformed into a more ionic interaction, which enhances the binding between the CpTM complexes and graphene supports.

In addition, MD simulations were used to investigate the hydration, the water-induced interactions, and the dispersion behavior of boron-doped single-walled carbon nanotubes (B-CNTs) within aqueous solutions. Models of B-CNTs with varying diameters and B-doping patterns were used in our simulation. Moreover, coarse-grain models of B-CNT intertubular interactions were parameterized to fit the LJ and Stockmayer style potential functions for future simulations at a larger scale. A moderate increase of the repulsion and prolonged interaction distances were found when comparing B-CNTs to pristine CNTs. Moreover, the PMF of the 3B-

CNTs bundle demonstrated that the repulsion between B-CNTs increased with respect to the number of B-CNTs in the bundle. As in other calculations, the hydration properties were insensitive to the doping pattern or doping concentration. In addition, the hysteresis analysis of compression indicated that the B-CNT bundle was more aggregation resistant than a CNT pristine bundle. However, in experiments, oxygen impurities within the B-CNT may also play a role in the enhanced dispersion of B-CNTs.

To summarize, our studies provide strong evidence that the Cp<sup>TM</sup>/doped nanocarbon complexes are exceptionally stable materials, which possess intriguing electronic, electrochemical, and dispersion properties, as compared to current material alternatives. Although these complexes have not been experimentally synthesized yet, our computational predictions indicate that they are experimentally viable.

## CHAPTER 6

### FUTURE WORK

The research projects in this dissertation reveal a brief picture of potential applications of organometallic/doped nanocarbon complexes in electrochemistry. However, as the current studies only cover a limited scope, follow-up studies of these complexes are needed. Generally speaking, two main fields of possible future study are proposed. First, the stability and properties of new organometallic/doped nanocarbon complexes, such as porphyrin<sup>TM</sup>/nanocarbon complexes and pyrazole<sup>TM</sup>/nanocarbon complexes, can be evaluated by protocols presented in Chapter 2 and 3 in this dissertation. In addition, new properties of our current Cp<sup>TM</sup>/nanocarbon complexes, like non-linear optical properties or catalytic properties, can also be investigated in future work.

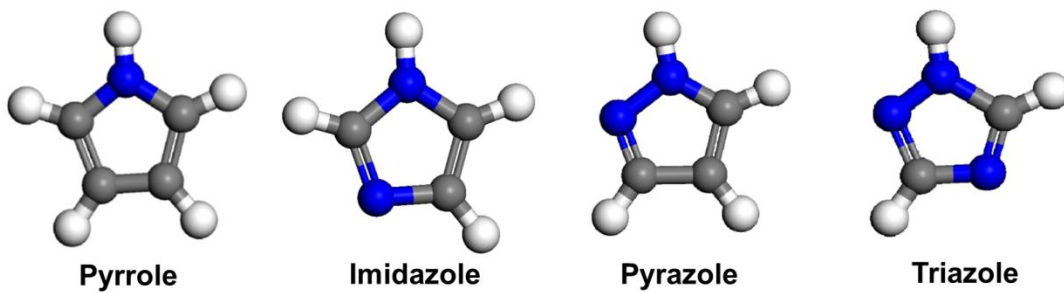
While the scope of our work is mainly focused on Cp<sup>TM</sup> complexes, other organometallic/doped nanocarbons complexes are also possible candidates for future materials. For example, Sarkar et al. and Dai et al. reported experimental and computational studies on the organometallic hexahapto-functionalized graphene and found tunable band gaps in these systems for nanoelectronic applications.<sup>1,2</sup> However, most of these reports are focused on pristine CNT or graphene supports. Based on our studies in this dissertation, doping within the nanocarbon supports drastically changes the properties of the organometallic nanocarbon complexes, and this motivates future work to expand the present organometallic nanocarbon systems to incorporate arene<sup>TM</sup> or hexahapto<sup>TM</sup> complexes on doped carbon supports. Moreover, new organometallic ligands with nitrogen containing five-member rings, like pyrrole, pyrazole, imidazole, and

triazole with TM and doped nanocarbon complexes should be investigated. The geometries of pyrrole, pyrazole, imidazole, triazole, pyrazoleFe/B-CNT (8,0) complex have been modeled, and the BEs (compared to the CpFe/B-CNT (8,0) complex) are shown in Figure 6.1. Even stronger BEs than the CpFe/B-CNT (8,0) complex are found. However, for this preliminary study, spin-unpolarized DFT calculations were used, which tend to overestimate the BE by about 1 eV. Taking this factor into consideration, the pyrazoleFe/B-CNT (8,0) complex is still more stable than its CpFe counterpart. Therefore, these complexes with N-containing five-member rings and TMs like Fe, Co, Ni, Cr, and Cu are possible candidates for future studies. Moreover, compared to ferrocene, the porphyrinTM complexes like heme, are also important electron donor-acceptors especially in bio-systems. The optimized porphyrinFe/B-CNT complex is shown in Figure 6.2, which was produced using the same computational method as Chapter 2. In particular, both computational and experimental works have shown potential applications of porphyrinTM/nanocarbon complexes in optoelectronics and electrochemical sensing.<sup>3-7</sup> Meanwhile, Brothers reported that novel structures and properties were found with porphyrin-based ligands and boron complexes, which are analogous to our porphyrinTM/doped nanocarbon system.<sup>8</sup> Considering the previous studies and examples in bio-systems, the possible TM candidates are suggested to be Fe, Mg, Zn and Cu. For these complexes, a similar computational routine with DFT and the analysis methods implemented in Chapter 2 and 3 can be used. However, one challenge of the porphyrin-based complexes is their size, which is larger than Cp. Also, in a periodic model, larger ligands call for a larger support (to eliminate the interactions between periodic images), which increase the total number of atoms in the system. To save some computation time, a scan of the porphyrinTM complexes using a semi-empirical method like PM6 is recommended before the actual DFT calculation. An example scan of the porphyrinFe

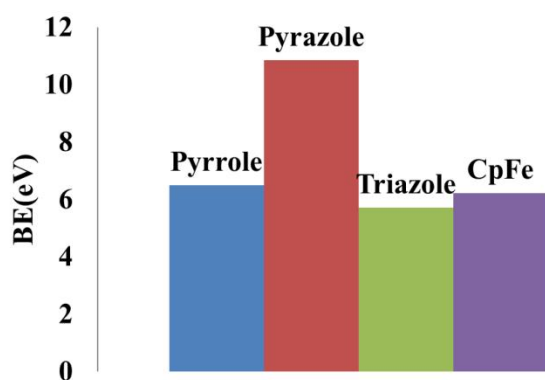
and B-CNT distance is shown in Figure 6.3. Therefore, future searches of organometallic/doped nanocarbons complexes for electrochemical applications should include porphyrin<sup>TM</sup> complexes and the pyrazole<sup>TM</sup> complexes.

In addition, future studies should also expand the scope of the fundamental property evaluation of these systems. For example, in Chapter 2, we reported preliminary work using AIMD to predict the oxygen adsorption and dissociation on CpFe/B-CNT complexes to explore the possible catalytic applications of these complexes for ORR. However, a more complete study is needed to evaluate the catalytic properties, transition states and reaction barriers for multiple possible reaction pathways. Future studies may start a transition state search based on the barriers we located using AIMD in Chapter 2. However, locating the transition states of different possible reaction pathways is challenging work. The other possible focus would be the non-linear optical properties of our present Cp<sup>TM</sup> complexes. Ferrocene derivatives with a large conjugated and delocalized pi-electron system are proven to have “switchable” non-linear optical properties.<sup>9, 10</sup> For example, Sporer et al. found that a ferrocene-based compound with a large conjugated structure exhibited different linear and non-linear optical properties among its non-ionic, neutral ionic, cation, and anion form (can be seen directly from the colors of different forms).<sup>10</sup> Follow-up studies showed that these switchable non-linear optical properties were correlated to the delocalization of the MOs. For the more delocalized CpFe/BGr complexes in Chapter 3, the non-linear optical properties should be investigated in future work. Also, since the non-linear optical properties of porphyrin<sup>TM</sup>/pristine CNT have previously been reported, similar routines can also be used in our future work on porphyrin<sup>TM</sup>/nanocarbon complexes. In support of this effort, the computational routines to calculate the hyperpolarizabilities in solution are well developed.<sup>11</sup> The computational cost of our proposed systems should be acceptable.

a)



b)



c)

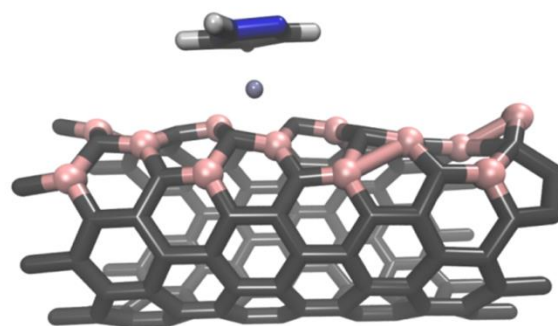


**Figure 6.1.** a) Proposed N-containing five-member rings, b) BEs of different N-containing five-member rings/Fe/B-CNT(8,0) complexes, c) Optimized geometry of pyrazoleFe/B-CNT(8,0) complex.

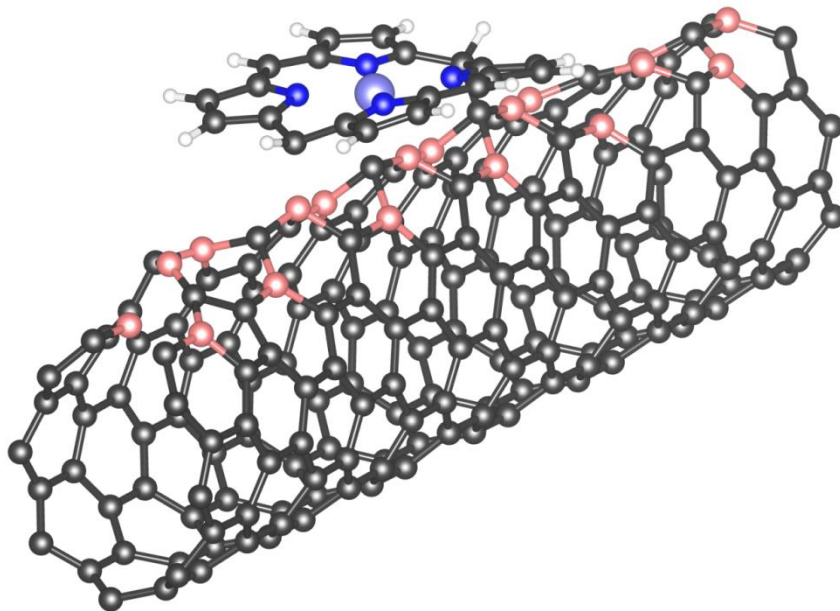


**Figure 6.2.** Optimized geometry of a porphyrinFe/B-CNT complex.

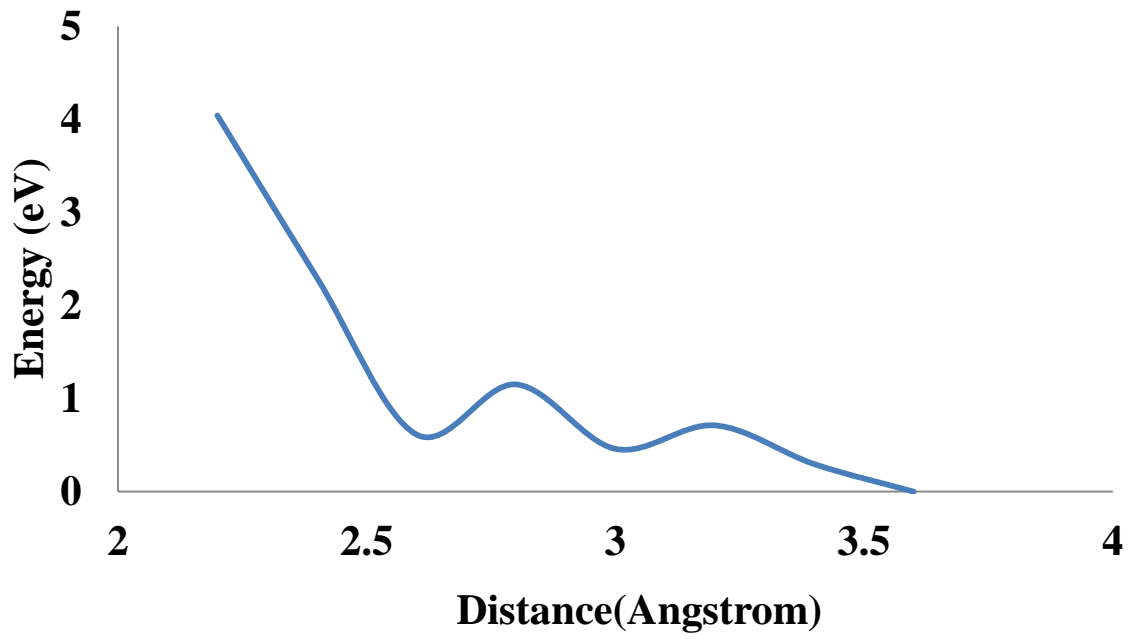


**Figure 6.3.** PM6 scan of a porphyrinFe/B-CNT complex.

## References

- (1) Sarkar, S.; Zhang, H.; Huang, J. W.; Wang, F. L.; Bekyarova, E.; Lau, C. N.; Haddon, R. C. Organometallic Hexahapto Functionalization of Single Layer Graphene as a Route to High Mobility Graphene Devices. *Advanced Materials* **2013**, *25*, 1131-1136.
- (2) Dai, J.; Zhao, Y.; Wu, X. J.; Zeng, X. C.; Yang, J. L. Organometallic Hexahapto-Functionalized Graphene: Band Gap Engineering with Minute Distortion to the Planar Structure. *Journal of Physical Chemistry C* **2013**, *117*, 22156-22161.
- (3) De Souza, L. A.; Da Silva, A. M.; Junqueira, G. M. A.; Carvalho, A. C. M.; Dos Santos, H. F. Theoretical Study of Structure and Non-Linear Optical Properties of Zn(II) Porphyrin Adsorbed on Carbon Nanotubes. *Journal of Molecular Structure-Theochem* **2010**, *959*, 92-100.
- (4) D'Souza, F.; Das, S. K.; Sandanayaka, A. S. D.; Subbaiyan, N. K.; Gollapalli, D. R.; Zandler, M. E.; Wakahara, T.; Ito, O. Photoinduced Charge Separation in Three-Layer Supramolecular Nanohybrids: Fullerene-Porphyrin-SWCNT. *Physical Chemistry Chemical Physics* **2012**, *14*, 2940-2950.
- (5) Pascu, S. I.; Kuganathan, N.; Tong, L. H.; Jacobs, R. M. J.; Barnard, P. J.; Chu, B. T.; Huh, Y.; Tobias, G.; Salzmann, C. G.; Sanders, J. K. M.; Green, M. L. H.; Green, J. C. Interactions between Tripodal Porphyrin Hosts and Single Walled Carbon Nanotubes: an Experimental and Theoretical (DFT) Account. *Journal of Materials Chemistry* **2008**, *18*, 2781-2788.
- (6) Wei, A.; Li, W. W.; Wang, J. X.; Long, Q.; Wang, Z.; Xiong, L.; Dong, X. C.; Huang, W. Single-Walled Carbon Nanotube Networked Field-Effect Transistors Functionalized with Thiolated Heme for NO<sub>2</sub> Sensing. *Chinese Physics Letters* **2011**, *28*, 127304.
- (7) Zhao, L. Y.; Liu, H. Y.; Hu, N. F. Assembly of Layer-By-Layer Films of Heme Proteins and Single-Walled Carbon Nanotubes: Electrochemistry and Electrocatalysis. *Analytical and Bioanalytical Chemistry* **2006**, *384*, 414-422.
- (8) Brothers, P. J. Boron Complexes of Porphyrins and Related Polypyrrole Ligands: Unexpected Chemistry for both Boron and the Porphyrin. *Chemical Communications* **2008**, *18*, 2090-2102.
- (9) Kaur, P.; Kaur, M.; Depotter, G.; Van Cleuvenbergen, S.; Asselberghs, I.; Clays, K.; Singh, K. Thermally Stable Ferrocenyl "Push-Pull" Chromophores with Tailorable and Switchable Second-Order Non-Linear Optical Response: Synthesis and Structure-Property Relationship. *Journal of Materials Chemistry* **2012**, *22*, 10597-10608.
- (10) Sporer, C.; Ratera, I.; Ruiz-Molina, D.; Zhao, Y. X.; Vidal-Gancedo, J.; Wurst, K.; Jaitner, P.; Clays, K.; Persoons, A.; Rovira, C.; Veciana, J. A Molecular Multiproperty Switching Array Based on the Redox Behavior of a Ferrocenyl Polychlorotriphenylmethyl Radical. *Angewandte Chemie-International Edition* **2004**, *43*, 5266-5268.

- (11) Cammi, R.; Mennucci, B.; Tomasi, J. An Attempt to Bridgethe Gap between Computation and Experiment for Nonlinear Optical Properties: Macroscopic Susceptibilities in Solution? *Journal of Physical Chemistry A* **2000**, *104*, 4690-4698.